Characterisation of a gantry-based 250 MeV ultra-high dose rate (FLASH) continuous scanning proton beam

Julian van Zanten

TU Delft

HollandPTC
Proton Therapy Centre

Characterisation of a gantry-based 250 MeV ultra-high dose rate (FLASH) continuous scanning proton beam

Master Thesis

to obtain the degree of Master of Science in Applied Physics
at the Delft University of Technology,
to be presented and defended on 28 June 2024 at 10:30

by

Julian van Zanten

Student number:	4725514	
Project duration:	9 October 2023 - 14 June 2024	
Daily supervisor	K.H. Spruijt	HollandPTC
Thesis committee	prof.dr. M.S. Hoogeman	TU Delft, HollandPTC
	dr.ir. D. Lathouwers	TU Delft
	dr. W.G. Bouwman	TU Delft

Cover: Combined image of two individual spot lists, irradiated on the IBA Lynx detector, and visualised through Python. Spot lists are not on scale.

An electronic version of this thesis is available at http://repository.tudelft.nl/.

TU Delft Delft University of Technology

HollandPTC Proton Therapy Centre

Acknowledgements

After nine months of hard work, I have finished this thesis, an achievement that holds great significance for me and would not have been possible without the help of numerous individuals.

Foremost, I would like to express my deepest gratitude to both my supervisors, Kees Spruijt and Mischa Hoogeman. Kees, I am incredibly grateful for your invaluable input, friendly attitude, and patience throughout the past nine months. This thesis would not have been possible without your help. Thank you for introducing me to the fascinating world of medical physics, and for sharing the delights of poke bowls. Mischa, thank you for the insightful monthly meetings and the informal moments we shared during my stay at HollandPTC. Your guidance, coupled with the excitement of three thrilling races — with the Rotterdam Marathon serving as the cherry on top — has truly pushed me beyond what I believed were my limits.

I would like to extend my sincere thanks to all the staff members I crossed paths with at HollandPTC, who I have all found very friendly and happy to help. With special thanks to the R&D department, particularly Marta Rovituso and Thomas Toet, for their generous help in the data analysis and in setting up all the detectors, both before and during the measurement sessions in the (late) evenings. Considering the sheer volume of emails I sent to both of you, I'm pleasantly surprised I didn't end up on an internal spam list. Thanks should also go to my fellow master's and PhD students, with a shout-out to Manon, Simone, and Siebren, who were there from the beginning. You all made my stay at HollandPTC a true joy. I really enjoyed our punctual lunches at noon, our perhaps too frequent and long coffee breaks, and the infamous 'junior researchers borrel'. Also, it would be careless of me not to mention the massage chair, who has been my best friend since day one.

This thesis also marks the end of my time as an applied physics student in Delft. I have spent the last seven years trying to understand how this world works, but ultimately, I think I am left with more questions than answers. This, perhaps, is the true nature of physics, and I wouldn't have it any other way. I count myself incredibly lucky to have embarked on this journey with an amazing group of friends, which formed during the study association's first-year's weekend in 2017 and has managed to stick together all these years. To all of my dear friends, thank you so much for the fun, both in and outside the lecture halls, and support throughout the years. I really hope that we continue to spend plenty of time together and go on yearly trips abroad for many years to come. A special thanks to Thomas, Brent and Maaike for making our Monday meetings at TN the perfect start to each week. I really appreciate our collaboration on our theses and all the fun we managed to have along the way too.

Lastly, I must extend my appreciation to my friends and family from Dordrecht. My parents have provided support throughout my entire academic journey, standing by me through even the most challenging times, especially during the start of my bachelor's program. My friends are truly lifelong companions. Each of you has contributed immeasurably to my personal growth and success. I am profoundly grateful for every moment of encouragement and every shared experience.

Julian van Zanten
Delft, June 2024

Abstract

Evidence indicates that ultra-high dose rate (UHDR) irradiation in radiotherapy can induce a normal tissue sparing effect without compromising effectiveness against tumour cells, known as the FLASH effect. This has prompted active research into clinical proton FLASH therapy. A key step is developing a clinically safe and predictable proton FLASH beam, which is being pursued through the commissioning of the ProBeam gantry in FLASH mode at HollandPTC. As part of this process, this thesis aims to characterise the gantry-based 250 MeV ultra-high dose rate continuous scanning proton beam, currently only intended for preclinical research.

Four distinct dosimetric aspects have been investigated, in accordance with the AAPM TG-224 report and machine quality assurance guidelines for UHDR proton beams in transmission mode. The first three, which are also part of conventional characterisations, include lateral and longitudinal relative dosimetry, along with absolute dosimetry measurements. These encompass the spot shape, spot position, integral depth dose (IDD) curve and output measurements. The fourth category includes temporal dosimetry, an essential aspect for FLASH characterisations since delivery time has now become an important aspect. For this, the scanning speed, spot dwell time and dose rate (constancy) have been determined. The temporal measurements were conducted using the FlashQ detector, a 2D strip ionisation chamber with a temporal resolution of 1 ms, which also served as a reference monitor chamber to enable the full spatiotemporal reconstruction of each irradiation. Measurements were conducted at nominal nozzle currents from 2 to 215 nA to explore potential correlations between the measured parameters and nozzle current. The suitability of all other detectors used in this work for FLASH measurements has also been assessed.

The spot shape did not show a clinically significant dependency on the nozzle current, and the average Gaussian parameters were determined to be σ_x = 3.39 ± 0.06 mm, σ_y = 3.86 ± 0.02 mm and θ = -16.6 ± 4.5 degrees. Spot position accuracy was within 0.15 mm, complying with AAPM TG-224 standards. The R_{80}-value from the integral depth dose (IDD) measured 37.9 ± 0.1 cm, aligning with IDD results from other ProBeam facilities. Absolute dose per monitor unit (MU) varied significantly with nozzle current, from 0.0041 Gy/MU at 10 nA to 0.0466 Gy/MU at 215 nA. In terms of temporal aspects, the gantry scanning speed was found to depend on the spot spacing but converged to 7.8 ± 0.1 m/s and 29.4 ± 0.9 m/s in the x- and y-directions respectively for large spot spacings (> 50 mm). The nozzle monitor chamber reached saturation at a nominal nozzle current of 18.4 nA, resulting in fixed spot dwell times. This saturation caused significant dose rate fluctuations, both day-to-day and beam-to-beam. Over six measurement sessions in a four-month period, deviations ranged from -13.9% to -23.2% compared to planned dose rates, with an average intraday fluctuation of 3.9%. These fluctuations were measured with the FlashQ, which has been verified as a suitable reference detector.

Ultimately, the gantry-based 250 MeV UHDR continuous scanning proton beam has been successfully characterised at HollandPTC. All conventional parameters met the AAPM TG-224 standards or aligned with findings from other ProBeam institutes. Using the FlashQ as a reference monitor chamber enables the reconstruction and simulation of dose delivery in both space and time through calibration.

Contents

List of Figures

Nomenclature

Abbreviations

Abbreviation	Definition
AAPM	American Association of Physicists in Medicine
ANOVA	Analysis Of Variance
BPC	Bragg Peak Chamber
CONV	Conventional
DADR	Dose-Averaged Dose Rate
ESS	Energy Selection System
FC	Faraday Cup
FWHM	Full Width at Half Maximum
HollandPTC	Holland Proton Therapy Centre
IAEA	International Atomic Energy Agency
IDD	Integrated Depth Dose
IDR	Instantaneous Dose Rate
ISOC	Isocentre
LINAC	Linear Accelerator
MC	Monitor Chamber
MU	Monitor Unit
NMC	Nozzle Monitor Chamber
NTCP	Normal Tissue Complication Probability
OAR	Organ At Risk
PBS	Pencil Beam Scanning
PBS-DR	Pencil Beam Scanning Dose Rate
PDD	Percentage Depth Dose
PS	Passive Scattering
PT	Proton Therapy
QA	Quality Assurance
RT	Radiotherapy / Radiation Therapy
SD	Standard Deviation
SOBP	Spread-Out Bragg Peak
TCP	Tumour Control Probability
TPS	Treatment Planning System
TRS	Technical Reports Series (IAEA)
UHDR	Ultra-High Dose Rate
WET	Water Equivalent Thickness

1

Introduction

1.1 Background

With over 2.7 million new cases and 1.3 million fatalities annually, cancer ranks as the second leading cause of mortality and morbidity within the European Union, particularly impacting younger people with it being the main cause of death for individuals under 65 years of age [1]. The trend is concerning as cancer rates are expected to increase even further with 18.4% by 2040, mainly driven by an ageing population [2]. Consequently, the EU has committed itself to turning the tide against cancer with "Europe's Beating Cancer Plan", launched in 2022. This plan focuses on introducing preventative measures, improving cancer treatment, and enhancing quality of life for cancer patients and survivors. With an estimated 12 million European cancer survivors, including approximately 300,000 childhood cancer survivors [3], it is beyond dispute that improving treatment efficacy and aftercare is of paramount importance.

While a variety of cancer treatment options is available nowadays, the three traditional and most widely used modalities are surgery, chemotherapy, and radiotherapy (Figure 1.1). The choice of treatment depends on numerous factors, including the type and stage of cancer [4]. Surgery entails the physical removal of cancer and is most effective for localised, solid tumours that have not metastasised. Chemotherapy involves the administration of drugs to kill cancer cells or to impede their growth throughout the body. It is prescribed for cancers that have metastasised or that are particularly susceptible to specific drugs. Radiotherapy (RT) utilises high doses of radiation to destroy or damage cancer cells, thereby reducing tumour size and impeding their growth and spread. RT is employed to treat various cancer types and can be utilised for tumours practically inaccessible via surgery. On average, more than 50% of all cancer patients in Europe require at least one RT course [5–7]. This thesis concentrates on the field of radiotherapy.

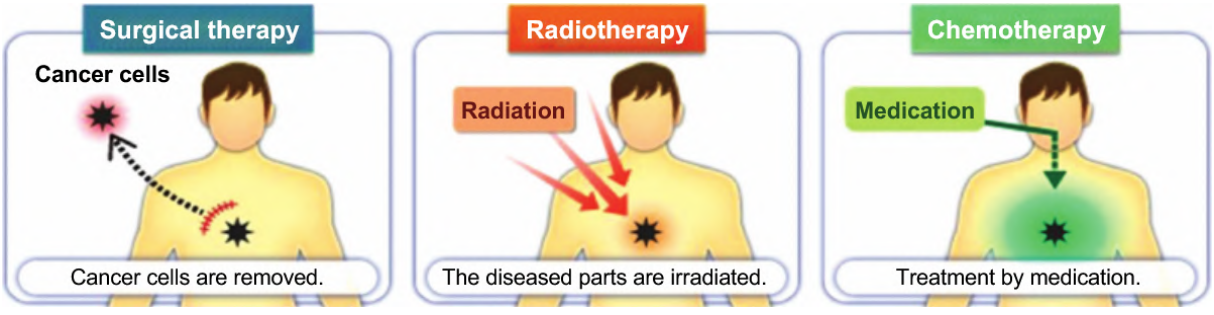

Figure 1.1: Illustration of the three traditional cancer treatment modalities: surgical therapy, radiotherapy and chemotherapy. Figure is taken from [8].

1.1.1 Radiotherapy

Radiotherapy is implemented in various clinical techniques. Nonetheless, at its core, radiotherapy operates on the fundamental principle of damaging DNA within cancer cells. When high-energy radiation is delivered into the body, it will interact with the DNA strands either directly by the initial ionising radiation or indirectly by

ionising other particles, like water molecules, forming secondary electrons and free radicals that, in turn, damage the DNA. The energy transferred and retained in tissue during these interactions is measured as 'absorbed dose', denoted in units of Gray (Gy), representing the amount of energy (in Joules) absorbed per unit mass (in kilograms). Biologically, these interactions lead to base mutations and/or discontinuities in the DNA strands. While base mutations and single-strand breaks can be repaired more easily by cell processes, a double-strand break is more lethal to the cell because an accurate repair is not always possible [9]. However, the process of inducing DNA damage can act as a double-edged sword: while it does lead to the death of cancerous tissue in the form of double-strand breaks, it may also trigger dangerous base mutations in healthy tissue (that cause cancer in the first place). Therefore, the primary goal of RT is to maximise damage to cancer cells while minimising the absorption of radiation in healthy tissue.

A treatment planning system (TPS) plays a crucial role in this challenge. A TPS is a software program that automates the process of determining a suitable dose distribution plan in which radiation exposure to healthy tissue is minimised while still sufficiently radiating cancerous cells. By analysing the patient's anatomy, tumour characteristics, and radiation beam properties, the TPS performs a mathematical optimisation problem, driven and bounded by a so-called 'wish list'. This list contains the objective function with individually weighted priorities and hard constraints, like imposing minimum absorbed dose values for cancerous tissue and maximum absorbed dose values for organs at risk (OAR), usually in units of Gray. By sequentially minimising objectives by their priorities, a (Pareto) optimal plan is crafted, providing favourable trade-offs among all objectives. An example of a dose distribution plan can be seen in Figure 1.2.

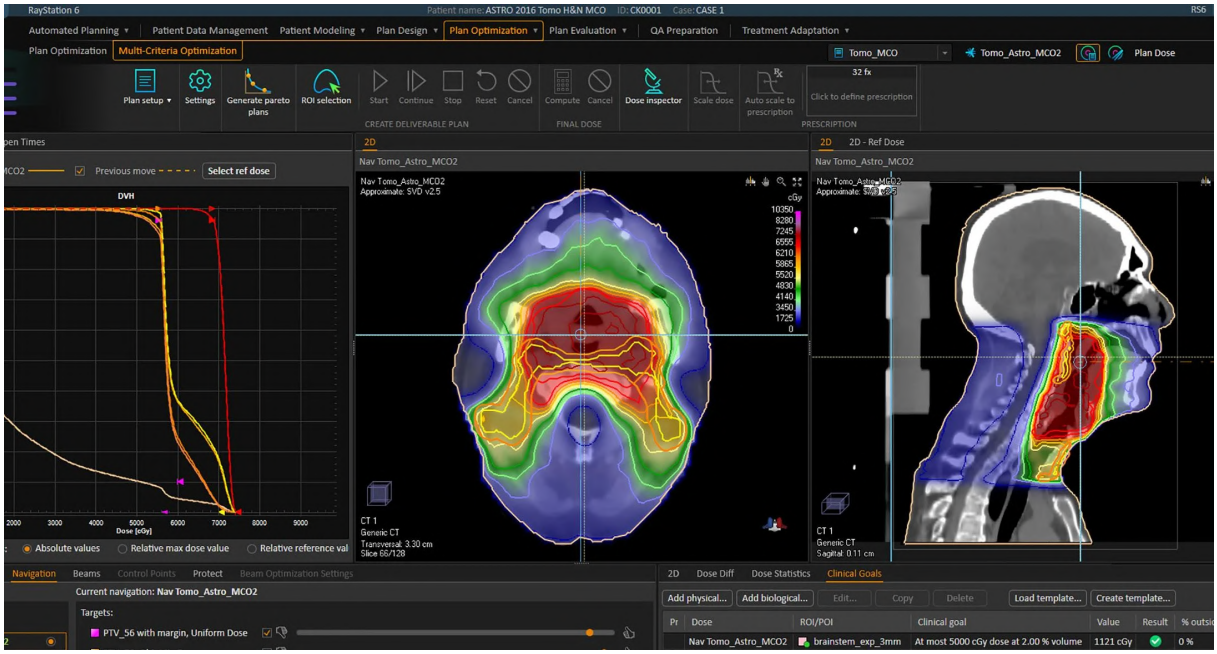

Figure 1.2: Snapshot of a dose distribution plan made with the treatment planning system 'RayStation'. Blue areas represent volumes with relatively low absorbed doses, while red volumes have high absorbed dose values. Figure is taken from [10].

In the challenge of minimising collateral damage to healthy tissue, besides the TPS, one can also look more fundamentally at different radiotherapy methods. Initially, a distinction can be drawn based on where the high-energy source spatially originates from. If the radiation source is located inside the patient's body, in close proximity to cancerous cells, it is classified as 'internal radiotherapy'. One example of internal RT is brachytherapy, in which a solid radioactive source, known as a "seed", is planted either within or adjacent to a tumour. This source emits radiation targeted at a small area to eradicate cancer cells, usually in the form of α-radiation. The other type of radiotherapy is 'external beam radiotherapy'. Here, a specialised machine directs beams of high-energy radiation towards the tumour from outside the patient. By far the most prevalent form of external beam RT is photon therapy for which a medical linear accelerator (LINAC) is used. In this device, a stream of electrons is generated and consecutively accelerated to high speeds in a waveguide, and then directed into a target typically made of tungsten or other heavy metals. Upon colliding with the target, the electrons produce X-rays through the process of bremsstrahlung. For photon therapy, the energy of these X-ray beams ranges between 4 and 15 MV [11]. By adjusting the shape and/or intensity of the photon beam to match the contour of the tumour, the dose can be delivered very precisely to the tumour, while sparing as much surrounding healthy

tissue as possible. However, dose distributions using photon beams are inherently constrained by the exponential attenuation of photons in tissue. Consequently, a substantial dose is absorbed very close to the skin, making it less applicable for e.g. the treatment of deep-seated tumours [12], or tumours close to organs at risk. This is where protons come into play as, contrary to photons, protons deliver the majority of their dose towards the end of their path.

1.1.2 Proton radiotherapy

Proton therapy (PT) is a form of external beam radiotherapy in which high-energy protons are used as ionising radiation instead of photons. High-energy protons are produced by accelerating protons in either a cyclotron or synchrotron to energies in the clinical range of 70 to 250 MeV. Despite sharing similar ionising properties with photons, protons exhibit unique characteristics in their dose deposition throughout the body. This is visualised in Figure 1.3.

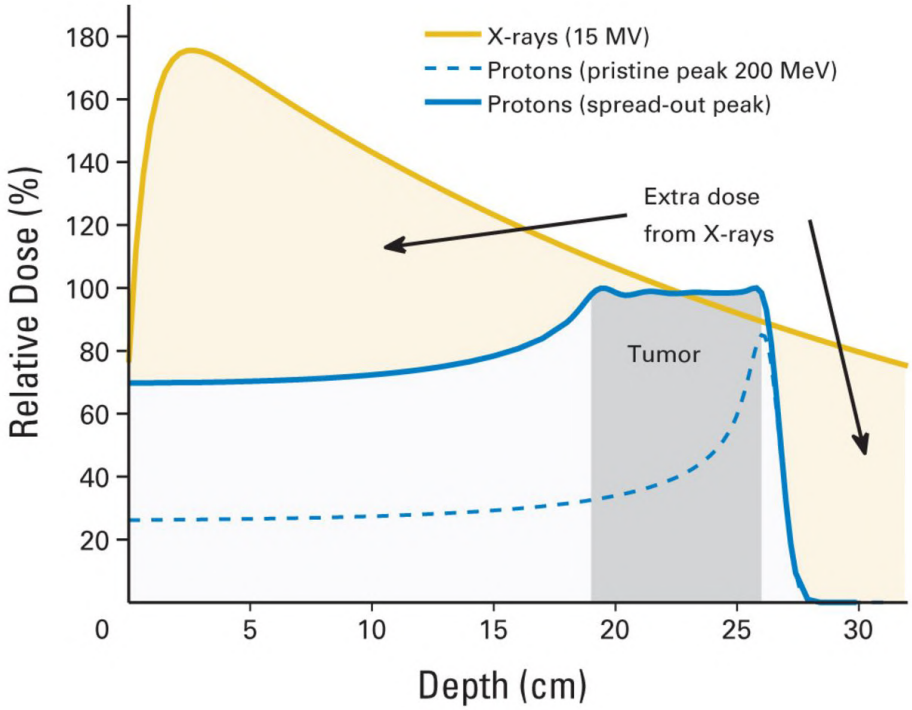

Figure 1.3: Comparison of three different depth-dose distributions: a photon beam (X-rays), a pristine (mono-energetic) and a spread-out (multi-energetic) proton beam. The grey area represents the tumour volume that ideally should receive 100% of the relative dose. The yellow area signifies the extra dose deposited by the photon beam in comparison with the spread-out proton beam. Figure is taken from [13].

The primary advantages of utilising protons over photons stem from the finite range and the distinct peak in dose deposition of the proton beam. As previously discussed in subsection 1.1.1, the photon beam depth dose distribution shows an exponential decrease in energy deposition with tissue depth after a brief build-up region. This shape is intrinsic to neutral particles: as the particle traverses the body, it either interacts, consequently transferring its energy to secondary electrons, or remains unchanged. This leads to an exponential decrease in the number of particles. The build-up region can be attributed to the fact that it takes a while for secondary electrons to build up in the beam. This is clinically beneficial and is called the skin-sparing effect [14]. Still, such a depth-dose distribution can lead to a significant dose delivery to healthy tissue located in front of and behind the tumour with respect to the incident beam direction.

However, protons carry a positive charge and will therefore undergo different interactions within the body, resulting in a different depth-dose distribution. The main mechanism through which protons interact with matter is collisions with electrons. Protons gradually lose energy due to Coulomb interactions with atomic electrons. The amount of energy lost per unit length is a function of the proton's speed: the slower a proton travels per unit length, the more energy it deposits through electromagnetic interactions with electrons,

resulting in a bigger dose deposition. This rate of energy loss is called the 'stopping power' and is inversely proportional to the square of the mean speed of the proton through the Bethe-Bloch formula:

$$\frac{dE}{dx} \propto \frac{1}{v^2}\left(\frac{Z}{A}\right)z^2 \tag{1.1}$$

with Z and A the atomic and mass number of the target nucleus respectively and z the charge number of the proton [15]. For mono-energetic beams, the dose deposited by protons increases sharply near the end of their range. This results in a distinct, narrow peak in the depth-dose distribution, which is called the 'Bragg peak'. The Bragg peak is very relevant in clinical settings as it allows for precise, local targeting of tumours, while still minimising dose to surrounding healthy tissue. Furthermore, in contrast to photons, protons come to a full stop at the end of their range. Consequently, it is possible to prevent the deposition of excess dose to healthy tissue distal to the Bragg peak by making use of the fact that the range of a proton depends on its velocity (and therefore kinetic energy) upon entry of the body. The empirical relation between a proton's range R in water and kinetic energy E is approximated by:

$$R(E) \approx 0.00244E^{1.75} \tag{1.2}$$

with R in cm and E in MeV [16, 17]. This relation is essential for high dose conformity, i.e. administering radiation such it that matches the exact volume of the tumour and preserves neighbouring healthy tissue, because, in practice, the narrow width of a single Bragg peak does not cover the full volume of a tumour. To achieve optimal dose conformity, the Bragg peak must be distributed across the tumour's depth. This is accomplished by exposing the patient to proton beams of varying energy and intensity, resulting in a relatively uniform depth-dose profile. This phenomenon is known as a 'spread-out Bragg peak' (SOBP) and is illustrated in Figure 1.3. Often, a range modulator wheel is used, which is a flat, circular device with different thicknesses around its edge. These thicknesses slow down proton beams to varying degrees. By spinning the wheel at a predetermined rate, the beam enters the patient with a mix of energies, creating an SOBP to accommodate the longitudinal shape (depth) of the tumour. Nevertheless, to treat the whole tumour, one also has to increase the width and height of the beam so that both lateral directions are covered. Traditionally, this is achieved by passively scattering the initial beam using a scattering system, which widens the beam (see Figure 1.4A). Then, after the range modulator, a collimator/aperture is used, which is a beam stop with a hole shaped to match the outer projection of the target in the beam, as seen from the beam's eye view. Finally, a range compensator is used to longitudinally shift the SOBP to the actual depth of the tumour.

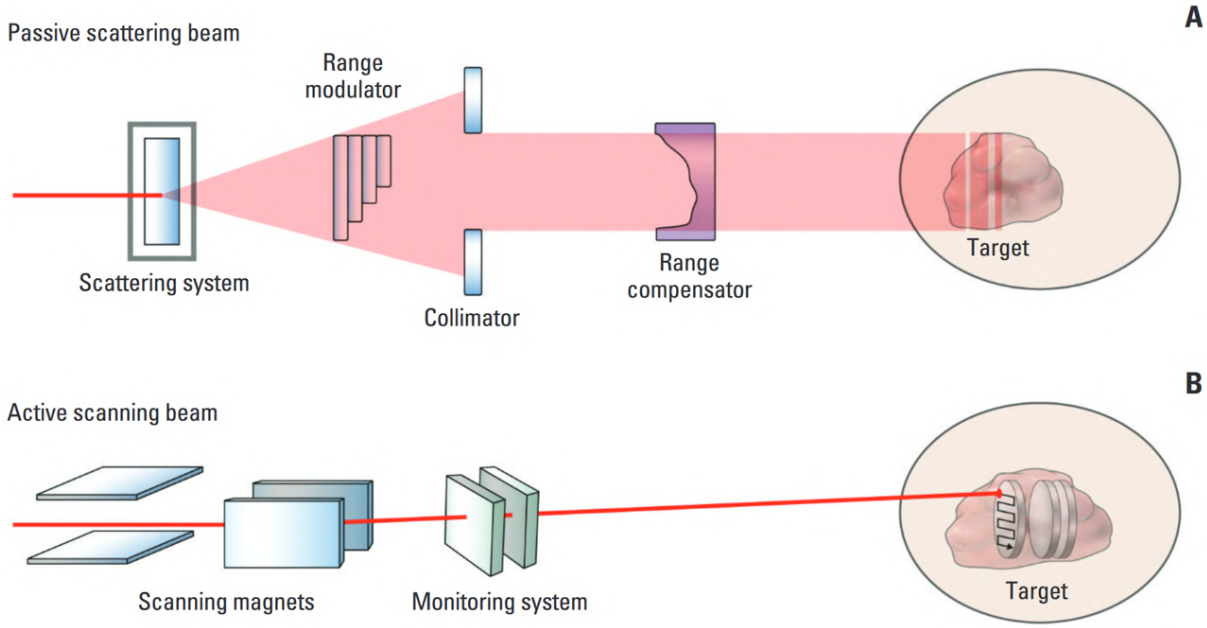

Figure 1.4: Schematics of a passive scattering beam (**A**) and an active/pencil scanning beam (**B**) used in proton therapy. Figure is taken from [18].

In general, passive scattering (PS) proton radiotherapy is a safe and straightforward technique for patient irradiation, and research has demonstrated that there are clear advantages over photon therapy in various cases. These advantages include reduced doses to OARs and improved dose conformity to cancerous tissue

[19, 20]. Additionally, PS proton therapy exhibits lower sensitivity to the time structure of the proton accelerator [21]. However, it is not without its drawbacks. Significant proton loss occurs during the scattering process and aperture shaping, with only approximately 5% of the initially generated protons reaching the patient. Efforts to enhance efficiency have led to the development of double scattering systems, but even with these improvements, efficiency remains capped at around 40% [21]. Moreover, the use of double scattering systems increases susceptibility to beam steering, potentially resulting in skewed dose distributions if the beam is off-centre by even a millimeter [22]. Furthermore, passive scattering systems are resource-intensive and can be time-consuming. Custom aperture and range compensator fabrication for each patient is necessary to ensure suitable dose conformity. This approach not only leads to higher costs but also limits flexibility in dose plan adaptation and presents challenges in radiation protection [23]. Also, with the inclusion of extra components such as these, patients could receive higher doses than planned due to an increased production rate of secondary neutrons, with the range modulation wheel being a significant contributor [21, 22, 24]. Ultimately, dose conformity is restricted to the depth of the SOBP, making PS systems less suitable for treating tumours with complex anatomies, such as those curved around OARs or with significant thickness variations [21, 25]. These limitations, combined with significant advancements in photon therapy, have led to the fact that PS proton therapy shows similar clinical results to advanced photon therapy techniques for various cancer types [26, 27].

To further increase efficacy and find solutions for these limitations, a third generation of proton RT systems was developed: pencil beam scanning (PBS) proton therapy. Instead of scattering and shaping the beam to the correct tumour volume with PS proton therapy, in PBS, the proton beam is scanned across the target cross section using magnets, which is visualised in Figure 1.4B. By consecutively changing the range of the beam with a range shifter, the various 'layers' of the tumour can be reached, allowing for the complete irradiation of the 3D target volume. While there are various scanning modes, a PBS pattern is usually created by defining individual spot coordinates that determine where the magnets should steer the proton beam to. As the pattern can be altered for each layer, PBS allows for a more accurate delineation of the tumour and therefore better dose conformity, even if it includes complex volume shapes [28]. To ensure a uniform dose distribution throughout the whole volume, the intensity/weight of each spot is determined by a dose conformity optimisation problem. This is called 'intensity-modulated proton therapy'. While intensity-modulated *photon* radiotherapy can also achieve similar dose conformity nowadays, PBS proton therapy requires fewer beam directions to achieve similar results, leading to less dose exposure to healthy tissue and lower toxicity [27, 29], in some cases even resulting in a total body dose reduction of 60% [26, 30]. When compared directly to other proton therapy techniques like single and double PS, it has been shown that PBS can again lead to less toxicity in normal tissue [28, 31–34]. Moreover, no scattering system, aperture and range compensator are needed with PBS. Consequently, lower production rates of secondary neutrons are observed [21, 35, 36].

Nonetheless, the usage of proton therapy (and radiotherapy in general) in cancer treatment is still inherently limited by radiation-induced toxicity in healthy tissue [37, 38]. Despite intensity-modulated proton therapy using the pencil beam scanning technique contributing significantly, the process of lowering toxicity in normal cells is still actively researched. In this quest, an increased interest in ultra-high dose rate irradiation is observed as it has been reported that this could lead to a healthy tissue sparing effect while remaining equally effective against cancer cells. This is called the FLASH effect and serious efforts are made to implement this in proton therapy.

1.1.3 FLASH radiotherapy

FLASH radiation therapy is a technique in cancer treatment and involves delivering radiation at ultra-high dose rates (UHDR) such that the FLASH effect is induced. Various studies have shown that the FLASH effect exhibits the ability to spare normal tissues while retaining similar levels of tumour cytotoxicity, i.e. similar toxicity to tumour cells when compared to conventional RT [39–43]. The phenomenon of sparing normal tissue in radiation therapy is referred to as the FLASH effect, and the corresponding branch of radiotherapy is known as FLASH RT. Hence, the implementation of the FLASH effect in proton therapy is called proton FLASH therapy.

In general, FLASH RT involves the delivery of doses at dose rates that usually are multiple orders of magnitudes higher than conventional (CONV) RT. While no clear thresholds are agreed upon, FLASH RT is typically as of 40 Gy/s, whereas in CONV RT, dose rates are usually ranged between 0.01-0.4 Gy/s [37, 39, 40, 44–46]. As a result, in FLASH RT, the total dose is administered within extremely brief time frames, typically lasting only one second at most, and in some cases, as short as 200 milliseconds [44, 45, 47]. However, "the full definition is more complex and involves several interdependent physical parameters" [39]. This ongoing investigation underlines the fundamental exploration of FLASH RTs parameters and their implementation.

Understanding the biological mechanism of the reduced toxicity in FLASH RT also remains an ongoing pursuit, but it is postulated to involve multiple contributing factors. The leading theory, increasingly supported, suggests oxygen depletion plays a crucial role in the biological response to FLASH irradiation [48–53]. As mentioned in subsection 1.1.1, high-energy radiation creates free radicals through interaction with water molecules in the cells. By reacting with oxygen, these free radicals turn into peroxyl radicals that damage DNA [54]. In CONV RT, the oxygen in cells gets replenished through normal cell processes. However, in FLASH RT, local oxygen depletion could outpace reoxygenation within the short exposure time, inducing a transient state of radiation-induced hypoxia. Because of the reduced oxygen levels, fewer peroxyl radicals are generated in this condition. This spares healthy tissue from FLASH irradiation, while minimally impacting the already oxygen-deprived cancerous tissue due to inefficient oxygen delivery in the inherently abnormal tissue structure [45, 55]. However, while reports have successfully demonstrated a sparing effect under hypoxia conditions [56–58], the oxygen-depletion theory has been questioned in recent research [59], e.g. due the observation of similar sparing effects under normoxic conditions [60], simultaneously reinforcing the postulate that FLASH mechanism is indeed multifactorial. Multiple systematic and literature reviews on FLASH RT have suggested various other mechanisms, like increased double-strand break rates, immune response modulation and increased stem cell preservation under FLASH RT [39, 44, 46, 59]. Nonetheless, additional research is necessary to resolve any ambiguity surrounding the underlying mechanisms of the FLASH effect.

The concept of a dose rate-dependent sparing effect was initially discussed in articles dating back almost six decades [61, 62]. However, these studies were promptly discontinued due to the challenges in effectively applying the findings to clinical practice. In the last decade, there has been a renewed interest in using FLASH in clinical settings, mainly due to technological advancements in radiotherapy. Clinically, the benefits of the FLASH effect can be described by two parameters, the 'normal tissue complication probability' (NTCP) and the 'tumour control probability' (TCP). For a certain amount of Gray, the NTCP represents the likelihood of complications in healthy tissue from RT, while the TCP denotes the likelihood of effectively controlling or eliminating a tumour with RT. As FLASH RT can induce a sparing effect for normal tissue, while still being (approximately) as effective for cancerous tissue, for a fixed amount of dose D, the following NTCP and TCP conditions are expected:

$$NTCP_{FLASH}(D) \lesssim NTCP_{CONV}(D)$$
$$TCP_{FLASH}(D) \approx TCP_{CONV}(D)$$

The gap between the NTCP and TCP, known as the 'therapeutic window,' is anticipated to widen with FLASH RT, aligning with the aforementioned conditions. Two beneficial aspects arise from a larger therapeutic window: firstly, it reduces toxicity in normal tissue for the same absorbed dose due to a smaller NTCP, and secondly, it allows for higher TCP values by delivering a bigger dose to the tumour with similar NTCP levels. Figure 1.5 substantiates this claim with preclinical data from an experiment by Montay-Gruel et al., in which mice with implemented human brain tumour cells are irradiated with UHDR electron beams [42]. The figure demonstrates a rightward shift in the NTCP curve for FLASH RT, with a significantly smaller shift of the TCP, resulting in an extended therapeutic window with corresponding benefits. Multiple other in-vivo studies, i.e. experiments or observations that are conducted within a living organism, have successfully replicated similar findings where the FLASH effect has led to normal tissue sparing [44, 63].

Although multiple preclinical experiments have been performed successfully, clinical studies are extremely scarce. The first clinical treatment of a patient irradiated with electron FLASH RT was reported in 2019 by Bourhis et al. [43]. Here, a 75-year-old man with a cutaneous lymphoma resistant to multiple treatments had metastases spread across various areas of his skin. The patient had encountered adverse effects from previous treatments involving around 110 tumour sites, utilising either X-rays or low-energy electrons. Due to a continued poor skin response, it was decided to administer FLASH RT. The results were promising, as after 5 months of the FLASH RT treatment, nearly all signs of adverse skin reactions from the treatment had vanished. However, while it does ascertain the technical feasibility and clinical safety of electron FLASH RT, more research is needed to prove its efficacy for more complex anatomy and to directly compare with CONV RT [44].

Proton FLASH radiotherapy

Similar to electron RT, the implementation of the FLASH effect in proton radiotherapy is under thorough investigation, with the majority of research conducted in preclinical studies. In 2020, Diffenderfer et al. published one of the initial in-vivo papers demonstrating the FLASH effect in proton RT [64]. In this study, mice were randomly assigned to receive double scattered proton beams at either CONV or FLASH dose rates. Ten days later, the mice were randomly divided into groups and received either 12 or 18 Gy doses using CONV or FLASH pro-

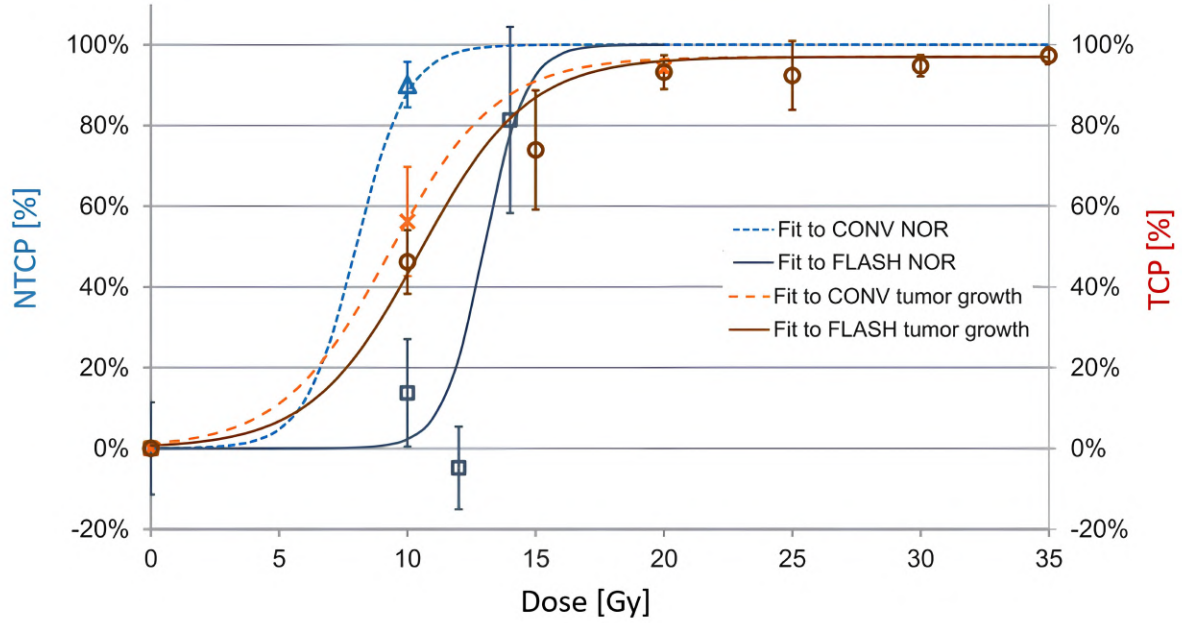

Figure 1.5: NTCP and TCP in electron FLASH RT as a function of the delivered dose. Blue graphs correspond to the NTCP, orange graphs to the TCP. TCP data is gathered by a 'novel object recognition' (NOR) test. For this experiment, CONV dose rates are defined to be 0.01 Gy/s & FLASH dose rates are 125 Gy/s. Error bars correspond to the standard deviation in the data. The figure is adapted from [39].

ton RT. The results were promising: mice subjected to proton FLASH RT exhibited reduced levels of intestinal damage and inflammation while maintaining similar levels of tumour control compared to CONV proton RT, with no significant differences found between dose rates and total doses. Numerous other papers have demonstrated similar beneficial effects attributed to the FLASH effect, with worst-case scenarios showing comparable NTCP and TCP values to CONV proton RT [44, 65–67]

The first clinical trial of proton FLASH RT, named FAST-01, was published by Mascia et al. in 2023, to validate the practicality of implementing proton FLASH RT in a clinical environment [68, 69]. Data were collected on 10 patients aged 18 years or older who underwent palliative FLASH radiotherapy for extremity bone metastases at the Cincinnati Children's/UC Health Proton Therapy Center between 3 November 2020 and 28 January 2022. All patients received a single UHDR proton beam field with dose rates of 51 - 61 Gy/s. Similarly to CONV proton RT, 8 Gy was irradiated per delivery site in a single fraction. The results showed consistent results with conventional proton radiotherapy regarding treatment efficacy and normal tissue sparing, without encountering any FLASH-related technical complications or delays. This again demonstrates the technical feasibility of proton FLASH RT and thus "supports further exploration of FLASH radiotherapy in patients with cancer" [68]. This has lad to the second, and still on-going, clinical trial of proton FLASH RT, FAST-02. The primary objective of FAST-02 is to evaluate the toxicities linked with FLASH radiotherapy treatment while also assessing its effectiveness in alleviating pain among individuals with painful thoracic bone metastases [70].

Proton PBS FLASH radiotherapy

Proton PBS FLASH radiotherapy aims to integrate the FLASH effect into proton PBS radiotherapy, with the overarching objective of harnessing the advantages offered by both PBS and the FLASH effect. As previously discussed in subsection 1.1.2, PBS systems already offer notable advantages over PS proton systems, including enhanced dose conformity, greater flexibility in dose plan adaptation, and reduced toxicity in normal tissue. Realising the FLASH effect within PBS could further enhance tissue sparing compared to conventional proton PBS radiotherapy. Theoretically, PBS could lend itself very well to the realisation of the FLASH effect as no scattering systems are needed to ensure sufficient dose conformity, consequently leading to higher proton transmission efficiencies. However, in practice, meeting the requirements for conformal dose delivery while maintaining the 40 Gy/s FLASH threshold across the entire treatment field has proven to be challenging. Hence, novel PBS FLASH modalities frequently compromise one or more of the advantages associated with conventional PBS radiotherapy. Currently, the two main techniques are 'transmission' and 'conformal/Bragg peak' PBS FLASH RT.

First, with transmission PBS FLASH RT, so-called 'transmission' or 'shoot-through' proton beams are used, meaning that the kinetic energy - and thus range - of the initial beam remains unchanged during the whole treatment. Hence, the Bragg peak, which is typically used to precisely target cancerous tissue, may not align with the shape of the tumour. Instead, for proton FLASH RT, the cancer cells are often situated within the relatively stable plateau region of the depth-dose curve of the proton beam. Then, after passing through the body, the proton beam exits the patient at the opposite side, hence the name transmission PBS FLASH radiotherapy. This transmission effect is evident in dose plans, as shown in Figure 1.6. While it sounds counter-intuitive to exclude the distinct characteristic of proton therapy, as the usage of the Bragg peak has formed the basis for all regular proton RT methods, the usage of transmission beams is one of the few techniques in which the FLASH effect can be induced with the current proton PBS RT systems. In fact, almost all proton FLASH RT studies, including the clinical test by Mascia et al., are performed with transmission beams [44]. The reason behind this has to do with the limitations of the energy selection system. For conventional proton PBS RT, to ensure sufficient dose conformity over the whole tumour, multiple layers are irradiated by constantly changing the energy of proton beams. This is done by the energy selection system (ESS). However, the usage of an ESS results in a significant decrease in the beam current due to beam transmission efficiency loss [71–73]. This makes it practically impossible to reach ultra-high dose rates, which are a requirement for FLASH RT. Furthermore, the usual time required for switching energy is around 900 milliseconds for cyclotron systems based on energy degradation, and it extends beyond 1000 milliseconds for synchrotron systems [74, 75]. This extended duration for energy switching further elongates the beam-on period. For the FLASH effect to be induced, the total dose must be administered within extremely brief time frames, at most one second, which is practically impossible with an ESS included.

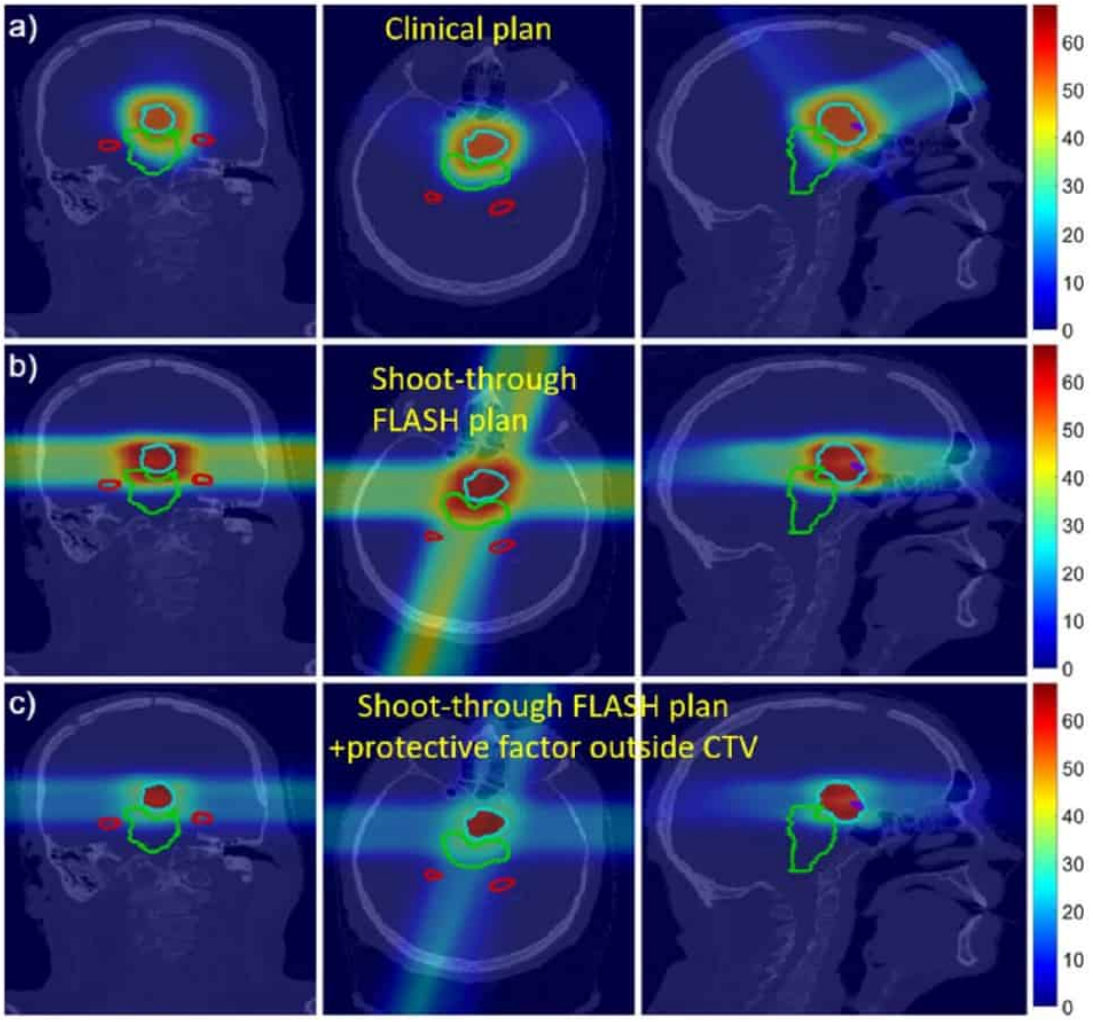

Figure 1.6: Proton dose distributions from three CT planes. (a) Standard four-beam plan. (b) Hypothetical shoot-through FLASH plan without considering protective effects. (c) Same shoot-through FLASH plan with protective effect (factor 2) beyond the target volume. The delineated volumes include the tumour (light blue) and OARs (red, green, and purple). The dose is delivered in units of Gray. Figure is taken from [76].

The second technique that has been proposed is called 'conformal/Bragg peak' PBS FLASH RT. Here, a beam-specific static energy modulation device is included to produce a polyenergetic beam, allowing for a highly conformal dose. An example of such a device is a ridge filter, which allows for the creation of an SOBP without the need for an ESS or rotating range modulator wheel, reducing the total treatment time. This inclusion has been successfully implemented already in regular PBS proton RT [77, 78], with recent studies indicating that proton FLASH RT can be achieved with ridge filters included too [79, 80]. Additionally, Simeonov et al. have introduced the concept of a patient-specific 3D range-modulator, which can be best understood as a unified integration of a range compensator and a very fine static ridge filter [81]. Conformal radiation may also be achievable without an energy modulation device, albeit with the necessity for faster energy layer switching as multiple beam energies are essential to ensure good dose conformity [82].

Nevertheless, the choice between transmission-based and conformal proton PBS FLASH RT can be seen as a significant trade-off: the former method compromises on conformality to achieve higher dose rates by shooting proton beams through the patient, while the latter approach may utilise static energy modulation devices to halt the beam within the patient, thereby ensuring distal conformality. In addition, other advantages and disadvantages have also been identified. For example, transmission beam PBS FLASH RT is less sensitive to range and setup uncertainties, but is limited by a maximum patient size as the beam must exit the patient. On the other hand, conformal PBS FLASH RT requires fewer beams, offering greater flexibility in the planning approach regarding avoidance regions, but could be inherently limited by the plan-specific energy modulation device [82]. At the moment of writing, the usage of transmission beams for proton FLASH RT is deemed more practical for preclinical studies [71], and several studies in treatment planning have already examined the possibility of implementing transmission proton pencil beam scanning beams in broader and more realistic clinical scenarios, including cancers of the head and neck [76, 83, 84], lung [85, 86], and liver [87].

Regardless of the PBS modality, the translation of PBS FLASH into clinical treatment planning is a non-trivial and complex task, with the main challenge being the search for a reliable quantification of the dose rate for pencil beam scanning. For methods other than PBS, the total dose is usually delivered in timed pulses, with the entire field administered simultaneously within each pulse. This results in two relatively straightforward dose rates: the 'instantaneous dose rate' (IDR), which is the dose per pulse divided by the single pulse duration, and the 'field-averaged dose rate' (FADR), being the field dose divided by the total delivery time for all pulses. However, the consecutive scanning of spots adds a distinctive temporal and spatial element to the dose delivery of PBS proton therapy, which complicates and adds complexity to the quantification and characterisation of dose rates. Various studies have investigated the feasibility of the FLASH effect in proton PBS and have even proposed novel ways of translating the unique spatiotemporal effect into dose rates. In 2019, Van de Water et al. proposed a 'dose-averaged dose rate', in which the instantaneous dose rate for each voxel is weighted by the dose contribution of each spot, and then averaged over all spots [83]. Then, in 2020, Folkerts et al. suggested the 'pencil beam scanning dose rate' (PBS-DR), which redefines the effective irradiation time for a certain voxel by ignoring insignificant dose contributions of distant spots with a manually set minimum dose threshold [88]. Consequently, even if the total dose remains constant, variations in spot sequences within scan patterns — despite having identical spot coordinates and weights — can result in differences in the local PBS-DR. Hence, optimising the scan pattern can, to some extent, enhance the local FLASH effect by considering the spatiotemporal structure of dose delivery [89]. This optimisation process of scan patterns, resulting in varying dose rates, is shown in Figure 1.7. In addition, next to plan-related parameters, the dose rate is also related to machine properties, like the beam current and beam scanning speed. Therefore, a reliable procedure should be put into place to precisely determine the behaviour and properties of the proton beam and delivery system. Typically, this is done through means of a beam characterisation.

1.1.4 Beam characterisation

A beam characterisation is a comprehensive process of analysing and defining the behaviour, properties, and performance of a beamline and its delivery system. It ensures the accuracy and reliability of treatment delivery by providing crucial insights into the behaviour and properties of the proton beam. These properties can be used as input for treatment planning systems, allowing for the optimisation of patient treatment. The execution of a beam characterisation is standard procedure in the commissioning process of a proton therapy system. Such commissioning involves the initial setup and calibration of the machinery, e.g. a beamline or gantry, to ensure its safety and to prepare for clinical operation according to established protocols and standards. Then, after the commissioning process, repeated (and partial) beam characterisations take place as part of the quality assurance (QA) procedure. QA encompasses ongoing processes to verify and maintain the quality and safety of treatment delivery throughout the operational lifespan of the system. Similar to the com-

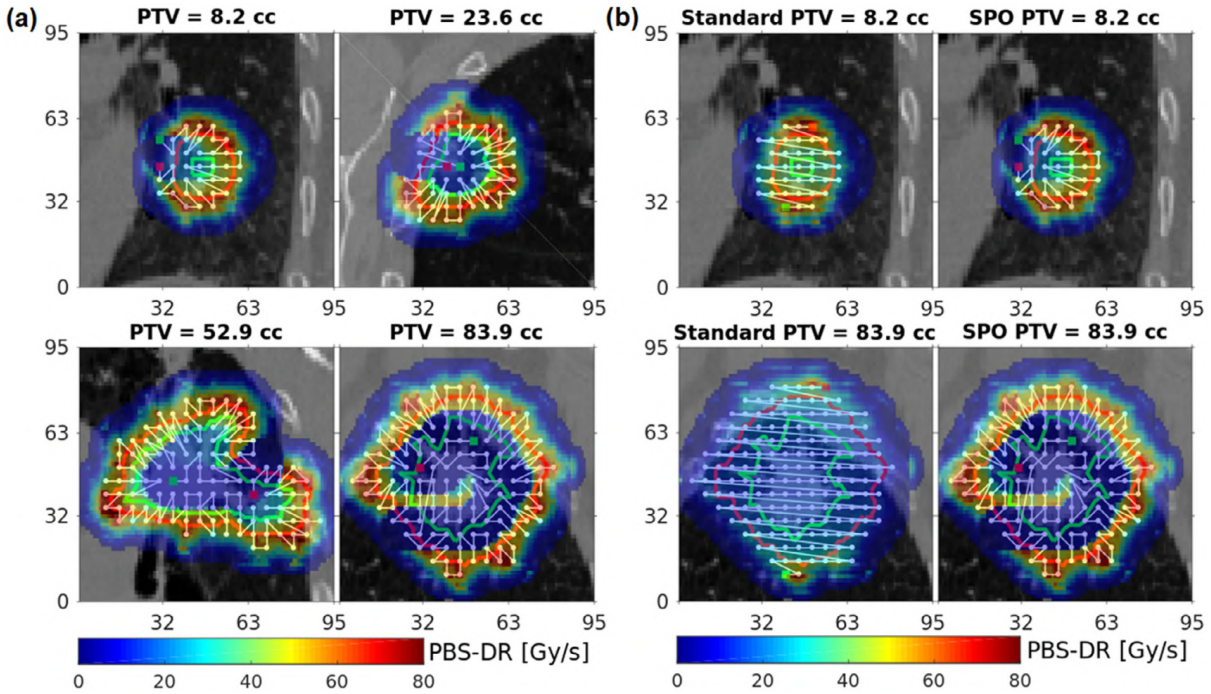

Figure 1.7: (a) Visualisation of the pencil beam scanning dose rate (PBS-DR) for various scan patterns that have been optimised. (b) Comparison between standard (non-optimised) line-by-line scan patterns and optimised scan patterns. For all scan patterns, the initial and final spot position are highlighted in green and red respectively. Figure is taken from [89].

missioning process, QA procedures ensure that the treatment system continues to meet established standards. As proton therapy has gained popularity and accessibility as a cancer treatment modality, the development of commonly agreed upon QA guidelines, alongside methodologies to establish these guidelines for proton therapy delivery, has become increasingly important. AAPM Task Group 224 has extensively tackled this issue and released a report that outlines recommended tolerance limits for various QA checks. Drawing from literature reviews and consensus data from numerous clinical therapy centres, this report is widely regarded as the benchmark for machine QA in proton radiotherapy [90]. Additionally, Spruijt et al. have contributed to this field by publishing an article that offers consensus-based practical guidelines on machine QA, the corresponding procedures and the suitability of detectors, specifically tailored for transmission-based proton PBS FLASH RT. [91]. Throughout this thesis, the works by AAPM TG-224 and Spruijt et al. will serve as the primary sources of support for decisions made in both the experimental setup and the assessment of clinical significance.

Characterisation reports from various conventional photon [92, 93], electron [93–96] and proton [97–100] beamlines have been published and are thus widely available, mainly because beam characterisations are standard procedure in the commissioning process of radiotherapy systems. Despite the different particle modalities, in general, similar parameters (e.g. beam spot shape, depth-dose distributions, absolute dosimetry) appear in these reports as the ultimate goal of the characterisation, namely defining the beam behaviour and extracting its properties, remains the same, regardless of the type of beam. However, for electron [101–103] and proton [104, 105] FLASH research beamlines, characterisation becomes more complex due to the temporal aspect of FLASH RT that now must be taken into account. This necessitates the usage of either novel analysis techniques or detectors with a sufficiently high temporal resolution. Coupled with the novelty of proton PBS FLASH radiotherapy, only one characterisation report for a gantry-based transmission FLASH proton beamline (Varian ProBeam) has been published by Charyyev et al. at this moment of writing [106]. Combined with an investigation on the suitability of various detectors, in short, this thesis aims to perform a characterisation of the Varian ProBeam beamline at Holland Proton Therapy Centre, abbreviated as HollandPTC.

1.2 Research goal

HollandPTC is a proton radiotherapy centre that specialises in providing proton therapy treatment for cancer patients. In addition to patient care, it also functions as both an educational and research institute. According to HollandPTC, one of the main research focuses is to improve the treatment efficacy, actively pursuing "the best proton therapy both now and in the future" [107]. Part of this research includes the realisation of ultra-high dose rate proton FLASH therapy, which has been shown to initiate the FLASH effect in healthy tissue. At the moment of writing, HollandPTC exclusively offers conventional proton therapy on its two cyclotron-based gantries. However, due to evidence indicating that the FLASH effect decreases the susceptibility of healthy tissue to radiation while preserving its effectiveness in killing tumour cells, the implementation of proton FLASH therapy at the gantries is actively researched for future clinical use. Specifically, the aim of HollandPTC's FLASH R&D consortium is to determine how to test the FLASH effect in a clinical trial for at least one treatment site before 2028. A critical step towards this goal is the development of a clinically safe and stable proton FLASH beam, which is being pursued through the commissioning of the ProBeam gantry at HollandPTC.

As part of the commissioning process of the gantry-based proton FLASH beam line, this thesis aims to determine the behaviour of the ultra-high dose rate continuous scanning proton beam. This is done by means of a characterisation of the 250 MeV transmission proton beam at the 'Citer' gantry. The characterisation is an essential part of the commissioning process of the UHDR proton beam for FLASH radiotherapy as it provides insight into the accuracy, reliability, and safety of the machinery before its potential clinical implementation. Moreover, beam parameters retrieved from the characterisation can be used as input for treatment planning systems, leading to accurate patient treatments, made specifically for the systems at HollandPTC. This research encompasses four characterisation categories. First, the lateral relative dosimetry is investigated, which involves examining the spot shape, spot position, and overall spread of the proton beam in air. Second, integrated depth dose (IDD) measurements are performed to quantify the in-depth relative dosimetry. Third, absolute dosimetry measurements are carried out to accurately measure the actual delivered dose per irradiation. Fourth and last, the study looks into temporal dosimetry, crucial for understanding the timing of dose delivery. This is particularly important since the FLASH effect requires a dose rate of at least 40 Gy/s. Hence, these measurements involve determining the spot dwell time and scanning speed, as well as investigating the consistency of the dose rate. Additionally, for the commissioning of UHDR proton therapy, all utilised detectors undergo a thorough investigation to determine their suitability for inclusion in proton FLASH measurements.

1.3 Overview

Chapter 2 outlines the materials and methods used in this thesis. Initially, it provides a detailed description of the Varian ProBeam proton therapy system and the detectors employed throughout this study. Following this, it explains and justifies the various experimental setups and methods used for each specific part or parameter of the characterisation process. Subsequently, Chapter 3 presents the findings from the four dosimetric categories. Similar to the methods chapter, the results for each characterisation element are presented separately. These findings are then analysed and their clinical relevance is discussed in Chapter 4. The thesis concludes with Chapter 5, where final conclusions and recommendations are offered.

2

Materials and Methods

2.1 Beam delivery system

HollandPTC has two clinical treatment gantries, called 'Luit' and 'Citer', that are served by the Varian ProBeam Proton Therapy System (Varian Medical Systems, a Siemens Healthineers company, Palo Alto, California, USA). The Varian ProBeam is a pencil beam scanning system and utilises an isochronous cyclotron to produce clinically usable proton beams of energies between 70 and 244 MeV. Initially, protons are accelerated to the maximum energy of 250 MeV but are then decelerated to lower energies after passing through the energy selection system, which consists of paired graphite-wedge plates with varying thicknesses. However, the ESS significantly reduces the fluence of the proton beam [71–73]. Therefore, to ensure the delivery of sufficiently high beam currents (and thus dose rates), the energy selection system is fully disengaged. Since disabling the ESS is solely achievable by switching the ProBeam from clinical mode to 'FLASH mode' (also known as 'Racehorse mode'), which is exclusively enabled by Varian on the Citer gantry, all measurements are conducted at the Citer. Ultimately, in FLASH mode, the ProBeam delivers monoenergetic 250 MeV proton transmission beams with a maximum requestable beam current of up to 215 nA.

This beam is transported from the cyclotron to the nozzle by the beam transport system. This setup comprises one or multiple vacuum tubes, periodically enclosed by quadrupole magnets placed to counteract any divergence in the proton beam as it travels through the system. This ensures that optimal beam quality is upheld, such that sufficiently small beam sizes, necessary for PBS, are achieved. Dipole magnets are used to bend the proton beam through corners. Then, the beam reaches the nozzle, which is mounted on a mechanical gantry. The gantry is a large, circular or semi-circular structure that rotates around the patient. The Varian Probeam in specific has a 360-degree rotating gantry that allows for treatment of the patient from any angle. However, to activate the FLASH mode on the ProBeam at HollandPTC, the gantry - and therefore nozzle - must be fixed at a 90-degree angle, which is shown in Figure 2.1. Therefore, all measurements are conducted under this specific orientation.

The nozzle itself possesses over hardware that is responsible for delivering the proton beam with great precision, both spatially and dosimetric. First, the nozzle has two scanning magnets that are responsible for steering the pencil beam horizontally (x) and vertically (y) to the correct position. These magnets are positioned successively and therefore create two distinct focal lengths, with $f_x = 200$ cm and $f_y = 256$ cm. These values represent the distances between each magnet and the gantry's isocentre (ISOC), which is the stationary reference point for the gantry's rotational movement. Similar to the focal length, the maximum scanning speed at which the magnets can steer the proton beam from one spot to another (at the isocentre) also varies for each direction, with the by Varian expected values of $v_x = 5$ m/s and $v_y = 20$ m/s. Second, a built-in ionisation chamber is used to monitor and control the intensity of the incoming proton beam. Under clinical circumstances, the amount of charge collected by this nozzle monitor chamber (NMC) is proportionally related to the total delivered dose through a predetermined conversion factor. This ensures that the system can validate the accurate delivery of dose per spot. However, the NMC has been shown to saturate at high nozzle currents, which is something that must be compensated for (see subsection 2.1.1).

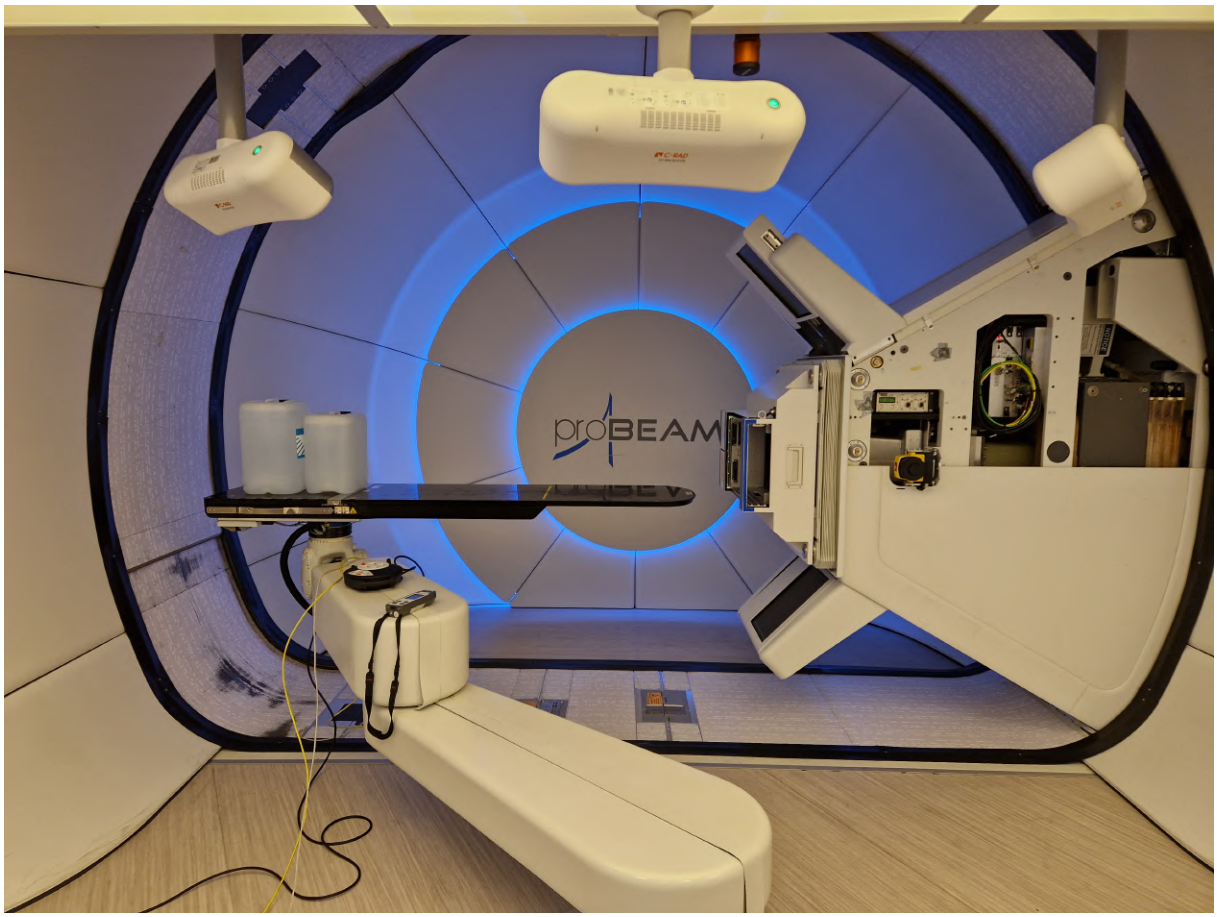

Figure 2.1: Photo of the Citer gantry at HollandPTC, with the gantry nozzle set at 90 degrees.

In FLASH mode, the ProBeam requires multiple beam delivery input parameters. First, the dose plan is determined through a comma-separated values spot list containing four columns: the spot number, the $x-$ and $y-$position of the spot and the number of monitor units (MU) per spot. Second, each spot list requires a nozzle beam current value (in nA). The nozzle current refers to the intensity of the proton beam emitted from the treatment nozzle. This differs from the cyclotron current, which indicates the intensity of the proton beam produced by the cyclotron accelerator before being directed towards the treatment nozzle for delivery. The ratio between the two is called the 'transmission efficiency' and is expected to be around 40%, with the cyclotron and beam transport system being the main contributors to the proton intensity loss. Third, the pencil beam scanning mode can be set to either spot or raster mode. In the spot mode, the proton beam turns off when moving from one spot to another, while in the raster mode - also known as "smearing mode" or "continuous scanning mode" - the pencil beam remains on when moving between spots. All measurements in this thesis are performed in raster mode.

2.1.1 Nozzle monitor chamber saturation

The nozzle monitor chamber is responsible for ensuring that the delivered dose per spot is in accordance with the dose plan, or in FLASH mode, with the spot list. The amount of dose per spot is denoted in so-called monitor units, acting as the linking face between the dose plan and the gantry. Normally, a single MU can be directly translated to a set amount of dose, which works as follows. Protons that pass through the NMC produce charges through the ionisation of gases. The rate at with charge is produced by gas ionisation, $\dot{Q}_{produced}$, is proportional to the number of protons per second, $\dot{N}_p$, and thus to the nozzle current I. The control electronics monitor the total charge collected by the chamber over the whole irradiation time and compare it to the expected total charge $Q_{planned}$, which is proportional to the total amount of MU. Then, if $Q_{planned} = Q_{collected}$, the NMC halts the beam delivery for the currently planned spot and continues with the next spot.

Hence, assuming that the produced charge is fully collected ($\dot{Q}_{produced}(I) = \dot{Q}_{collected}(I)$), the delivery time per spot, t_{dwell}, is given by:

$$t_{dwell} = \frac{Q_{planned}}{\dot{Q}_{produced}(I)} = \frac{Q_{planned}}{\dot{Q}_{collected}(I)} \propto \frac{MU}{I} \tag{2.1}$$

Then, as the dose D is a function of the total number of delivered protons N_p, the dose becomes proportional to the total amount of MU:

$$D \propto N_p = \dot{N}_p \cdot t_{dwell} \propto I \cdot t_{dwell} \propto I \cdot \frac{MU}{I} = MU \tag{2.2}$$

However, the assumption that all produced charges are collected is only valid for non-saturating ionisation chambers. Reports indicate that the ProBeam's nozzle monitor chamber experiences significant ion recombination effects at sufficiently nozzle currents [108], resulting in an extremely low ion collection efficiency of around 7 to 10% at 215 nA [109]. Recombination effects refer to the phenomenon in which the ionised electrons recombine before reaching the collecting electrode in the ionisation chamber, leading to an underestimation of the produced charge rate: $\dot{Q}_{produced}(I) \gg \dot{Q}_{collected}(I) \approx \dot{Q}_{collected}$. Because the charge production rate loses its dependency on the nozzle current, the dwell time becomes proportional to the MU per spot:

$$t_{dwell} = \frac{Q_{planned}}{\dot{Q}_{produced}(I)} = \frac{Q_{planned}}{\dot{Q}_{collected}} \propto MU \tag{2.3}$$

Consequently, the delivered dose is not solely proportional to the amount of MU anymore, but to the product of the nozzle current and MU:

$$D \propto N_p = \dot{N}_p \cdot t_{dwell} \propto I \cdot t_{dwell} \propto I \cdot MU \tag{2.4}$$

This new dependence of the delivered dose on the nozzle current, attributed to the nozzle monitor chamber's inability to effectively monitor and regulate the proton beam, causes significant challenges in various dose delivery aspects. The reliance on the nozzle current for dose delivery without feedback from the nozzle monitor chamber introduces variability in administered doses. This inability to verify the accuracy of dose delivery makes ensuring consistent dosages practically impossible. This challenge is aggravated by experiments conducted at HollandPTC indicating substantial discrepancies between the nominal (requested) nozzle current and the detected nozzle current, with a standard deviation of ±10%. Typically, this could be remedied by either increasing or decreasing the spot dwell time, but such adjustments are not viable when dealing with a saturated NMC. Therefore, for almost all experiments, an external detector that does not suffer from recombination effects is placed as the first element in the setup, acting as a reference monitor chamber (FlashQ ionisation chamber, see section 2.2). By calibrating the FlashQ readings with the correct nozzle current (see subsection 2.6.5), it becomes possible to retrospectively obtain the detected nozzle current for each irradiation.

2.2 Detectors

For this work, the following devices are used:

- FlashQ (DETECTOR, Torino, Italy [110]): The FlashQ is an air-vented strip ionisation chamber that can measure the beam profile and provide particle flux estimations for ultra-high intensity beams. The detector consists of two layers with 128 strips in each direction (x and y) and two layers with integral strips. With an active area of 128 x 128 mm^2, an effective resolution of 1 mm is achieved. Moreover, the FlashQ exhibits linearity across its entire intensity range (0.03 - 1000 nA), as it is engineered to mitigate recombination effects and prevent front-end signal saturation problems commonly found in conventional gas ionisation chambers. With a nominal raw data acquisition rate of 1 kHz, all registered beam profile and particle flux data include high-resolution temporal information. For each time step, the detector registers the signal from each of the 128 horizontal and 128 vertical strips, along with two integral values.

- Lynx PT (IBA Dosimetry, Schwarzenbruck, Germany [111]): The Lynx detector is a scintillation screen made of gadolinium-based plastic material, which converts the ionising radiation's energy into photons. These photons are then directed to photodiodes located on a CCD camera positioned outside the irradiation field. The detector has an active surface area measuring 300 x 300 mm^2, an effective resolution of 0.5 mm and is optimised for pencil beam scanning. This configuration enables it to deliver a high-resolution 2D image depicting the relative intensities of the incoming radiation beams. Depending on the total intensity of the beams, the iris aperture of the Lynx must be set such that no saturation of the individual detector pixels of interest occurs. Note that the Lynx detector is not transparent and should be positioned as the final element of the setup.

- Gafchromic EBT3 film (Ashland, Covington, Kentucky, USA [112]): Gafchromic EBT3 film is a type of radiochromic film commonly used in radiation therapy dosimetry. This film contains a 28 µm marker dye that undergoes a colour change when exposed to ionising radiation. This characteristic enables the film to effectively characterise the level of exposure and beam profile in radiation therapy applications. The EBT3 film can achieve a high spatial resolution, reaching resolutions as fine as 25 micrometers or less, but is limited by the scanning technique. A scanner captures the red, green, and blue colour components of light transmitted by the film, which allows for the linking of the film's optical density to its corresponding dose response through calibration.

- BC-75 Faraday Cup (Pyramid Technical Consultants, Waltham, Massachusetts, USA [113]): The BC-75 Faraday cup is a device used to measure the total charge of a charged particle beam by collecting all the particles that pass through it. Combining it with the gathered temporal information about the beam, the BC-75 can directly measure the proton beam current for energies ranging between 30 to 250 MeV. The operational design for in-air operation has been validated through comparison with a reference vacuum Faraday collector. Following this comparison, the typical accuracy was found to be better than 2%, with enhanced accuracy observed at higher proton energies [114]. It must be noted that the detector will become activated as a result of exposure to high-energy proton beams. Although this activation does not impact performance and will naturally decay over time, it is essential to conduct radiation surveys on the device, and ideally, limit the total exposure to high-energy proton beams.

- Advanced Markus chamber (Type 34045, PTW, Freiburg, Germany [115]): The Advanced Markus is a vented plane-parallel ionisation chamber used for reference dosimetry in high-energy electron and proton beams. After calibrating the detector in a collimated beam of cobalt-60 gamma radiation, its reading (in nC) can be directly related to absorbed doses in water (in Gy). Combined with its small size (a sensitive area of 0.02 cm^3 and radius of 2.5 mm), the detector is very suitable for high spatial resolution, absolute dosimetry measurements.

- Bragg peak chamber (Type 34070, PTW, Freiburg, Germany [116]): The 34070 Bragg peak chamber is a vented plane-parallel ionisation chamber used for relative dosimetry in high-energy proton beams. Unlike the Advanced Markus chamber, which also is an ionisation chamber, the larger diameter of this chamber (sensitive radius of 40.8 mm) enables the measurement of the entire proton beam diameter, including scattered protons. This feature makes it suitable for precisely determining the location of the Bragg peak in proton beams.

- X-ray therapy monitor chamber (Type 7862, PTW, Freiburg, Germany [117]): The 7862 monitor chamber is a vented plane-parallel transmission chamber designed for dose monitoring in X-ray therapy units. With an even bigger radius than the Bragg peak chamber (sensitive radius of 59.8 mm), this monitor chamber is also highly suitable for serving as a thin window reference chamber in relative dosimetry measurements for proton therapy.

2.3 Lateral relative dosimetry

First, the lateral relative dosimetry measurements are explained. In the context of radiation therapy in general, lateral often refers to movement or measurements made perpendicular to the direction of the beam. For example, a lateral dose distribution refers to the dose distribution across the patient's body in the left-right direction, perpendicular to the direction of the proton beam. Similarly, lateral motion or lateral displacement may refer to the movement of the patient or treatment equipment sideways during treatment delivery. For this thesis, the direction of the beam is defined to be parallel to the z-axis. Therefore, lateral measurements are conducted in the xy-coordinate plane at a fixed depth z. The following subsections explain the purpose of and the steps taken during the measurements for the determination of the spot shape, spot position and beam envelope. Note that all measurements are either measured, translated and/or reported on a relative scale, meaning that all values are normalised on a scale from 0 to 1, based on the minimum and maximum detector reading value. Apart from practical considerations (such as certain detectors providing readings solely on a relative scale), this practice is implemented to enable straightforward comparison of measurements obtained from different detectors and under varying beam intensities. Ultimately, almost all readings can be translated to absolute dose values with the absolute dosimetry measurements, explained in section 2.5.

2.3.1 Spot shape

Purpose & Goal

The spot shape refers to the lateral dose distribution at a certain depth and describes the profile of the dose distribution of a single spot in the xy-plane. The lateral dose distribution of individual spots plays a significant role in optimising the overall dose distribution. Hence, accurately modelling this aspect within the treatment planning system is essential. This ensures the creation of accurate treatment plans that maximise treatment effectiveness while minimising damage to healthy tissues. Furthermore, AAPM TG-224 recommends that the verification of the spot shape is part of the monthly quality assurance procedure [90]. Therefore, it is important to obtain an accurate reference value to ensure the reliability of the QA process. The goal of this experiment is to accurately determine the lateral spot profile and investigate any potential dependency on the nozzle current.

Method

For this, the Lynx detector is used. The Lynx is placed on the gantry table and its centre of the effective area is aligned to the gantry's isocentre, shown in Figure 2.2. For each measurement, a single proton beam is irradiated through air to obtain pure spot images with minimal scatter. This procedure is repeated 10 times to get a statistically meaningful reference value for the mean spot shape, including uncertainty of the mean. The whole procedure is done twice, namely with two different nozzle currents: 10 and 215 nA, totalling up to 20 measurements in total. These values are chosen for two main reasons: firstly, the selection of 10 nA corresponds to one of the lowest feasible nozzle currents for which the instantaneous dose rate remains above 40 Gy/s. Conversely, 215 nA represents the highest nominal nozzle current achievable on the Varian ProBeam in FLASH mode. Secondly, this wide range facilitates the examination of how nozzle current affects the spot shape, while also leaving room to introduce further intermediate steps at evenly spaced intervals for other measurements. The amount of MU for each current is scaled such that approximately an equal amount of dose is irradiated.

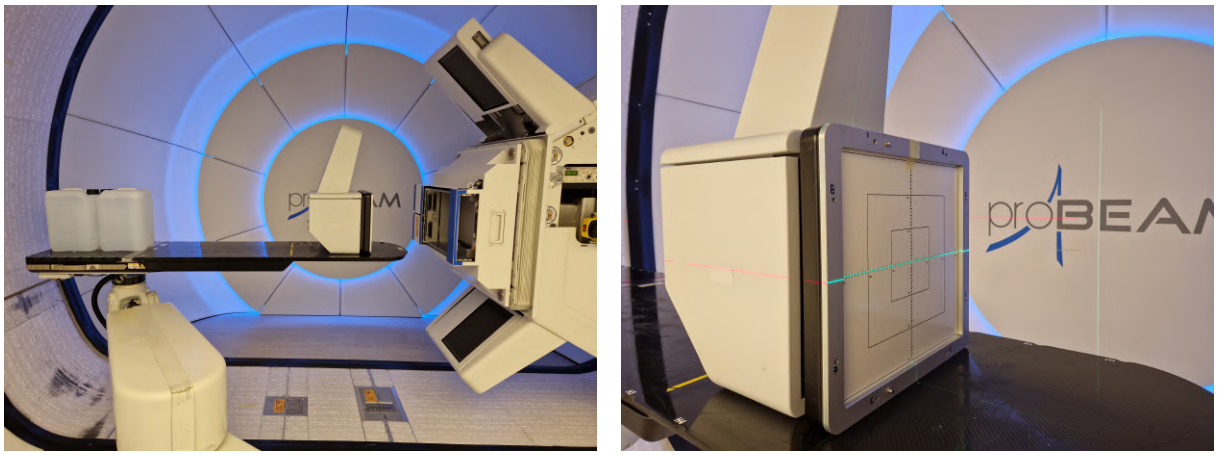

Figure 2.2: Experimental setup for the determination of the spot shape with the Lynx. The surface of the Lynx is aligned with the gantry's isocentre using the built-in green laser system of the ProBeam.

Data analysis

In order to quantify the beam spot shape, the lateral profile is approximated to be normally, but independently distributed in the x- and y-direction. Hence, a single two-dimensional elliptical Gaussian distribution, defined by standard deviations σ_x and σ_y, is used to describe the shape of the beam spot. Non-Gaussian contributions due to nuclear interactions are assumed to be negligible as the measurements are performed in air. The formula for the general two-dimensional elliptical Gaussian function is given by:

$$f(x,y) = A\exp\left(-\left(a(x-x_0)^2 + 2b(x-x_0)(y-y_0) + c(y-y_0)^2\right)\right) \quad \text{with} \quad \begin{cases} a = \dfrac{\cos^2\theta}{2\sigma_x^2} + \dfrac{\sin^2\theta}{2\sigma_y^2} \\ b = -\dfrac{\sin 2\theta}{4\sigma_x^2} + \dfrac{\sin 2\theta}{4\sigma_y^2} \\ c = \dfrac{\sin^2\theta}{2\sigma_x^2} + \dfrac{\cos^2\theta}{2\sigma_y^2} \end{cases} \tag{2.5}$$

In Eq. 2.5, σ_x and σ_y are the standard deviation (SD) of the Gaussian distribution, (x_0, y_0) is the centre coordinate of the Gaussian distribution, A is the height/amplitude of the distribution and θ is the angle which rotates the whole distribution around its centre coordinate, with $\theta \in [-45°, 45°]$ [118]. The rotation is defined to be positive for clockwise rotations, visualised in Figure 2.3. Then, least-squares fitting is performed on all 20 lateral spot profiles from the Lynx to obtain the optimal parameters for each data set. The mean values of σ_x, σ_y and θ, including corresponding uncertainties of the mean, are reported for each nozzle current.

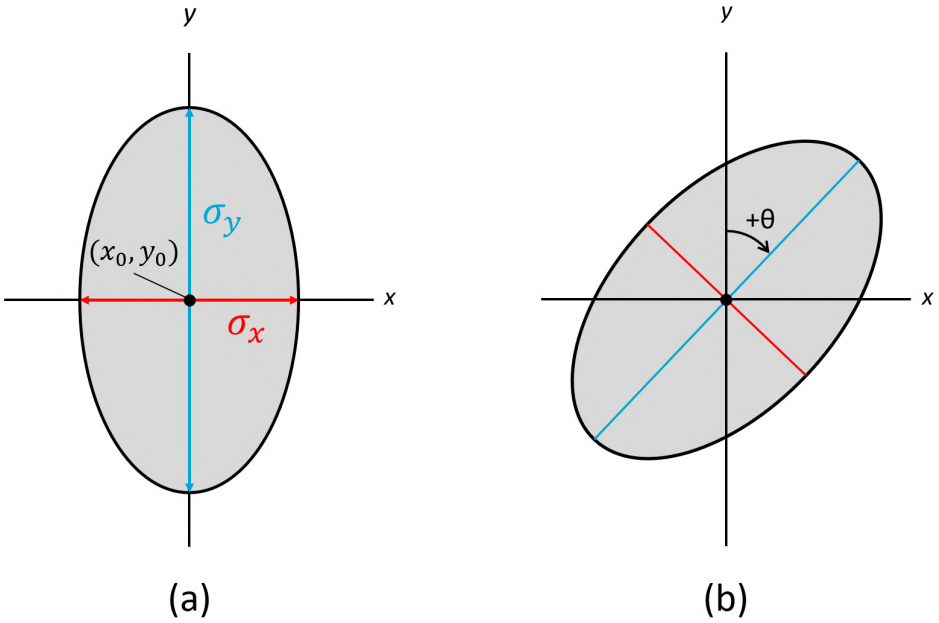

Figure 2.3: Illustration of (a) the 2D elliptical Gaussian definition with centre coordinate (x_0, y_0) and the orientation of the standard deviations σ_x and σ_y, and (b) the rotation θ of the whole normal distribution around its centre coordinate, with a positive rotation θ defined as clockwise.

To investigate the correlation between the spot shape and the nozzle current, an unpaired t-test and a Mann-Whitney U test are performed on the three parameter distributions (σ_x, σ_y and θ), which are retrieved from the 10 repeated measurements per nominal nozzle current (10 nA and 215 nA). In general, an unpaired t-test and Mann–Whitney U test are used to compare differences between two independent groups, but they differ in their assumptions, with the former assuming normally distributed data and the latter not requiring this assumption. For both tests, the null hypothesis H_0 posits that there is no difference between the two groups; specifically, it asserts that the distribution of values in both groups is identical. Hence, H_0 claims there is no statistically significant correlation found between the nozzle current and spot shape parameters, while the alternative hypothesis H_1 claims that a statistically significant correlation is indeed found. Both tests are valid for an individual sample size of ten [119]. The level of significance is set at $\alpha = 0.05$, meaning that H_0 is rejected for H_1 if the retrieved p-value is smaller than α.

2.3.2 Spot position

Purpose & Goal

The spot position typically refers to the lateral position of a delivered spot, particularly indicating its location in the xy-plane at the isocentre. In general, dose conformity is achieved through the optimisation of dose plans by treatment planning systems, which generate PBS plans wherein optimised spot position values and weights are determined. Given that the majority of spots deviate from the central beam axis, the proton beam must be directed by the steering magnets towards the desired spot position. Ensuring accurate dose delivery necessitates verifying the proper functioning of the steering magnets to prevent significant discrepancies between the expected and detected spot positions. This experiment aims to find the spot position accuracy, defined as the average deviation between the detected spot position and the planned spot position from the spot list.

Method

For this purpose, the FlashQ is used. The FlashQ is positioned directly on the gantry table, with its effective area aligned to the isocentre (see Figure 2.4). Spot lists are then irradiated with single spots arranged on a grid, including one spot on the central beam axis. Each spot list comprises seven rows and columns with spots at fixed intervals, totalling up to 49 spots per list with a weight of 100 MU per spot. Three different spot spacings are used: 5 mm, 7.5 mm, and 10 mm. The minimum spacing of 5 mm is chosen as this is larger than one standard deviation of the elliptical spot profile in both the x- and y-direction, making it easier to distinguish between different spots. The maximum spacing of 10 mm is selected because, in FLASH mode, the threshold for continuous scanning is just above 10 mm, beyond which the proton beam temporarily stops irradiating when moving between spots (see subsection 2.6.6). To investigate a potential dependency on the nozzle current, each spot list is irradiated twice: once at 10 nA and once at 215 nA.

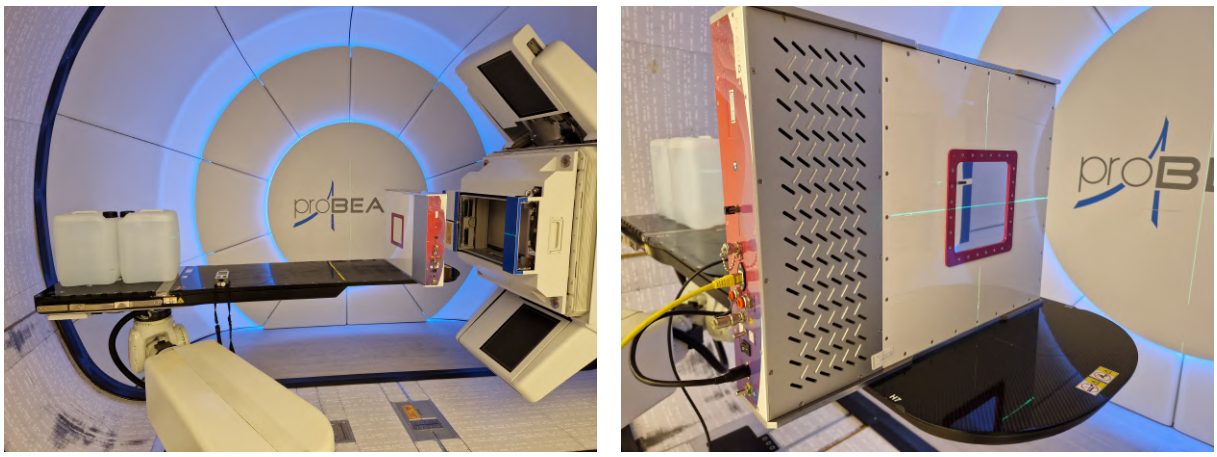

Figure 2.4: Experimental setup for the determination of the spot position accuracy with the FlashQ. Similarly to the alignment of the Lynx (Figure 2.2), the laser is used to align the surface of the FlashQ with the gantry.

Data analysis

As mentioned in section 2.2, the FlashQ has a temporal resolution of 1 ms, with each time step registering the detected number of counts for each of the 128 horizontal and 128 vertical strips. Hence, the positioning and movement of the pencil beam can be tracked over time. For each time step, an elliptical Gaussian least-squares fit is performed through Eq. 2.5, similar to the determination of the spot shape. However, for tracking and quantifying the exact spot position, the central coordinate (x_0, y_0) of the Gaussian fit is the only parameter of interest, as other fit parameters, like σ_x, σ_y and θ, do not influence the central spot coordinate. At each 1 ms time step, the optimal coordinates x_0 and y_0 are determined and recorded. This procedure for a single time step is referred to as one 'event'. The combination of all such events during the irradiation period allows for a complete spatiotemporal reconstruction of the PBS irradiation.

The next step is to identify and correlate each detected spot event with its respective coordinate from the list of irradiated spots. This allows for the analysis of the event-averaged spot parameters, of which the most important parameter is the event-averaged spot position. This process is complicated by the continuous scanning of the pencil beam, as events are also registered during transitions between spots. Therefore, for the determination of the event-averaged spot positions, these so-called 'intermediate spots/events' are computationally excluded by a filter to ensure that all analysed events correspond to a spot list coordinate. This filter imposes the following conditions for intermediate events:

1. The distance between the event and at least one of its two neighbouring events in time is greater than half the spot spacing. For large spot spacings, this distance equals the maximum distance possibly traversed between the two events, considering the scanning speed in both directions (see subsection 2.6.2).

2. The distance between both neighbouring events is greater than four times the spot precision, defined as the spatial standard deviation of all events corresponding to an event-averaged spot position.

3. The spatial derivative with respect to both neighbouring spots is either fully positive or negative, based on the assumption that the beam moves in a single forward direction when transitioning between spots.

After applying this filter, only events corresponding to irradiated spots from the spot list remain. For each spot position, all corresponding events are averaged, totalling up to 49 event-averaged spot positions, which are called 'detected spot positions'. The central detected spot position, aligned with the beam axis, is set to $(0,0)$ to facilitate the comparison between detected and planned spot positions. The detected spot position deviation for individual spots is calculated by subtracting the requested spot list coordinate from the detected spot coordinate. In the end, the spot position accuracy is defined and reported as the standard deviation of the distribution that is formed by all detected spot position deviations. Note that a geometric correction is applied to this distribution to account for any alignment issues of the FlashQ relative to the gantry, mainly to prevent overestimating the spot position accuracy.

2.3.3 Beam envelope

Purpose & Goal

Normally, the majority of measurements are taken at the gantry's isocentre since this point serves as the rotational centre for the gantry and offers a consistent reference for performing and comparing various measurements. This allows for the use of earlier measurement data for follow-up research, such as using the spot shape to determine spot position accuracy (as described in subsection 2.3.2). However, clinically, it is important to understand the characteristics of the proton beam not only at the isocentre but also upstream and downstream of this point. Any convergence or divergence of the proton beam spot shape impacts the dose distribution, especially with transmission beams, which can deposit significant doses beyond the planned treatment area, potentially endangering critical organs located distally and adjacent to the target. Therefore, the goal is to determine the spot shape at various distances relative to the isocentre, referred to as the proton beam envelope.

Method

Because the determination of the beam envelope solely compromises spot shape measurements, the Lynx detector is again used. Logically, the setup is identical to the spot shape determination (Figure 2.2), with the Lynx aligned at the isocentre, defined as $z = 0$ cm. The full beam envelope is determined by moving the Lynx along the z-axis, achieved by consecutively shifting the gantry table a specified distance from its starting position. Measurements of the spot shape are conducted at depths of $z = -20$, -10, -5, 0, 5, 10 and 20 cm. These values are considered clinically significant as larger distances usually extend outside the patient and are not needed for evaluation. At each depth, measurements are taken at nominal nozzle currents of 10, 75, 150, and 215 nA, providing an approximately equally spaced range within the FLASH regime and allowing for the evaluation of a potential current dependency of the beam envelope. Again, the amount of monitor units for each current is scaled such that approximately an equal amount of dose is delivered per irradiation.

Data analysis

For each measurement, the spot shape is determined using a least-squares fit of Equation 2.5, yielding values for σ_x, σ_y, and θ at each depth for each nozzle current. Then, a statistical evaluation is conducted to check for any dependency of the beam envelope on the nozzle current. This is combined with the conclusions from subsection 2.3.2, where a similar correlation between nozzle current and spot shape is investigated. The results are then plotted against the depth z. Finally, a linear least-squares fit is conducted to derive an equation representing the spot shape as a function of the depth in air.

2.3.4 Comparison Lynx and EBT3 film

Purpose & Goal

As discussed in previous subsections, the Lynx detector plays a critical role in accurately measuring parameters like the spot shape and beam envelope. However, according to the manufacturer's specifications, the Lynx is officially rated for proton energies up to 230 MeV [111]. Despite this, it is currently being utilised at 250 MeV. Given this deviation from recommended usage parameters, it is crucial to verify the detector's performance not only at this higher energy but also under the significantly higher dose rates encountered in FLASH measurements. Ensuring dose linearity, which is expected to be within $\pm 1.5\%$, is particularly important under these conditions to maintain the accuracy and integrity of the measurement results. Therefore, the goal is to assess the accuracy and reliability of the Lynx under conditions encountered in FLASH measurements.

Method

This study compares spot shape measurements obtained from both the Lynx detector and radiochromic EBT3 film. EBT3 film has been extensively used in a variety of FLASH-related experimental setups for both absolute and relative dosimetry, along with profile and depth-dose measurements [101, 120–125]. Moreover, it is usually selected for its high spatial resolution and its ability to capture a complete 2D dose distribution within a single pulse irradiation. However, the principal advantage for this investigation lies in the film's dose rate independent response [104, 126–128], making it a good standard for comparison at ultra-high dose rates. Nevertheless, it is essential to approach the use of radiochromic film in the dosimetry of UHDR proton beams with caution because optimal performance is achieved within a dose range of 0.2 to 10 Gy [112]. Beyond this range, there is a potential for overresponse behaviours [128, 129].

To allow for a direct comparison of spot shapes under the same conditions, both the Lynx detector and the film must be aligned at the gantry's isocentre, ensuring matching z-positions to prevent depth-related discrepancies. Consequently, the EBT3 film is positioned directly atop the centre of the Lynx detector, which is shown in Figure 2.5. This setup captures spot irradiations simultaneously on both detectors, allowing for straightforward spot shape comparisons. The measurement process consists of sequentially irradiating single proton beam spots onto both detectors. Four measurements are carried out, each at different nozzle currents of 10, 75, 150, and 215 nA, to evaluate potential dependencies on the nozzle current. The amount of MU is scaled such that approximately an equal dose is irradiated (< 10 Gy per irradiation). After each measurement, the irradiated film is replaced and stored in the dark to prevent the films from being left exposed to room light. Lastly, within 24 hours, the films are scanned and digitised with a 48-bit (16-bit per channel), 150 dpi flatbed colour scanner.

Figure 2.5: Experimental setup for the comparison between the Lynx and EBT3 spot shape measurements, in which the radiochromic film is placed directly on top of the centre of the Lynx' effective area.

Data analysis

To translate the scanned film image into a usable reading, the film response is assessed by calculating the net optical density. This optical density is then correlated to the dose using the film's calibration curve. For this analysis, only the red channel is used because it has the highest dose rate independence threshold and the steepest calibration curve [112, 129]. Both the Lynx and film data are used to determine the spot shape using Eq. 2.5 to ensure a fair comparison. Ultimately, for each irradiation, the retrieved optimal parameters σ_x, σ_y and θ for both detectors are compared.

2.4 Longitudinal relative dosimetry

Following the lateral relative dosimetry, this section focuses on longitudinal relative dosimetry measurements. Unlike lateral measurements, which are made perpendicular to the beam's direction, longitudinal dosimetry concerns itself with measurements along the direction of the beam, parallel to the z-axis, therefore aligning with the beam's travel from the source through the patient in clinical settings. Longitudinal dosimetry is vital for assessing how deeply the proton beam penetrates and where it delivers its maximum energy deposition — a key factor in effective radiation therapy planning. Note that, as with lateral dosimetry, all data initially captured here are measured, translated, and/or reported on a relative scale.

2.4.1 IDD

Purpose & Goal

Fundamentally, conventional proton therapy is built upon the unique energy deposition profile of proton beams, best understood through the integrated depth dose (IDD). Often referred to as the percentage depth dose (PDD) or depth-dose distribution (DDD), the IDD shows how protons release a significant part of their energy at the end of their path in the Bragg peak. This allows for targeting tumours with precision while preserving surrounding healthy tissues. Accurately measuring the IDD allows for dose distributions that conform to the complex shapes of tumours, providing the precise control crucial for optimising treatment efficacy. In the context of FLASH radiotherapy, particularly with transmission beams, the significance of this measurement slightly diminishes as the Bragg peak is intentionally positioned beyond the body. Nevertheless, the IDD remains an essential parameter for treatment planning systems, serving not only as a vital component in the initial design of therapy protocols but also as an important tool for ongoing quality assurance and verification purposes, such as determining the proton beam energy. The aim of this section is to accurately measure the IDD of the 250 MeV proton beam, using this data to assess both the stability and purity of the proton beam.

Method

In accordance with the AAPM TG-224 report [90], IAEA TRS-398 Code of Practice [130], and machine QA guidelines outlined by Spruijt et al. [91], the IDD of the 250 MeV transmission beam is measured in liquid water. For this purpose, the IBA Blue Phantom 2 is used [131]. Depicted in Figure 2.6, this water phantom system is usually employed for the commissioning and quality assurance of radiation beams, with exterior tank dimensions of 675 x 645 x 560 mm facilitating comprehensive measurements across the entire proton beam range. Furthermore, the measurements involve the use of the 34070 Bragg peak chamber (BPC) and the 7862 monitor chamber (MC). The waterproof BPC is secured within the internal detector holder, enabling external control of its positioning, while the MC is mounted directly at the entrance window, serving as the reference chamber. By slowly, but continuously scanning the BPC from its initial position to the end of the water phantom, the dose deposition relative to water depth is captured. To accommodate intensity variations in the proton beam, the ratio of readings from the BPC and MC is automatically calculated for each depth measurement. This ratio is then normalised to the maximum reading, producing the IDD curve when plotted against the water depth. To ensure reproducibility, IDD measurements for the 250 MeV proton beam are conducted three times. Additionally, single measurements for proton beams at 70, 160, 190, and 230 MeV are performed to enable the comparison with internal reference measurements at HollandPTC. All measurements are performed with the gantry fixed at 90 degrees, effectively excluding water surface effects, and at the lowest nominal nozzle current of 2 nA to minimise saturation effects in both the BPC and MC, thereby avoiding potential inaccuracies in readings. The examination of these saturation effects is explored in the subsection 2.4.2.

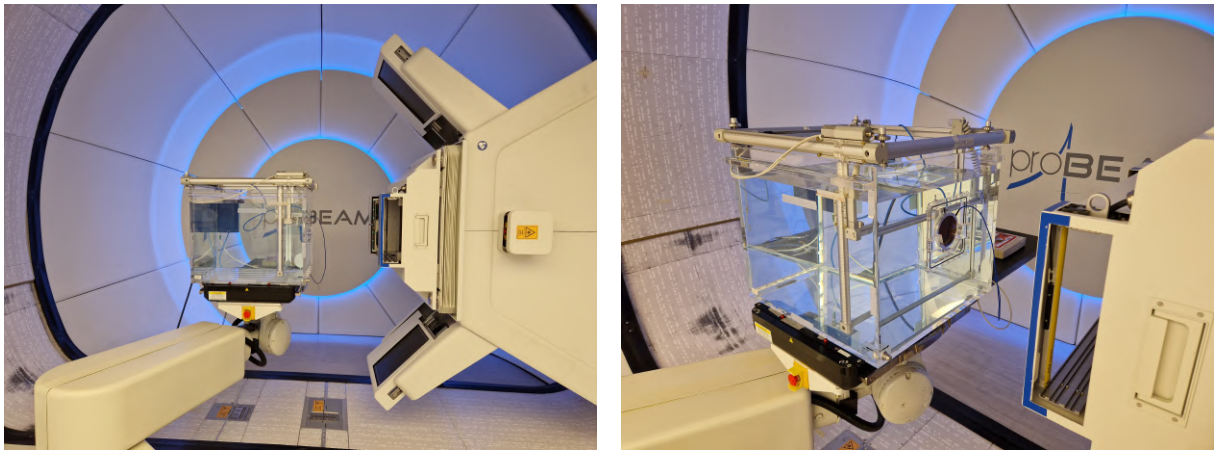

Figure 2.6: Experimental setup for integrated depth dose (IDD) measurements conducted with the IBA Blue Phantom 2 water phantom. The Bragg peak chamber is positioned within the phantom to record the depth-dependent dose deposition, while the monitor chamber is placed at the front, serving as the reference chamber.

Data analysis

As mentioned, the IDD is constructed by plotting the normalised reading from the BPC against the depth in the water. The range of the proton beam is quantified using the R_{80}-value, defined as the depth at which the radiation dose decreases to 80% of its maximum value in water. This depth corresponds to the mean projected range, representing the point at which half of the protons, which have undergone only electromagnetic interactions, have stopped [17]. This value consists of two components. First, the water depth in the phantom corresponding to the distal 80% dose level is determined via interpolation of the IDD. Second, the sum of the water equivalent thicknesses of all elements traversed by the proton beam is calculated and added, shown in Table A.2. Ultimately, the average R_{80}-value for the 250 MeV proton beam is calculated from the average of the repeated measurements.

Then, the purity of the proton beam is assessed based on its energy spectrum, which reflects the concentration of protons with a specific energy within the beam. This concentration is affected by the distinct characteristics of the accelerator, the beam guidance system, and, if in use, a collimator. Specifically, for the UHDR proton beam, high purity signifies that the majority of protons are approximately 250 MeV, with very little variation in energy levels. The Bortfeld function, a closed-form analytical model using Gaussians and parabolic cylinder functions, is employed to quantify the energy spectrum [16]. This function closely matches numerically calculated Bragg curves and is adapted to fit experimental depth distributions. The energy spectrum $\sigma_{E,0}$, defined as the standard deviation around the initial beam energy, is calculated from this fit, as documented in the appendix (subsection A.3.1). For verification purposes, this value is validated with similarly obtained energy distributions based on the lower energy proton beams.

2.4.2 Saturation effects BPC and MC

Purpose & Goal

The Bragg peak chamber and monitor chamber are both ionisation chambers that operate based on ionising radiation interacting with the gas within the chambers. Normally, the generated current is proportional to the amount of radiation passing through the chamber, allowing these devices to measure the intensity of the radiation beam. However, given that these chambers are typically designed for conventional radiotherapy settings, at ultra-high dose rates, the observed recombination effects can lead to an underestimation of the measured charge. Therefore, to investigate the effectiveness of both the Bragg peak and monitor chamber for FLASH irradiations, the aim is to quantify the saturation effects as a function of the nozzle current for both chambers.

Method

For the setup, several components are aligned along the central beam axis, as illustrated in Figure 2.7. The Bragg peak and monitor chamber are positioned consecutively to guarantee identical beam intensity exposure for each irradiation. The nozzle current is varied from 2 to 215 nA to effectively evaluate saturation effects over the entire nozzle current range, with incrementally increasing step sizes. For each measurement, the detected charge by each chamber is recorded using electrometers. However, to ensure consistent comparisons across different nozzle currents, the amount of monitor units is adjusted for each irradiation to maintain a roughly constant dose for each current, with the minimum intensity per spot being 100 MU for the highest nozzle current. This is verified with FlashQ, which is positioned at the start of the beam path as the reference detector and can provide insight into the beam intensity through the number of detected counts. Additionally, five RW3 plates, equating to 5 cm of water equivalent thickness, are positioned between the FlashQ and the chambers to stabilise the dose delivery [132]. This addresses the nuclear buildup effect in the entrance region, where the proton beam undergoes a rapid increase in nonelastic reactions upon transitioning from air to water. To ensure a stable mix of secondary particles, which typically forms after traversing a few centimeters of water or an equivalent thickness, five solid water plates deemed sufficient [17].

Data analysis

The experimental data consist of charge readings from the BPC and MC, both in nC, along with dimensionless count readings from the FlashQ for each nozzle current. To adjust for any variations in the delivered dose per nozzle current, the charge readings from both detectors are normalised by dividing them by the corresponding FlashQ counts. This normalisation process yields a measure unaffected by the magnitude of the beam intensity, thereby providing a clearer understanding of the saturation effects relative to the nozzle current. For each dataset, a second-degree polynomial fit is applied to model the trends. As the step size is increased with higher

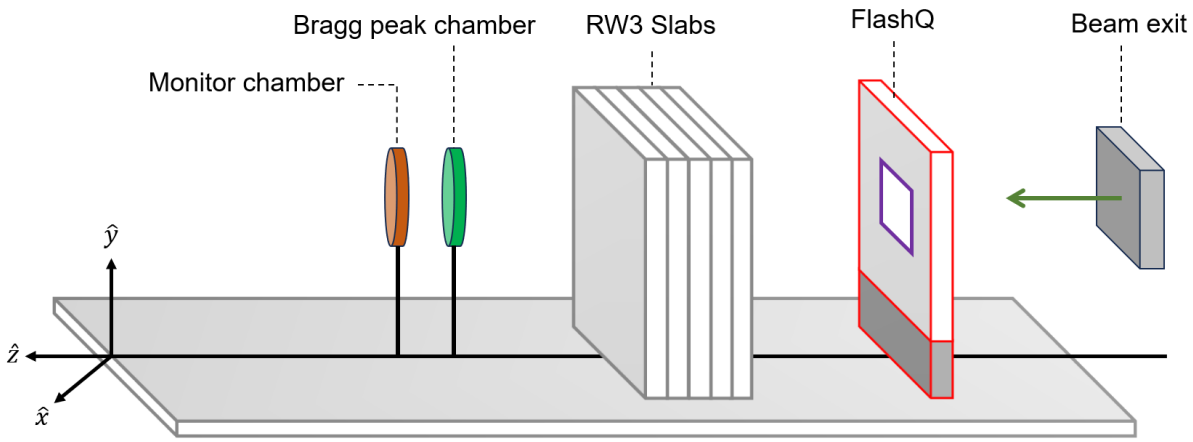

Figure 2.7: Experimental setup for measuring saturation in the Bragg peak chamber and monitor chamber. The FlashQ is added as a reference monitor detector, and five RW3 plates are positioned to counteract any instabilities due to the nuclear buildup effect.

nozzle currents, the data points for nozzle currents greater than 100 nA are given double the weight. This adjustment prevents the initial measurement points from disproportionately influencing the polynomial fit. A further normalisation step involves dividing all data by the theoretical zero-current value determined through the fit, representing the hypothetical charge reading in the absence of any saturation.

2.5 Absolute dosimetry

Building upon the foundation in the sections on lateral and longitudinal relative dosimetry, this section transitions to focusing on absolute dosimetry. Absolute dosimetry is crucial for accurately quantifying the actual radiation dose absorbed by the medium, which is essential for verifying treatment integrity and ensuring patient safety. This section establishes the basis for retrospectively determining the delivered dose for all measurements conducted within this thesis by correlating monitor units to specific dose values.

2.5.1 Output

Purpose & Goal

In clinical settings, the TPS calculates the optimised dose distribution plan in Gray. However, this plan must be translated into MU per pencil beam spot, enabling the gantry to deliver the correct dose to the patient. This translation necessitates a precise calibration factor, which ensures that the dose delivered in Gray per MU is accurately known and verified; without this, correct dose delivery cannot be assured. In the context of FLASH radiotherapy, it is particularly crucial to assess the implications of saturation effects in the NMC, where the dose delivered is determined by both the nozzle current and MU — not solely by the quantity of MU (see subsection 2.1.1). Therefore, the objective is to determine the delivered dose per MU, and specifically how it varies with changes in the nozzle current.

Method

In accordance with reference dosimetry guidelines from IAEA TRS-398 [130], the output measurements are conducted with the Advanced Markus detector in a water phantom. With its sensitive volume of 0.02 cm^3, the Advanced Markus is deemed suitable for reference dosimetry, striking a balance between necessary sensitivity and precise point-dose measurement. Its application in FLASH measurements has also been extensively endorsed due to its dose rate independent response, as described in multiple studies [64, 105, 109, 133–136]. To avoid the discrepancies associated with uncertain water-to-plastic fluence correction factors, a liquid water phantom is used instead of plastic phantoms for more reliable absorbed dose determinations [130].

The experimental setup is shown in Figure 2.8. The Advanced Markus is positioned in the water phantom at a water equivalent depth of 2 cm (see Table A.4) and aligned with the central beam axis. Spot lists of 5 x 5 cm^2 are irradiated with nominal nozzle currents of 10, 75, 150 and 215 nA, and with a spot spacing of 5 mm to ensure a relatively even dose distribution. For each spot list, the MU is scaled such that uniform field doses of approximately 10.5, 12, 15 and 20 Gy are achieved, totalling up to 16 irradiations. The Advanced Markus signal is read out using an electrometer and nominal chamber voltage of 300 V. Note that the workings of the detector for FLASH measurements as a function of the chamber voltage is discussed in subsection 2.5.2.

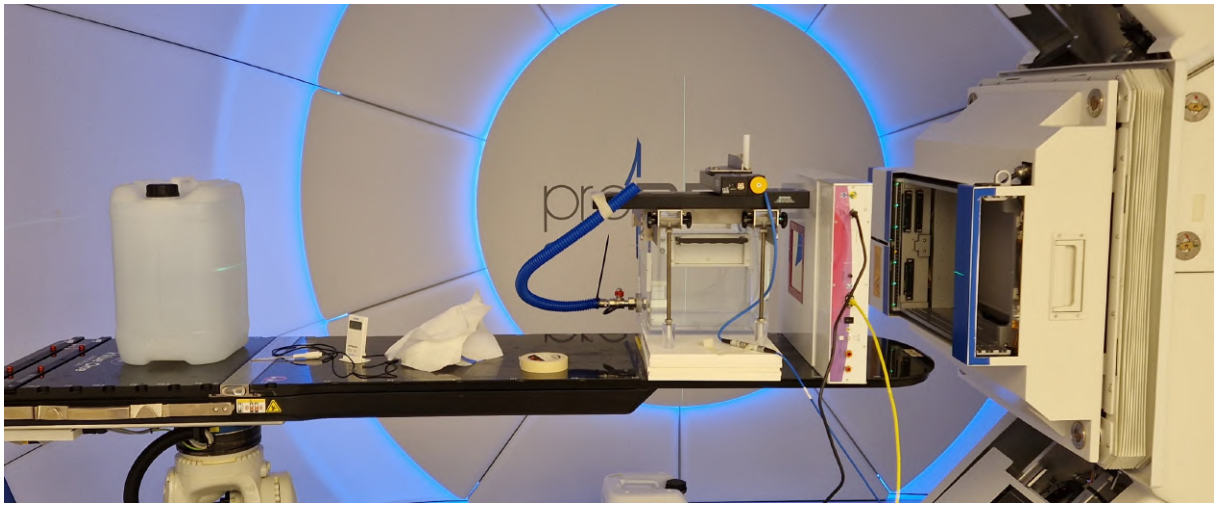

Figure 2.8: Experimental setup for the output measurements. The Advanced Markus is positioned in the water phantom at a depth of 2 cm WET (of which calculations are found in Table A.4). A thermometer is placed on the gantry table to determine the pressure and temperature correction factors.

Data analysis

Each irradiation's output from the Advanced Markus (measured in nC) is converted to Gy using the 'absorbed-dose-in-water calibration coefficient' $N_{D,\mathrm{w}}$, determined to be 1.444 (± 1.0%) Gy · nC^{-1} through prior calibration with a ^{60}Co gamma radiation beam. Additionally, a correction factor $k_{p,T}$ compensates for air temperature and pressure variations. The calculated dose represents the total field dose at the ion chamber's effective measurement point, assumed to be aligned with the central beam axis and thus with the central spot at $(x, y) = (0, 0)$ cm. However, the field dose includes contributions from other spots due to the close spot spacing intended to create a uniform dose field. To isolate the dose from a single spot and thereby determine the dose per MU for individual proton beam spots, the 'field-to-peak ratio' is calculated as follows:

$$\text{Field-to-peak ratio} = \frac{D_{\text{field}}}{D_{\text{peak}}} \tag{2.6}$$

Here, D_{peak} is the dose contribution from a single planned spot at a specific position, and D_{field} is the total field dose at that position, including contributions from nearby spots. For this experiment, the ratio is computed by simulating the two-dimensional dose distribution from the same spot list irradiated during the conducted measurements. The spot shape (subsection 2.3.1) and beam envelope (subsection 2.3.3) measurements in air are used as input parameters for the simulation to estimate the spot shape at a water equivalent depth of 2 cm and assess the impact of neighbouring spots. Ultimately, by dividing the Advanced Markus reading by this field-to-peak ratio and the total amount of MU per spot, the delivered dose per MU for a single spot is retrieved.

2.5.2 Saturation effects Advanced Marcus

Purpose & Goal

As outlined in subsection 2.5.1, the Advanced Markus, a plane-parallel ionisation chamber, is noted for its suitability in absolute dosimetry for FLASH measurements due to its dose rate-independent response. The charge detected by the chamber is converted into an absorbed dose reading using the absorbed-dose-in-water calibration coefficient, $N_{D,\mathrm{w}}$. This coefficient is determined under stringent calibration conditions, including a specific chamber voltage setting on the Advanced Markus. Although a higher chamber voltage could reduce

recombination effects — which is beneficial for FLASH measurements — deviating from the calibrated conditions may compromise the accuracy of $N_{D,w}$. Therefore, this section aims to explore whether the Advanced Markus exhibits saturation effects at the recommended chamber voltage of 300 V.

Method

For this experiment, the setup used for the output measurement, as illustrated in Figure 2.8, is used. To investigate saturation effects, similar protocols are followed, involving spot lists of 5 x 5 cm^2 with a 5 mm spot spacing and an effective field dose of approximately 15 Gy. However, the experiment includes varying the chamber voltage at 50, 100, 200, 300, and 400 V. Measurements are carried out using the maximum nominal nozzle current of 215 nA. For each irradiation, the charge detected by the Advanced Markus (in nC) at the different chamber voltages is retrieved using the PTW Unidos E electrometer [137].

Data analysis

The readings from the Advanced Markus are plotted against the various chamber voltages to visualise potential saturation effects related to changes in voltage. Lastly, all data points are normalised against the benchmark reading taken at 300 V.

2.6 Temporal dosimetry

In this last section, the temporal dosimetry measurements are explained. Temporal dosimetry distinguishes itself from conventional dosimetric approaches by focusing on the timing of dose delivery, a critical factor in FLASH radiotherapy. Unlike conventional characterisations that primarily assess the magnitude of absolute dose and spatial distributions, temporal dosimetry evaluates the temporal aspect and precision with which radiation doses are delivered. This aspect is fundamental in FLASH radiotherapy where exceeding the specific dose rate threshold of 40 Gy/s is crucial for achieving the desired widening of the therapeutic window.

2.6.1 Spot dwell time

Purpose & Goal

The FLASH effect incorporates both absolute and temporal dosimetric elements. Thus, alongside the quantification of the absolute dose per MU, the timing aspect is equally critical. This temporal aspect is quantified by the spot dwell time t_{dwell}, which is defined as the irradiation time per MU. Spot dwell time not only aids in managing dose delivery within the temporal constraints of FLASH radiotherapy but also provides deeper insights into the behaviour of the nozzle monitor chamber under potential saturation scenarios. Consequently, the purpose of this measurement is to assess the spot dwell time as a function of nominal nozzle current and MU/spot and, through this analysis, explore the saturation behaviour of the NMC.

Method

Measurements are conducted using the FlashQ, similar to the setup depicted in Figure 2.4. To investigate the relationship between spot dwell time and nominal nozzle current, 13 single spot irradiations are executed with nominal nozzle currents ranging from 5 to 215 nA. Each irradiation ensures sufficient data collection with a minimum of 2000 MU per spot. For examining the spot dwell time against MU per spot, 25 single spot irradiations are performed across nozzle currents from 2 to 215 nA, adjusting the MU per spot from 1358 to 100 to maintain a consistent dose across different spot weights.

Data analysis

For each irradiation, the spot dwell time is determined with the FlashQ's temporal resolution of 1 ms. Each irradiation's duration is divided by its respective MU per spot to calculate the spot dwell time per MU, which is then analysed in relation to the nominal nozzle current. This is done by employing a least-squares fit to identify the specific nominal nozzle current at which the NMC begins to exhibit saturation. The relationship between spot dwell time and MU, which does not require normalisation, is directly plotted to explore the linearity on the range in which the NMC experiences saturation.

2.6.2 Scanning speed

Purpose & Goal

In PBS proton systems, irradiation is executed via a predefined list of spot coordinates. For each coordinate, the proton beam is guided to the spot positions across the isocentre by the gantry's steering magnets, ensuring precise dose delivery to the targeted areas. The speed at which these steering magnets can move the beam from one spot to the next is referred to as the scanning speed. This speed is a critical attribute of the steering magnets and plays a significant role in the treatment's temporal dynamics. Specifically, higher scanning speeds can reduce the total irradiation time, potentially increasing the local dose rates. Hence, the primary aim of this section is to determine the scanning speeds of the ProBeam system in both the x- and y-direction.

Method

Two distinct sets of measurements are conducted to evaluate and quantify the scanning speed. First, the ratio between the scanning speeds in the x- and y-directions is assessed using the Lynx detector. A 2 x 2 grid pattern with a spot spacing of 100 mm, which simulates a complete square-like configuration, is irradiated with a nominal nozzle current of 215 nA. Due to the continuous scanning of the proton beam between spot positions, this setup allows for the determination of individual scanning intensities in both the x- and y-directions.

Second, the scanning speed is quantified with the FlashQ detector aligned with the isocentre, similar to the determination of the spot position from Figure 2.4. Seven spot lists with different spot spacings are irradiated to capture the scanning speeds, which are expected to be 5 m/s in the x-direction and 20 m/s in the y-direction. Given the 1 ms temporal resolution of the FlashQ, the smallest detectable spot spacing is determined and set at 5 mm, while the largest is 100 mm, which marks the maximum distance where two distinct spots can still be detected on the detector's sensitive area. For closely spaced spot spacings (5, 7.5, 10 mm), a 7 x 7 grid of spots is used, totalling 49 spots. For larger spot spacings (30, 50, 70, 100 mm), the spot positions are configured in a 2 x 2 grid pattern. Each list is tested under nozzle currents of 10, 75, 150, and 215 nA to investigate a correlation with nozzle current.

Data analysis

For the determination of the intensity-based ratio, the relative intensities of the Lynx data are summed over the x- and y-axis separately, resulting in two graphs depicting intensity as a function of the position on the detector along each axis. Then, the segments between the spot positions where smearing is evident (see section 2.1) are determined. Within these intervals, the average intensity values for both the x- and y-axis are calculated. The intensity readings between spot positions are indicative of the scanning speed; a slower scanning speed yields a higher intensity due to prolonged beam presence over each detector pixel. With the assumption that the beam moves solely in a forward direction, the ratio of intensities (x- over y-direction) is computed, enabling the correlation of scanning speeds across these axes.

For the quantification of scanning speed using the FlashQ, an analytical approach akin to the one used for determining spot positions (see subsection 2.3.2) is adopted. In this method, for each FlashQ time step, an elliptical least-squares fit is conducted to determine the central spot coordinate of each detected event. While the analysis of spot positions aims to correlate specific events to defined spot locations, omitting intermediate events that result from the continuous scanning of the beam, the approach for these scanning speed measurements incorporates the intermediate events. By calculating the spatial distance (Δx or Δy) between two neighbouring intermediate events and with the temporal resolution Δt of the FlashQ known, the scanning speed of the proton beam between spots can be retrieved.

For the precise measurement of scanning speed, the filtering process used in calculating spot positions is adapted. Previously used to exclude intermediate events during the analysis of spot positions, this filter is now utilised to specifically identify and register these intermediate events. However, to compute Δx or Δy, it is essential to have at least two adjacent intermediate events between two spot positions, which is imposed as a new, fourth condition. Then, for each irradiation, the distances between pairs of neighbouring intermediate events are determined and averaged. This process yields a distinct velocity value, v_x, for the x-direction and, given adequately large spot spacings, v_y for the y-direction per spot list. As the experimental method includes varying spot spacings and nominal nozzle currents, these factors are statistically investigated to explore their correlation with scanning speed.

2.6.3 Dose rate

Purpose & Goal

The determination of the dose rate is of intrinsic importance in FLASH radiotherapy, primarily due to the critical dose rate threshold of 40 Gy/s required to achieve the FLASH effect. This threshold underscores the necessity for precise dose rate measurements to ensure the therapeutic benefits of FLASH radiotherapy are fully realised. However, the quantification of dose rates is complicated by the variety of definitions and measurement methodologies that exist, making this a significant area of research in its own right. In this context, this research focuses on investigating two widely used dose rate definitions: the instantaneous and the field-averaged dose rate. This is crucial for verifying if the radiation delivery meets the FLASH criteria. By correlating the nozzle current directly with the (instantaneous) dose rate, this section aims to establish an approach that allows for retrospective confirmation of whether specific measurements were conducted within the FLASH regime.

Method

This research incorporates the output measurements detailed in subsection 2.5.1, where the dose delivery per MU is assessed using the Advanced Markus detector positioned within a water phantom, illustrated in Figure 2.8. A total of 16 measurements are conducted across four nominal nozzle currents: 10, 75, 150, and 215 nA, with each current tested at four distinct field doses. These output measurements are then integrated with the spot dwell time data from subsection 2.6.1, which provides the irradiation time associated with each MU.

Data analysis

First, with the delivered dose per MU (subsection 2.5.1) and time per MU (subsection 2.6.1) established, the instantaneous dose rate (IDR) for each output measurement can be retrieved by dividing the former by the latter. Second, as described in subsection 1.1.3, the field-average dose rate (FADR) is calculated by dividing the central axis field dose (subsection 2.5.1) by the total field irradiation time, measured with the FlashQ. For each nozzle current, both dose rates are averaged individually over all four irradiations, yielding two average dose rates for each nominal nozzle current. Subsequently, a linear fit is applied to these values, enabling the determination of the specific nominal nozzle current necessary to achieve the 40 Gy/s dose rate threshold.

2.6.4 Dose rate constancy

Purpose & Goal

Maintaining the planned dose rate during spot scanning is critical to ensure consistent treatment outcomes in FLASH radiotherapy. Variations in dose rate can significantly affect the efficacy of treatment; hence, understanding and controlling these variances is paramount. Specifically, the ProBeam system has been reported to exhibit a day-to-day variance of approximately ±10%. This level of fluctuation necessitates regular verification of the nozzle current to ensure adherence to planned treatment parameters. Hence, the primary aim of this research is to assess and quantify dose rate constancy across three dimensions:

1. Day-to-day variance: Analyse the consistency of the dose rate from one day to the next, assessing systemic stability between different measurement sessions.
2. Beam-to-beam variance: Evaluate fluctuations in the dose rate between different irradiations during the same measurement session to assess intraday consistency.
3. Variance within the beam: Investigate the uniformity of the dose rate within a single beam, identifying any deviations that occur during each irradiation.

Method

This analysis is conducted with the FlashQ, which, as noted in subsection 2.1.1, has been positioned as the initial detector in most experimental setups, serving as a reference monitor chamber. The FlashQ records counts over time, offering insights into the instantaneous dose rate for each irradiation. This is achieved by calibrating the FlashQ counts per second against the detected nozzle current, a process detailed in subsection 2.6.5. Thus, instead of relying solely on the nominal (requested) nozzle current, the actual detected nozzle current for each irradiation is determined. Given that the nozzle current is directly proportional to the instantaneous dose rate, quantifying and comparing deviations in the detected nozzle current across various measurement sessions

effectively evaluates the (instantaneous) dose rate constancy. In total, nozzle current values from 120 irradiations, collected across six different measurement sessions spanning four months, are retrospectively analysed. To ensure reliability, all included irradiation data sets contain at least 500 MU (such that sufficient data points are available), have no temporary beam stops, and are fully irradiated on the sensitive area of the FlashQ.

Data analysis

For every irradiation in each session, both the nominal and the FlashQ-detected nozzle currents are recorded. The deviation from the nominal nozzle current is then calculated for each irradiation using

$$\Delta I = \left(\frac{I_{det}}{I_{nom}} - 1 \right) \cdot 100\% \tag{2.7}$$

with ΔI the nominal nozzle current deviation (in %), I_{det} the detected nozzle current (in nA) and I_{nom} the nominal/requested nozzle current (in nA). This calculation provides a measure of the deviation between the requested and the actual nozzle currents.

To analyse the day-to-day variation, irradiations and their corresponding nominal nozzle current deviation values are categorised by measurement session, forming distinct distributions for each day. This enables the analysis of trends and dose rate variations across different days. The analysis includes three statistical tests, accommodating different data assumptions/conditions. First, a one-way ANOVA assesses differences in means, assuming normal distribution and equal standard deviations. Second, the Alexander-Govern test is used when equal variances are not guaranteed. Third, the Kruskal-Wallis test evaluates differences in medians, assuming that the distributions are not normally distributed. For all tests, the null hypothesis states that all distributions come from one common distribution, indicating no significant variance in dose rate between measurement sessions. The alternative hypothesis, on the other hand, suggests that the individual distributions cannot originate from a common distribution, thereby indicating significant differences in the dose rate across different sessions. The level of significance for rejecting the null hypothesis is set at 0.05.

For the beam-to-beam variation, the standard deviation of the nozzle current deviations is calculated for each day's distribution of measurements. These individual standard deviations reflect the variability in dose rate from beam to beam within each measurement session. To determine the overall beam-to-beam variation, these daily standard deviations are then averaged, providing a measure of fluctuation across different beams.

The variance within the beam is determined by calculating the standard deviation of the nozzle current (in nA) within each irradiation. To understand this variation in the context of overall current levels and make it independent of the actual magnitude of the nozzle current, the relative variance is computed by dividing the standard deviation by the mean detected current for each irradiation. This total relative variance, averaged across all treatments, defines the overall variance within the beam.

2.6.5 Coupling FlashQ and Faraday cup

Purpose & Goal

Due to significant recombination effects in the nozzle monitor chamber at high currents, the FlashQ is used as a reference monitor chamber. However, the FlashQ quantifies the signal as counts per time step. To accurately reflect the actual detected nozzle current, it is necessary to correlate the FlashQ counts per second with the detected current. Therefore, this section aims to calibrate the FlashQ counts to the detected nozzle current.

Method

This calibration is done with a Faraday cup (FC), which provides the actual detected nozzle current as a function of time. The Faraday cup is known for its dose rate independent response, making it ideal for FLASH measurements [64, 65, 105, 114]. Two versions of the FlashQ, called 'original' and 'loan', are calibrated. These are used interchangeably across all measurement sessions. Visual distinctions between the two are highlighted in Figure A.6. The calibration of the original FlashQ is performed on the gantry, shown in Figure 2.9. This process involves 13 irradiations with nozzle currents gradually increasing from 5 to 215 nA to secure an accurate calibration across the entire current range. Both the FlashQ and FC are aligned with the central beam axis during this process, ensuring they measure the same beam intensity for a direct comparison. The calibration procedure is replicated for the loan FlashQ on the experimental beamline at HollandPTC, using a similar number of irradiations but with requested nozzle currents ranging from 2 to 800 nA.

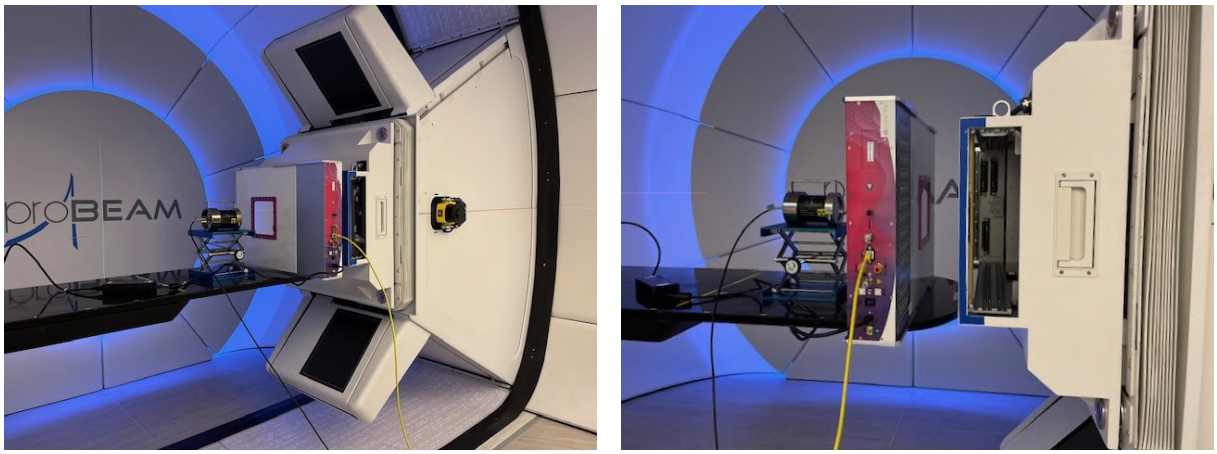

Figure 2.9: Experimental setup for the calibration of the original FlashQ on the gantry. Both the FlashQ and Faraday cup are aligned with the central beam axis to capture the full beam intensity.

Data analysis

To establish the calibration factor between the FlashQ and the FC, each irradiation's FC reading (in nA) is paired with the FlashQ reading (counts per second). To ensure sufficient data, each irradiation is conducted with a minimum of 2000 MU, providing a sufficiently long irradiation time. However, as the total irradiation time varies for various nozzle currents, this poses a challenge due to the Faraday cup's resolution being dependent on its exposure time. Larger time steps resulting from lower FC resolutions can lead to the occurrence of "rising spots" — instances where the beam is not consistently on throughout the entire time resolution window. To ensure a consistent analysis irrespective of the FC's resolution, any rising spots are excluded from the analysis. Then, the leakage current is filtered from the data after which the average nozzle current value from the stable plateau period is used as the definite reading for each irradiation. A similar approach is applied to the FlashQ readings: any rising spots, indicating that the beam has not fully activated within the time step window, are also excluded. The FlashQ counts per second are then calculated by dividing the total integrated counts number by the effective irradiation time. To establish the calibration factor, the counts per second from the FlashQ are plotted against the current from the Faraday cup for both FlashQ devices. A linear least-squares fit is then performed on each set of data, linking the FlashQ counts to the FC current for both devices.

2.6.6 Continuous scanning parameters ProBeam

Purpose & Goal

A continuous proton beam can result in unintended dose delivery between spot transitions, a factor not accounted for by treatment planning systems. While current systems can pause the beam between spot positions using a vertical deflector, this approach extends the overall irradiation time and reduces the local dose rate. However, it has been observed that the Varian ProBeam system still pauses the proton beam temporarily for larger spot spacings. This study aims to identify the parameters that enable the proton beam to scan continuously without interruptions.

Method

All measurements are carried out using the Lynx, which is well-suited for this research due to its ability to provide images directly after an irradiation is finished. This feature is important, given the repetitive nature of these measurements, where the influence of various parameters needs to be methodically investigated. This requires numerous irradiations and adjustments of parameters during the measurement session itself. Each irradiation is performed with a square 2 x 2 spot list with various spot spacings, as long as the smearing of the beam remains identifiable. All measurements are performed at a nominal nozzle current of 215 nA to maximise beam intensity, which enhances the visibility of smearing effects. Two parameters of interest are identified.

The first parameter to consider is I_{mag}*-tolerance*, which sets a tolerance level between the expected and actual steering magnet currents needed for the steering magnets to work properly. These magnets play a crucial role in directing the beam to its intended spot position by moving it away from the central beam axis in the xy-plane. For each spot, the gantry system predicts the necessary current for the steering magnets to move

the proton beam from one spot to the next. However, there is often a discrepancy between the predicted and measured steering magnet current. This maximum allowable discrepancy is defined by the 'Imag_x_tolerance' and 'Imag_y_tolerance' settings in the gantry system. Typically, this value is set at 1200 mA in the x-direction and 1600 mA in the y-direction. Generally, the greater the distance needed to move between spots, the larger the required current, and consequently, the larger the discrepancy becomes. The standard tolerance values are sufficient for short distances, but for bigger distances, the discrepancy surpasses these limits, consequently halting the irradiation.

The second parameter, *ConstRaster*, sets the maximum spot spacing for which continuous scanning is achieved. In the gantry settings, this is specified as 'ConstRasterX' and 'ConstRasterY', both set at 10 mm. Practically, this means that for spot spacings less than 10 mm, the beam remains on during transitions between spots. However, for spacings exceeding this limit, the beam is temporarily stopped, resulting in a non-continuous scanning mode akin to 'spot mode'.

Data analysis

For both identified parameters, the standard values are adjusted while other parameters remain constant to determine their influence on the behaviour of the gantry. Ultimately, from the various irradiated Lynx images, conclusions are drawn about the parameter values that should be adopted for the realisation of the continuous scanning UHDR proton beam.

3

Results

3.1 Lateral relative dosimetry

3.1.1 Spot shape

Figure 3.1a shows an example dose distribution from the 250 MeV proton beam spot, measured in air at the isocentre. The experimental data has been reproduced with a single 2D elliptical Gaussian fit (subsection 2.3.1) from which the spot shape parameters σ_x, σ_y and θ are retrieved. Figure 3.1b shows the corresponding overlaid least-squares fitting contour plot, which matches the relative lateral distribution well. This is further confirmed by the residual plot, shown in Figure 3.1c. With an average maximum residual of 3.3% observed across 20 measurements, a single two-dimensional Gaussian fit is deemed suitable to characterise the spot shape in air.

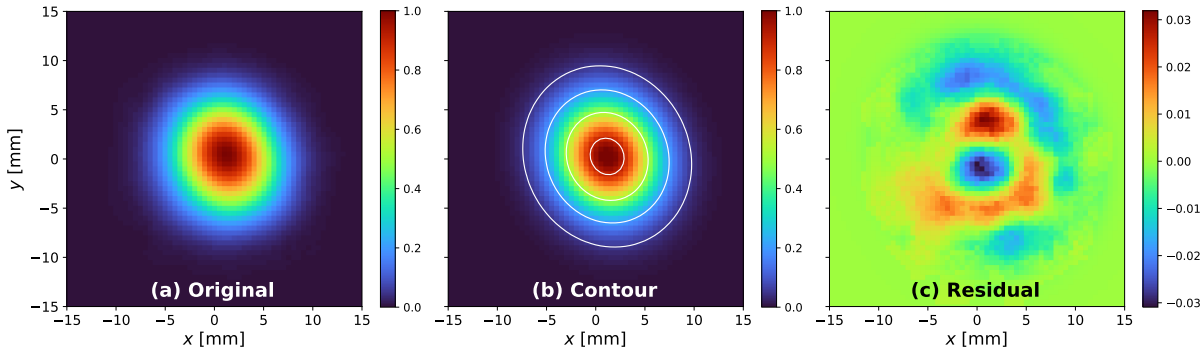

Figure 3.1: Relative dose distribution for a single UHDR proton beam spot in air, irradiated at the isocentre with 215 nA. (a) Original: the original lateral dose distribution. (b) Contour: the original distribution with the overlaid least-squares fitting contour plot. (c) Residual: the residual differences by subtracting the optimally fitted dose distribution from the original.

Table 3.1 presents the mean optimal spot shape parameters derived from ten repeated measurements for each nominal nozzle current. The spot shapes varied between 3.28 mm and 3.46 mm for σ_x and between 3.83 mm and 3.89 mm for σ_y. With a maximum relative uncertainty in the mean of 1.8% for σ_x at 10 nA, the spot shape demonstrates stability across multiple irradiations and nozzle currents. It should be noted that the uncertainty in the individual measurements due to the Lynx's effective resolution of 0.5 mm is not accounted for, in order to emphasise the small magnitude of the uncertainty in the mean.

Regarding the statistical evaluation, normality tests are first performed on the distributions of repeated measurements for σ_x, σ_y and θ, with separate tests conducted for each of the two different nozzle currents. These tests produce p-values that are bigger than the significance level of 0.05, leading to the assumption that the distributions are normally distributed. Second, to assess the potential dependency on the nozzle current, two other statistical tests are conducted, of which the full results are shown in Table A.1. With p-values smaller than 0.05, the individual distributions of the spot width σ_x and height σ_y for each nozzle current do not originate from the same distribution, suggesting a dependency of both parameters on the nozzle current. On the contrary, the spot angle θ demonstrates no significant dependence on the nozzle current.

Table 3.1: Spot shape versus nominal nozzle current. The mean values of the σ_x, σ_y and θ are based on 10 repeated measurements for each nozzle current. Corresponding standard deviation in the mean (SD) and the relative variance with respect to the mean (SD/Mean) are also noted. Due to the 2π-periodicity of the spot angle, no relative deviation is given.

	σ_x			σ_y			θ	
Nozzle current [nA]	Mean [mm]	SD [mm]	SD/Mean [%]	Mean [mm]	SD [mm]	SD/Mean [%]	Mean [deg]	SD [deg]
10	3.36	0.06	1.8	3.85	0.02	0.5	-16.0	4.5
215	3.42	0.01	0.3	3.87	0.01	0.3	-17.1	2.0

3.1.2 Spot position

The determination of the spot position involves several steps. First, the centre coordinate (x_0, y_0) of each beam spot event is identified, which is crucial for accurate spot positioning and tracking. This coordinate is retrieved through a least-squares fit of a single two-dimensional Gaussian model, effectively capturing the spot shape as established in subsection 3.1.1. However, due to the FlashQ's limitation of providing only summed integral counts per strip along both axes — unlike the Lynx, which offers a complete two-dimensional intensity array — the spot angle is assumed to be constant to ensure a unique solution for each event. Figure 3.2 presents two example distributions from the FlashQ's x- and y-strips during a single event (1 ms) of an irradiation, along with the overlaid results from the least-squares fitting. The single Gaussian fit closely aligns with the FlashQ readings, enabling precise tracking of the pencil beam over time, which is the second step in the process.

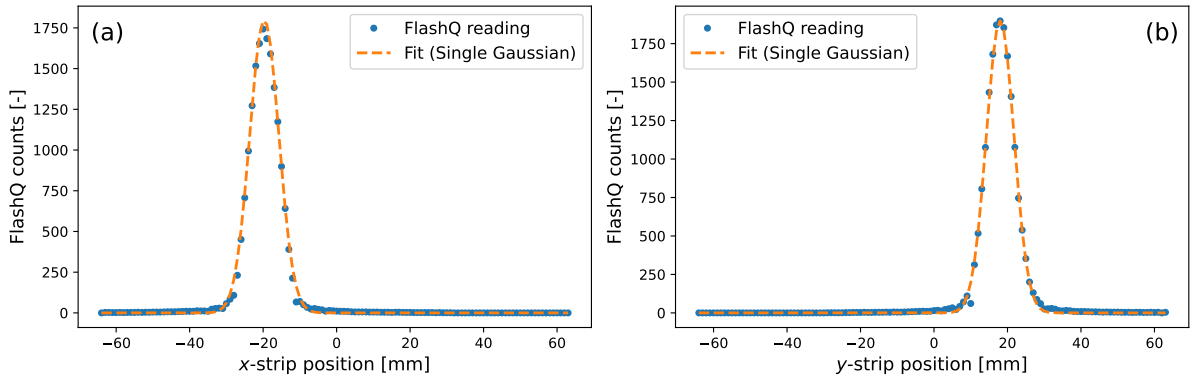

Figure 3.2: The lateral distribution of the (a) x- and (b) y-strip FlashQ readings for a single event with the single Gaussian least-squares fit overlaid. The FlashQ is placed at ISOC, after which the measurement is conducted at 215 nA.

Figure 3.3 shows the full spatiotemporal reconstruction of a single irradiation measured by the FlashQ. Each dot represents the measured spot position of a single time event. The clusters of small dots represent individual planned beam spots from the spot list. The number of events recorded per spot depends on the dwell time of the planned spot, with the Varian ProBeam system requiring at least 3 ms to successfully irradiate a planned spot position. Hence, with a time resolution of 1 ms, a single cluster contains at least three dots/events. Despite the spot list containing only predefined coordinates, the observed irradiation field displays a distinctive snake-like and/or zigzag pattern, a result of the scanning method employed. During the scanning of a column of planned spots, the x-position is precisely adjusted in predefined 10 mm increments, while the y-position remains fixed. This results in the detection of intermediate events during transitions, where the beam continues to remain active as it moves between spots in the respective direction.

The third step involves identifying and grouping events that correspond to the same planned spot. The presence of intermediate events complicates this task, as they do not directly match any predefined spot coordinates. To mitigate this issue, the filtering technique explained in subsection 2.3.2 is used to exclude these intermediate events from the analysis of event-averaged spot positions. The outcomes of this approach are shown in Figure 3.4, displaying the spatiotemporal reconstruction without any intermediate events. This visualisation closely represents what an irradiation in spot mode would resemble. The filter significantly simplifies the calculation of event-averaged processes since all events now correspond to a spot list coordinate.

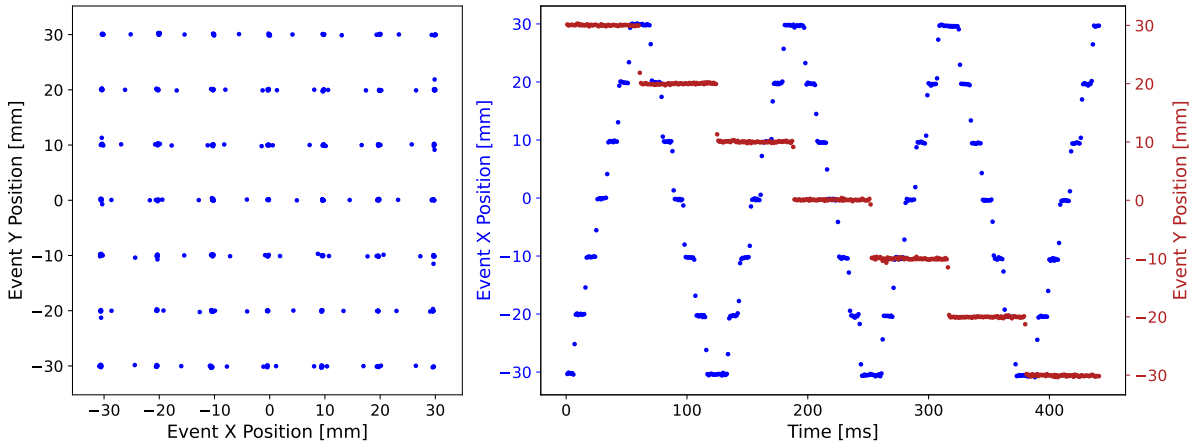

Figure 3.3: The full spatiotemporal reconstruction of a single irradiation in raster mode with intermediate events, measured with the FlashQ. Left: a scatter view of the retrieved per-event (x_0, y_0) coordinates. Right: the per-event x- and y-coordinates as a function of time. The irradiation comprises a uniform 6 x 6 cm^2 field with 10 mm spot spacing, conducted at a nominal nozzle current of 10 nA.

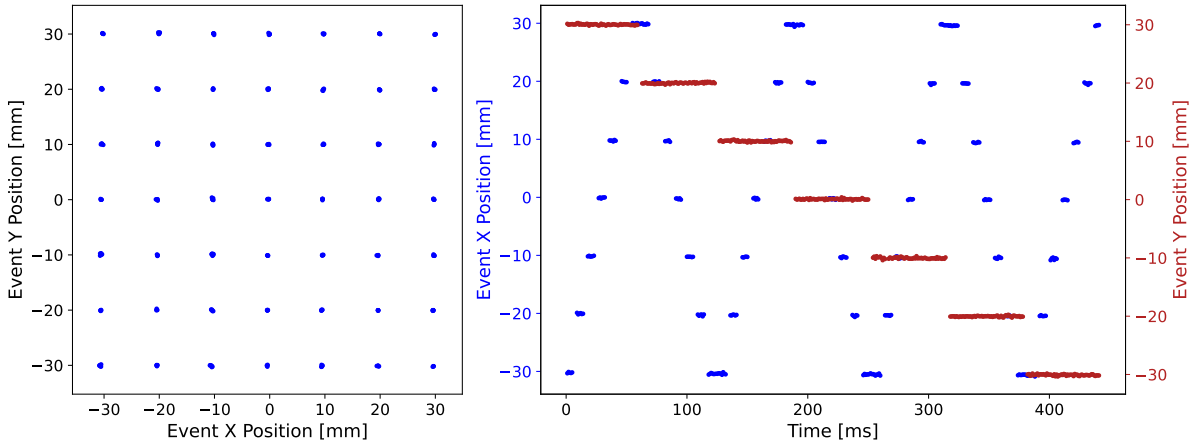

Figure 3.4: The full spatiotemporal reconstruction of a single irradiation in raster mode, but with the intermediate events computationally filtered out. Left: a scatter view of the retrieved per-event (x_0, y_0) coordinates. Right: the per-event x- and y-coordinates as a function of time. The irradiation comprises a uniform 6 x 6 cm^2 field with 10 mm spot spacing, conducted at a nominal nozzle current of 10 nA.

Figure 3.5a shows the event-averaged spot position deviation, quantified as the discrepancy between the event-averaged and the planned spot positions, plotted against the planned spot list coordinates. The data are separated by different nozzle currents and the x- and y-directions to examine potential correlations with spot position deviation. Initially, no statistically significant correlation between spot position deviation and nozzle current variations is found. Consequently, linear regression analyses are independently conducted for the x- and y-direction data, without segregating by nozzle currents, to further explore underlying patterns. These fits show that the magnitude of the spot position deviation increases linearly for planned spots located further away from the central beam axis. This is primarily attributed to an alignment issue of the FlashQ with the isocentre. Specifically, the FlashQ is placed distally to the isocentre. The steering magnets guide the proton beam, resulting in a small incident angle at the FlashQ's sensitive area. This angle becomes more pronounced for spot positions that are planned further from the central beam axis - essentially, the farther a spot is from the centre, the greater the angle required to reach it. As the FlashQ is positioned at a greater distance from the isocentre, the beam must travel a longer path to reach it. This extended travel distance results in larger spot position deviations, which increase is approximately linear with the distance of the spots from the central beam axis. The disparity in gradient observed between the x- and y-direction fits can be attributed to the shorter focal length in the x-direction, as discussed in section 2.1. To compensate for this misalignment, a geometric correction is applied to adjust for any alignment discrepancies of the FlashQ.

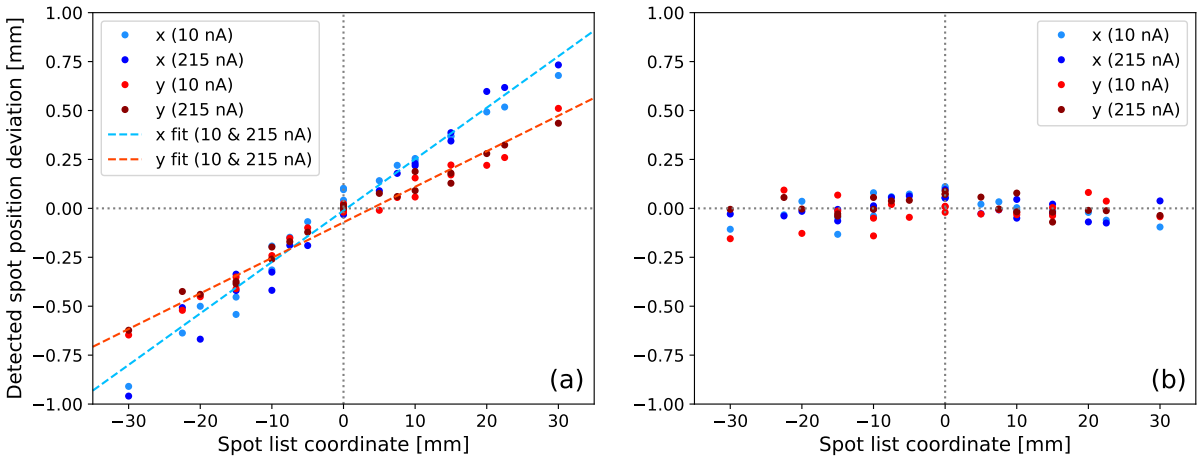

Figure 3.5: The spot position deviation between the detected and the planned spot plotted against the planned spot list coordinate (a) before and (b) after the geometric correction. All data points correspond to a planned spot $x-$ or y- position from three irradiated 7 x 7 spot fields with spot spacings of 5, 7.5 and 10 mm. Measurements are performed with the FlashQ and conducted at both 10 and 215 nA.

Figure 3.5b shows the spot position deviation after the geometric correction. This correction accounts not only for the additional distal distance from the isocentre but also for an unintended tilt of the gantry table around the z-axis (roll), attributed to uneven weight distribution. A gantry table angle of $0.3 \pm 0.1°$ was detected, which agrees with the 0.4 degrees reported by the monitoring system. After the correction, the data points uniformly distribute around the zero line. Ultimately, the spot position accuracy is quantified by the standard deviation of this distribution, measured at 0.06 mm, which translates to a 99% confidence interval of 0.15 mm.

3.1.3 Beam envelope

Figure 3.6 shows the beam envelope, i.e. the spot shape as a function of position from the isocentre, in air. Although measurements are performed at four different nominal nozzle currents, all data points are averaged over the nozzle current. The beam envelope extends over a range from -20 to 20 cm from the isocentre and exhibits a linear trend. The optimal linear fits for the envelope, presented in Equation 3.1, are as follows:

$$\begin{aligned} \sigma_x &= -0.014z + 3.380 \\ \sigma_y &= -0.013z + 3.838 \end{aligned} \tag{3.1}$$

with z the distance with respect from the isocentre in cm, and σ_x and σ_y given in mm. No significant correlation was found between the spot angle θ and position.

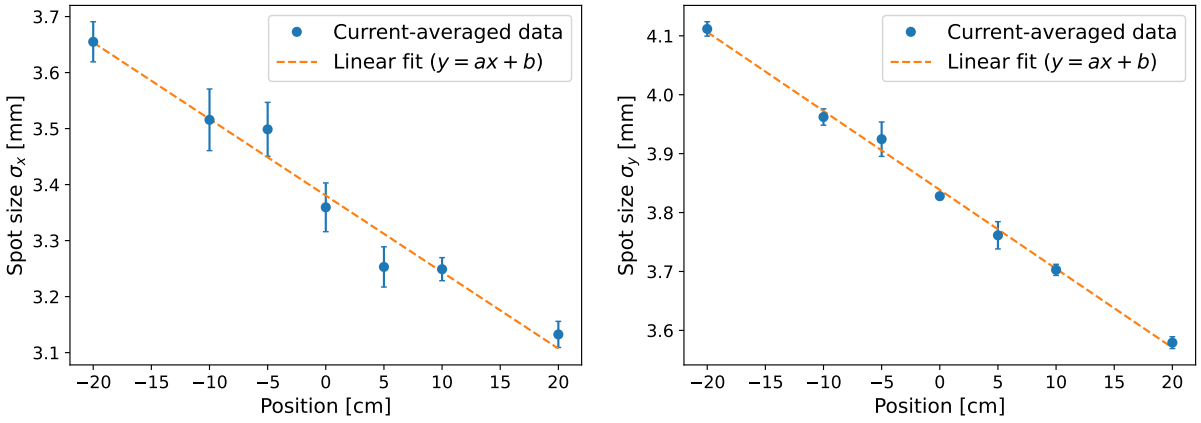

Figure 3.6: Beam envelope of the 250 MeV proton beam in air. The spot sizes σ_x and σ_y are averaged over the nozzle current and are plotted against the relative position with respect to the gantry's isocentre ($z = 0$ cm), with linear fit included. Positions towards the nozzle are represented by positive x-axis values. The error bars represent the uncertainty due to averaging over the nozzle current. The non-averaged data points for all nozzle currents can be found in Figure A.1.

3.1.4 Comparison Lynx and EBT3 film

As part of the procedure to assess the suitability of the Lynx detector for FLASH measurements, its accuracy is cross-checked against the Gafchromic EBT3 film, which is known for its dose rate independence. Both detectors are subjected to a single beam irradiated at four different nozzle currents, followed by an elliptical two-dimensional Gaussian least-squares fitting to determine the spot shape parameters. The results, presented in Table 3.2, show the optimal parameters obtained from both detectors, including calculations of both absolute and relative differences relative to the Lynx. Generally, the film retrieves higher values than the Lynx. However, with relative differences of 0.9% for σ_x and 2.6% for σ_y, these discrepancies are considered minimal. They likely result from a combination of the Lynx's effective resolution of 0.5 mm and the analytical and numerical methods used to interpret the film data, which will be discussed in subsection 4.1.4.

It should be noted that the Lynx detector does suffer from saturation effects when individual detector pixels are subjected to prolonged exposure to high-intensity beams. This issue can be mitigated by reducing the aperture of the Lynx, which limits the beam's exposure and decreases brightness. However, this adjustment introduces a trade-off between ensuring sufficient detector response and avoiding saturation. In this thesis, nearly all measurements are conducted using an iris setting of 10%, with the maximum exposure per spot adjusted according to the nozzle current. For instance, exposures reaches up to 200 MU/spot at 215 nA and up to 1200 MU/spot at 10 nA.

Table 3.2: Spot shape data for both EBT3 film and the IBA Lynx as a function of the nominal nozzle current. For each nozzle current, a single measurement is performed, including both the EBT3 film and IBA Lynx. All measurements are analysed with a least squares method based on Eq. 2.5, regardless of the detector type. The absolute difference is difference between the the IBA Lynx and EBT3 film, the relative difference is calculated with respect to the IBA Lynx. Due to the 360°-periodicity of the spot angle, no relative deviation is given. The main findings are written in bold.

	EBT3 Film			IBA Lynx			Absolute diff.			Relative diff.	
Nozzle current [nA]	σ_x [mm]	σ_y [mm]	θ [deg]	σ_x [mm]	σ_y [mm]	θ [deg]	σ_x [mm]	σ_y [mm]	θ [deg]	σ_x [%]	σ_y [%]
10	3.47	3.95	-26.6	3.40	3.82	-23.3	0.07	0.13	3.3	2.1	3.5
75	3.38	3.90	-21.4	3.35	3.82	-17.2	0.03	0.08	4.2	0.9	2.1
150	3.36	3.91	-16.4	3.33	3.81	-16.7	0.03	0.10	-0.3	0.7	2.7
215	3.39	3.93	-24.4	3.38	3.85	-21.1	0.01	0.08	3.2	0.1	2.1
Mean	3.40	3.94	-21.4	3.37	3.82	-19.6	0.03	0.10	**2.6**	**0.9**	**2.6**

3.2 Longitudinal relative dosimetry

3.2.1 IDD

Figure 3.7 shows five integrated depth dose curves, measured with the Bragg peak and monitor chamber in the Blue Phantom 2 water phantom for proton beam energies of 70, 160, 190, 230 and 250 MeV. Each curve exhibits a characteristic Bragg peak, with the depth in water increasing proportionally with higher proton energies, as anticipated. Upon comparison with internal commissioning reports, the R_{80}-values for proton beam energies from 70 to 230 MeV, as depicted in Figure 3.7, indicate a slight underestimation of the Bragg peak depth with a mean discrepancy of -0.9 mm.

Figure 3.8a shows an overlay of three repeated 250 MeV IDD curves. The consistent overlap of all three curves across the entire range underscores the stability of this proton beam's range. The found R_{90}- and R_{80}-values for the 250 MeV proton beam in liquid water are determined as 37.8 ± 0.1 and 37.9 ± 0.1 cm respectively, with the uncertainty reflecting both the variability in repeated measurements and corrections for water equivalent thickness. The determined longitudinal profile penumbra ($R_{80} - R_{20}$) measures 0.5 ± 0.1 cm. The found R_{80}-value closely matches the theoretical value of 38.4 cm, determined through the Bortfeld equation from Equation 1.2. Inversely, the found value corresponds to a proton beam energy of 248.5 MeV.

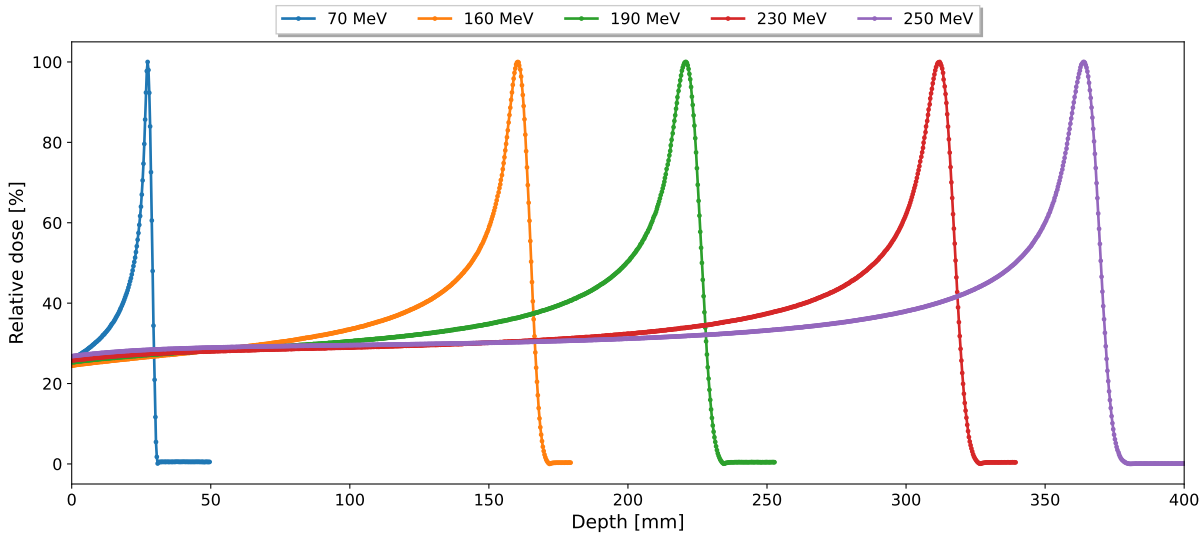

Figure 3.7: Single integrated depth dose curve for five different proton beam energies, measured with the Bragg peak and monitor chamber in the Blue Phantom 2 and conducted at a nominal nozzle current of 2 nA. The gantry angle is set at 90°.

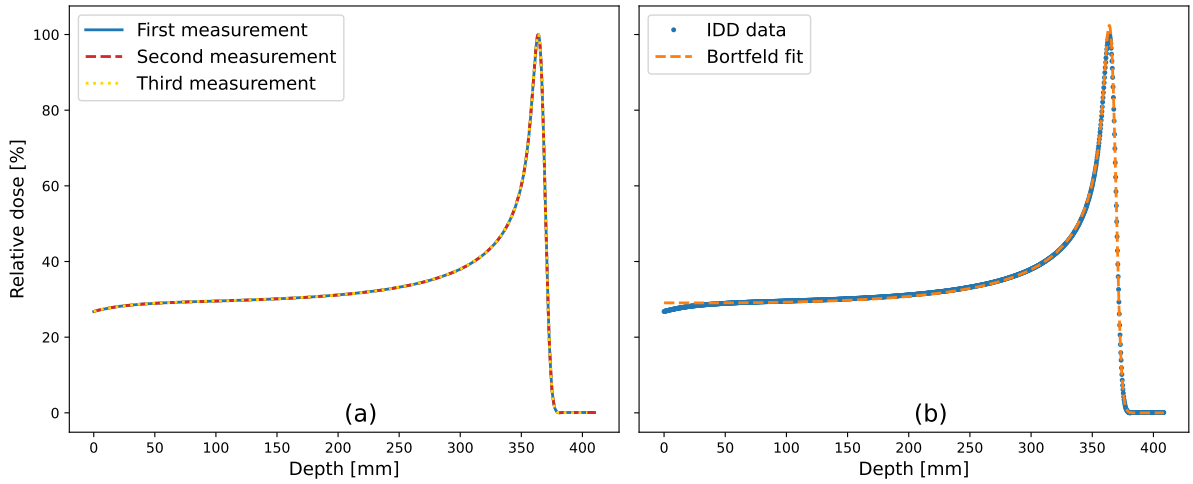

Figure 3.8: Integrated depth dose curves containing (a) an overlay of the three repeated measurements for a 250 MeV proton beam and (b) a single 250 IDD curve with overlaid a Bortfeld least-squares fit, explained in section A.3.1. The measurements are performed with the Bragg peak and monitor chamber in the Blue Phantom 2 and conducted at a nominal nozzle current of 2 nA. The gantry angle is set at 90°.

Figure 3.8b shows the 250 MeV IDD curve alongside the optimally fitted least-squares Bortfeld fit, which is utilised to assess the energy purity of the proton beam, as detailed in subsection A.3.1. The energy purity is quantified by $\sigma_{E,0}$, defined as the width of the Gaussian energy spectrum around the initial proton beam energy and is retrieved as one of the fitting parameters. Besides a slight overestimation in the entrance domain and at the Bragg peak, the fit generally aligns well with the IDD data points. Through analysis of the optimally fitted curves, the energy purity is determined at 14.8 ± 0.8 MeV.

3.2.2 Saturation effects BPC and MC

The IDD curves are generated by calculating the normalised ratio of the readings from the Bragg Peak and the monitor chamber. Verifying the response from both detectors as a function of nominal nozzle current is essential to correct for any potential saturation effects ensuring the accuracy of results. Figure 3.9a shows the saturation curves of both the BPC and MC as a function of nominal nozzle current, fitted with a second-degree polynomial function to describe their respective saturation behaviours. The fits correspond well with the normalised readings from each detector, revealing that while the BPC exhibits no saturation across the entire range of nominal nozzle currents, the MC begins to show signs of saturation at lower currents.

Figure 3.9b shows the differential readings between the two chambers, calculated to determine the nominal nozzle current at which the discrepancy between the readings exceeds 0.5%. With an R^2-value of 0.994, the difference in reading between both detectors is accurately described by a linear fit. The saturation threshold is identified at 23 nA. To ensure precision in accounting for deviations in nozzle current (see subsection 3.4.4), the FlashQ is used to measure the actual detected nozzle current. The actual detected nozzle current corresponding to the threshold where the difference exceeds 0.5% is established at 18 nA, shown in Figure A.2.

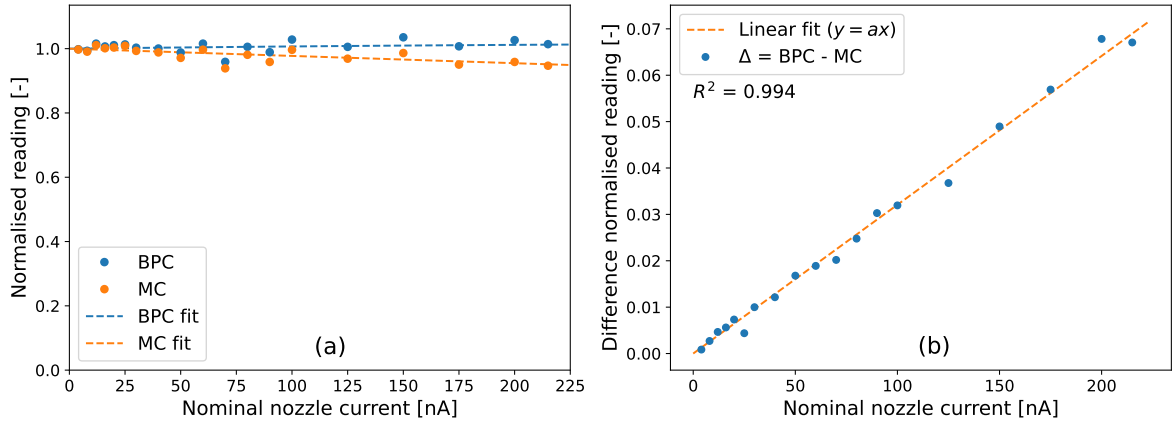

Figure 3.9: (a) Saturation curves for the Bragg peak chamber (BPC) and the 7862 Monitor Chamber (MC) against the nominal nozzle currents. Each detector is modelled with a second-degree polynomial fit. Data points are normalised relative to FlashQ counts, with those above 100 nA assigned double weight. (b) The difference Δ between the normalised readings from the BPC and MC, accompanied by a linear fit. Error bars, representing uncertainties (u(BPC) = 0.05 nC, u(MC) = 0.1 nC, u(FlashQ counts) = 5% of the reading), are considered in the analysis but omitted from the figure for clarity.

Figure 3.10 shows the Bragg peak curves from four IDDs measured at different nominal nozzle currents. This analysis is conducted to investigate the impact of MC saturation on the IDD. Due to the asymmetry of the Bragg peak, a third-degree polynomial is employed to model the complete zoomed-in curves shown in Figure 3.10. For higher nominal nozzle currents, the relative height of the IDD increases. This increase is attributed to MC saturation at higher currents. Since the IDD is calculated by the ratio between the BPC and MC readings, the ratio increases if the MC baseline reading does not rise proportionally to the BPC reading for increasing nozzle currents due to saturation. This effect is amplified when the BPC reading significantly increases in the Bragg peak regime, whereas the MC reading remains stationary at the front of the phantom. Consequently, the higher ratio results in a higher relative Bragg peak value. However, the convergence value for a hypothetical 0 nA measurement is found to be only 0.025% lower than at 2 nA. This difference is deemed insignificant, concluding that a nozzle current of 2 nA is sufficient for accurately measuring IDD curves.

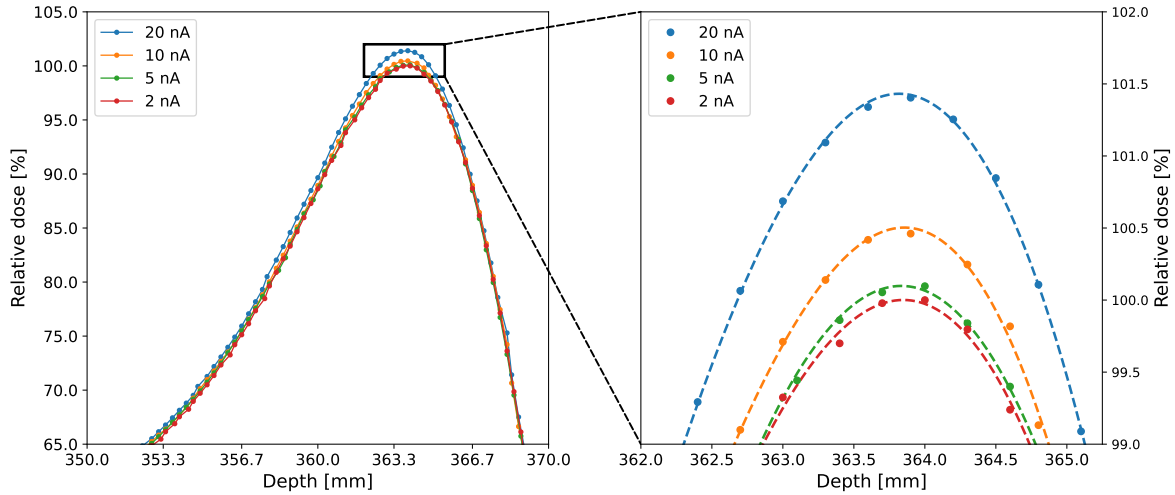

Figure 3.10: Figure of the 250 MeV Bragg peak for four nominal nozzle currents. All curves are normalised against the maximum reading of the 2 nA measurement. The dashed lines in the right subplot represent separate third-degree polynomials used to model the Bragg peak, while no fit is included in the left subplot.

3.3 Absolute dosimetry

3.3.1 Output

The output measurements are conducted in liquid water at a depth of 2 cm WET to determine the dose per MU. Initially, the field-to-peak ratio (Equation 2.6) is calculated to assess the contribution of a single spot relative to the entire dose field, influenced by neighbouring spots. Figure 3.11a shows a computationally simulated 5 x 5 cm^2 uniform dose field with a spot spacing of 5 mm. Each red dot represents a planned spot position. A uniformly distributed dose within the 50%-isodose line is achieved due to the tight spot spacing, which is optimal for dose measurements using the Advanced Markus. Figure 3.11b shows the dose cross section along the x-axis at $y = 0$ from Figure 3.11a. Individual Gaussian curves depict the dose contribution from each spot, while the thicker black curve represents the total field contribution. This cross section enables the determination of the field-to-peak ratio, with D_{field} and D_{peak} extracted from the simulation. The computed field-to-peak ratio for this specific field setup with 5 mm spot spacing is 3.317. Subsequent analysis confirms that this ratio remains consistent irrespective of the field size and MU per spot, provided the field size is large enough and the spot weights are equal, ensuring a uniform dose field is achieved.

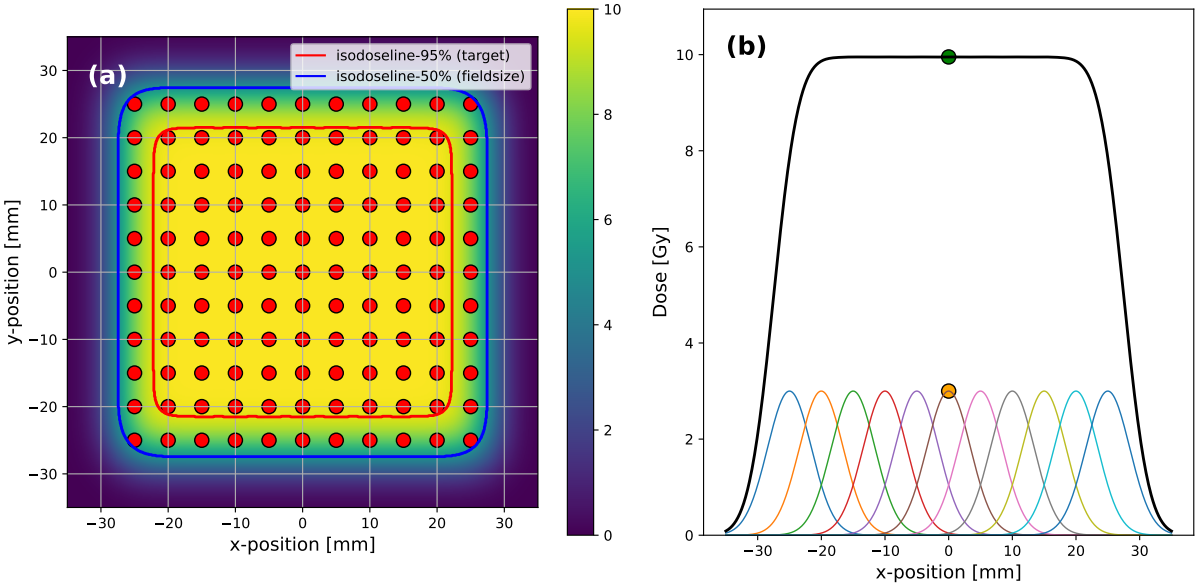

Figure 3.11: (a) The simulated two-dimensional dose distribution of 5 x 5 cm^2 uniform dose field with spot spacing of 5 mm at 2 cm depth in air. Each red dot represents a planned spot position. The spot shape and beam envelope data from subsections 3.1.1 and 3.1.3 respectively are used to simulate the dose distribution. (b) The cross section of the simulated dose distribution from 3.11a along the x-axis at $y = 0$. The smaller curves correspond to the dose distribution of the individual spots, while the thicker black curve is the total field dose contribution. The green dot marks the field dose D_{field} and the orange dot denotes the individual spot peak dose D_{peak}, both at $(x, y) = 0$ cm.

With an average air temperature of 19.8 °C and an atmospheric pressure of 1000.8 hPa, the correction factor $k_{p,T}$ is 1.012 [130]. Combined with both the absorbed-dose-in-water calibration coefficient $N_{D,w}$ and other correction factors (e.g. ion recombination factor k_s and polarity correction k_{pol}), the total correction factor for calculating the delivered dose (in Gy) from the Advanced Markus reading (in nC) is determined at 1.466.

Figure 3.12a shows the delivered dose per MU as a function of the nominal nozzle current, which is retrieved by dividing the central axis dose reading by the field-to-peak ratio and the MU per planned spot. The dose per MU varies from 0.0041 Gy/MU at 10 nA to 0.0466 Gy/MU at a nominal nozzle current of 215 nA. Two notes must be made. First, the dose delivery behaviour is influenced by the saturation state of the NMC system (explained in subsection 2.1.1). For a non-saturating NMC, observed at 10 nA, the dose per MU remains constant. However, at higher beam intensities (75, 150, and 215 nA), the NMC saturates. In this saturated regime, the dose per MU increases linearly with increasing nominal nozzle current. Hence, a linear fit is performed on the data points corresponding to the saturated regime (excluding the 10 nA data point). This yields a factor of $(2.15 \pm 0.02) \cdot 10^{-4}$ Gy MU^{-1} nA^{-1}, relating the nominal nozzle current and dose per MU within the saturated NMC range. Then, given that the dose per MU in the non-saturated regime is constant, an estimation of the nominal nozzle current at which the NMC starts saturating can be made. This threshold is found to be 18.8 nA.

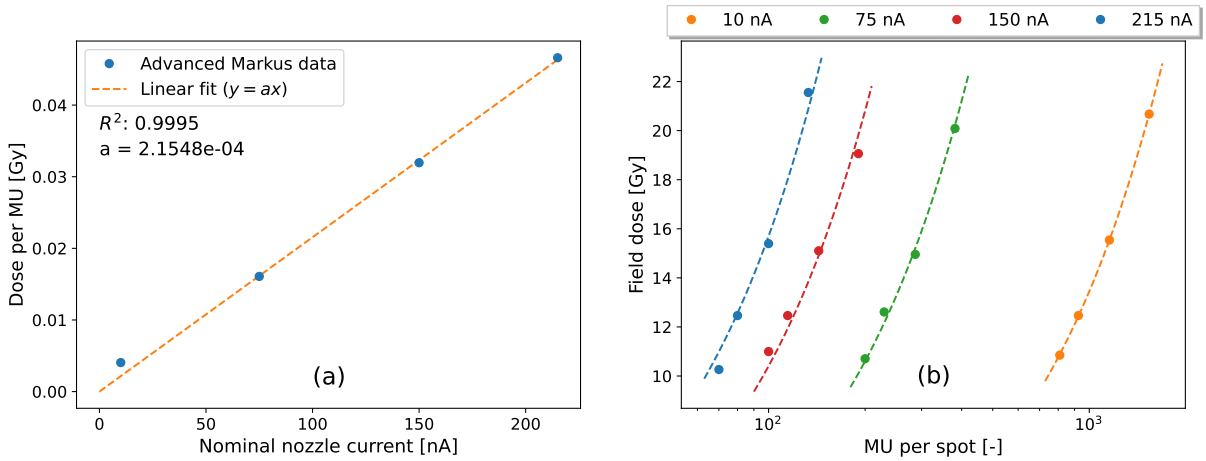

Figure 3.12: (a) The delivered dose per MU versus nominal nozzle current. Each data point represents the average value obtained from four uniform dose fields with varying dose levels. The linear fit shown applies only to the saturated NMC regime (75, 150, and 215 nA) because dose per MU exhibits linear dependence on nominal nozzle current only within this range. (b) The field dose as a function of the MU per spot, including linear fits for each nozzle current. The x-axis is shown on a log scale for improved visualisation.

Second, while the initial analysis explored the relationship between dose per MU and nominal nozzle current (as shown in Figure 3.12a), this approach may not be entirely accurate due to discrepancies between nominal and detected currents (shown in subsection 3.4.4). Therefore, for a more precise analysis, the FlashQ is used to retrieve the detected current for each irradiation. This approach compensates for nozzle current variations and yields an average value of $(2.75 \pm 0.02) \cdot 10^{-4}$ Gy MU^{-1} nA^{-1}. Similar to the value for the nominal nozzle current, this value is only valid within the saturated NMC regime, as the dose per MU remains constant for a non-saturated NMC. This value is retrieved by multiplying the calibration factor with the detected nozzle current threshold value, resulting in an output factor of $4.1 \cdot 10^{-3}$ Gy MU^{-1}.

Lastly, Figure 3.12b shows the field dose plotted against the MU delivered per spot. Each nominal nozzle current has a corresponding linear fit overlaid on the data points, demonstrating a good linear relationship between field dose and MU per spot regardless of the requested nozzle current. This signifies that the field dose scales linearly with the amount of MU delivered per spot, independent of the nominal nozzle current.

3.3.2 Saturation effects Advanced Marcus

Figure 3.13 shows the detector response as a function of the chamber voltage. A stable reading is observed at voltages of 200 V and above, indicating minimal saturation effects within this range, suitable for FLASH measurements. These findings align with observations by Lourenço et al. and Zou et al., who report negligible ion recombination effects at 300 V [138, 139].

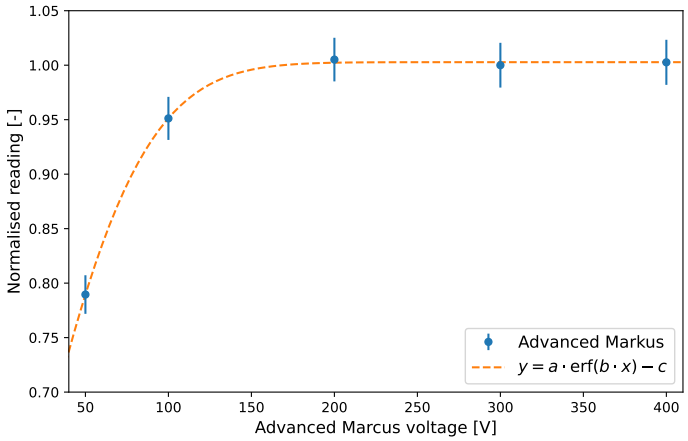

Figure 3.13: Normalised reading of the Advanced Markus detector as a function of the applied chamber voltage. The error bars represent the normalised uncertainty of the PTW Unidos E electrometer, ($u(Q)$ = 0.5% reading + 1 digit) [137].

3.4 Temporal dosimetry

3.4.1 Spot dwell time

Figure 3.14a shows the spot dwell time per MU as a function of the nominal nozzle current, measured by the FlashQ detector. Two domains are identified. For nominal nozzle currents below 20 nA, the spot dwell time exhibits an inverse-proportional relationship to the beam current, consistent with expectations when the nozzle monitor chamber is not saturated and efficiently collects all generated charge, denoted in Eq. 2.1 and 2.2. This capability ensures consistent dose delivery per MU across varying nozzle currents. In contrast, for beam currents exceeding 20 nA, the spot dwell time converges to a constant value, indicating saturation in the nozzle monitor chamber where the charge collection rate becomes nearly steady. Through Equations 2.3 and 2.4, this saturation leads to a direct proportionality between t_{dwell} and MU/spot, consequently causing the dose delivered to depend on both the total MU per spot and the nozzle current. For the saturated nominal nozzle current range, a constant dwell time of 0.0483 ms per MU is established, computed as the average of the dwell times for beam currents exceeding 20 nA for each MU/spot setting. Furthermore, the dashed curve represents the theoretical inverse-proportional relationship between spot dwell time and the nominal nozzle current in the absence of saturation. The transition point where the non-saturated fit equals the constant saturated spot dwell time, calculated at 18.4 nA, marks the threshold nominal nozzle current at which saturation begins. This value is comparable within 1% to the threshold of 18.8 nA identified from the output measurements, as discussed in subsection 3.3.1. Note that, after accounting for discrepancies between the nominal and detected nozzle currents, the threshold value adjusts to 15.7 nA. The corresponding curve of the spot dwell time per MU as a function of the detected nozzle current is found in Figure A.3.

Figure 3.14b shows the saturated spot dwell times plotted against the MU per spot, measured by the FlashQ. For this, the saturated dwell time of 0.0483 ms is taken. With an R^2-value greater than 0.99, this measurement demonstrates a strong linear relationship between both parameters. This reflects the anticipated behaviour where the charge collection by the nozzle monitor chamber is proportionally calibrated to the requested MU. Moreover, this linearity confirms the consistency of the NMC's response under saturation conditions.

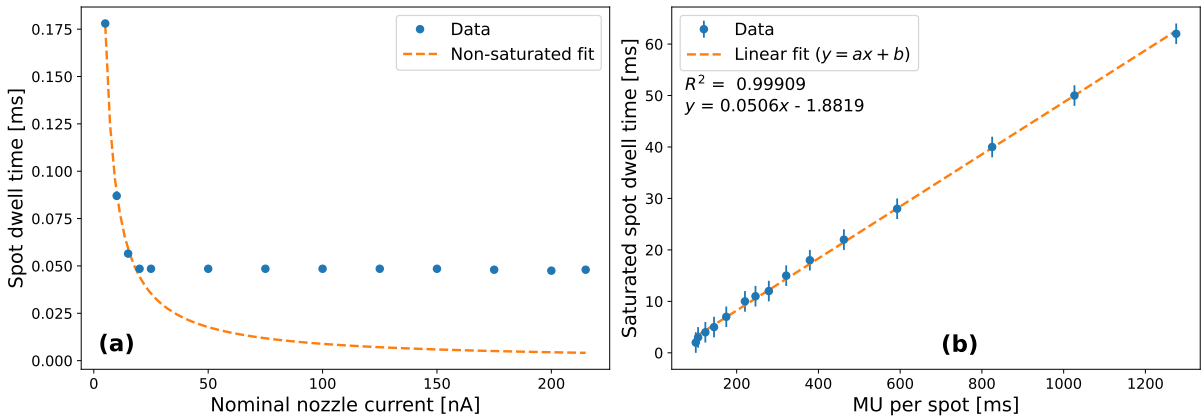

Figure 3.14: (a) The spot dwell time per MU as a function of the nominal nozzle current, measured by the FlashQ detector. The dashed curve represents the inverse-proportional relationship between spot dwell time and nozzle beam current in the absence of saturation. (b) The saturated spot dwell times plotted as a function of the the MU per spot. A linear fit is performed to investigate the linearity.

3.4.2 Scanning speed

The determination of the scanning speed consists of two parts. First, the ratio between the scanning speeds in the x- and y-direction is determined by analysing the smearing intensities between different spots using the Lynx detector. Figure 3.15 shows the relative dose distribution for a continuous scanning proton beam across a square-like 2 x 2 spot pattern with a spot spacing of 100 mm, alongside the summed intensity profiles in both directions. The four red peaks in the distribution correspond to the planned spot positions. However, their profiles deviate from the spot shape dose distributions displayed in Figure 3.1. This difference is due to the saturation of the Lynx, which results in a substantial area reaching maximum intensity. The intermediary intensity, which is observed between the spots and also termed smearing, is indicative of the beam's continuous movement during scanning. The average measured smearing intensity of 23.7 in the x-direction and 6.03 in the

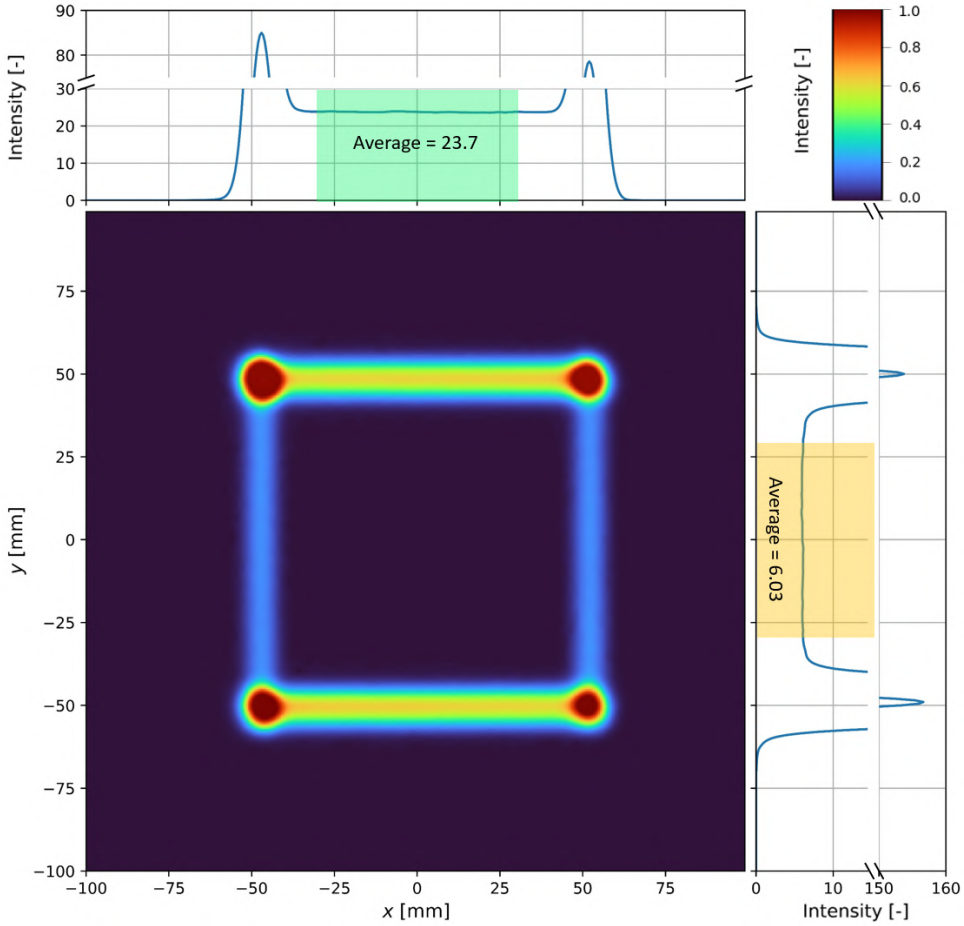

Figure 3.15: The relative dose distribution of a square-like 2 x 2 spot pattern with a spot spacing of 100 mm. The intensity profiles for the x- and y-axes are derived by summing the pixel values across each row and column, respectively, and are displayed next to the corresponding axis. The coloured areas on the graph represent the regions over which the average value is calculated for each direction. The measurement is performed using the Lynx at a nozzle current of 215 nA, under the correct gantry parameters, as detailed in subsection 3.4.6

y-direction yields an intensity ratio of 3.94 ± 0.05. Since smearing intensity indirectly measures the scanning speed, this ratio reflects the relative scanning speed in the x- and y-direction. With an expected ratio of 4, the found intensity ratio confirms the accuracy of the measurements.

Secondly, the scanning speed is determined by analysing intermediate events between irradiations. Measurements with 2 x 2 spot lists are conducted with not only smaller spot spacings (less than 10 mm) but also larger spacings (greater than 20 mm). These larger spacings correspond to the minimum distance required for capturing two consecutive intermediate events in the y-direction, given the FlashQ's 1 ms time resolution and an expected scanning speed of 20 m/s in the y-direction. Figure 3.16 shows the spatiotemporal reconstruction of an irradiation using the largest spot spacing of 100 mm. The intermediate events displayed between spots are indicative of continuous scanning of the beam. Alongside Figure 3.15, this further substantiates the correct working of continuous scanning operation mode. Additionally, the increased spacing between neighbouring events during transitions in the y-direction aligns with the higher scanning speed in that direction.

Figure 3.17 shows the scanning speed in the $x-$ and y-direction as a function of the spot spacing. For each spot spacing, the depicted data point represents the average scanning speed derived from multiple irradiations. The scanning speed for a single irradiation is determined by calculating the average distance between all successive intermediate events. The criteria for classifying an event as intermediate are detailed in subsection 2.6.2. Similar to the spot position calculation, a geometric correction is applied to the data to correct for any distal misalignment with the isocentre. No significant correlation has been observed between the scanning speed and the nominal nozzle current, hence the data from different currents are averaged. However, the results indicate that both scanning speeds vary with spot spacing. In the x-direction, the speed increases with

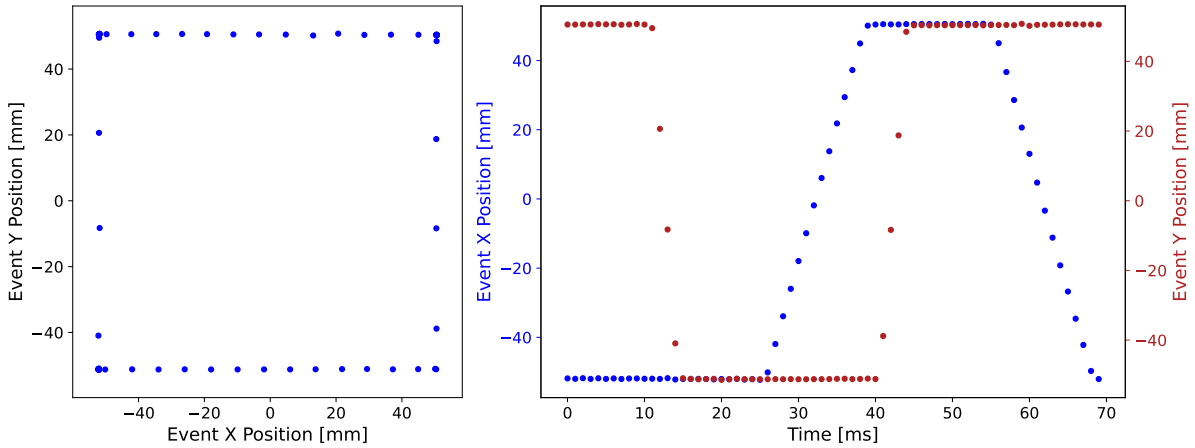

Figure 3.16: The full spatiotemporal reconstruction of a single irradiation in raster mode, measured with the FlashQ. Left: a scatter view of the retrieved per-event (x_0, y_0) coordinates. Right: the per-event x- and y-coordinates as a function of time. The irradiation comprises a uniform 2 x 2 square-like spot list with 100 mm spot spacing, conducted at a nominal nozzle current of 215 nA.

larger spacings before converging to an approximate steady value of 7.8 ± 0.1 m/s, derived from the average and standard deviation of the last four data points. Similarly, in the y-direction, the average scanning speed is calculated to be 29.4 ± 0.9 m/s. This results in a scanning speed ratio of 3.8 ± 0.1, which is comparable to the earlier found intensity-based value of 3.94 ± 0.05.

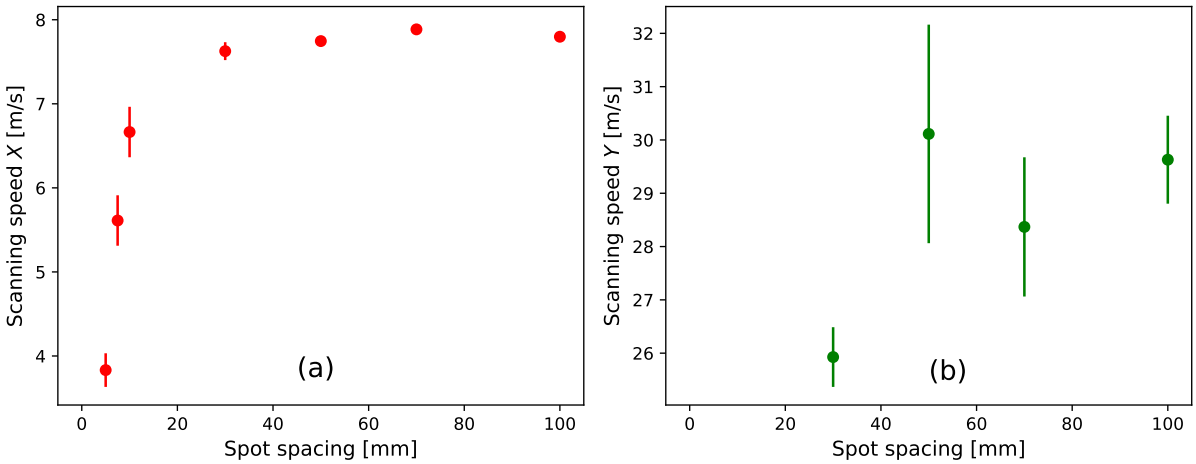

Figure 3.17: Scanning speed in the (a) x- and (b) y-direction as a function of spot spacing. Each data point represents the average scanning speed derived from multiple irradiations for a given spot spacing. The scanning speed for each irradiation is calculated by averaging the distances between all successive intermediate events.

3.4.3 Dose rate

Figure 3.18a shows the instantaneous dose rate as a function of the nominal nozzle current. The plotted data points represent the average IDR calculated from four different dose levels for each specific nominal nozzle current, with error bars indicating the uncertainty in the mean. A linear least-squares fit is applied to confirm the linearity of the IDR across the entire nozzle currents range, regardless of NMC saturation. With an R^2-value exceeding 0.99, the fit shows that the IDR maintains a linear relationship with the full nominal nozzle current range. From this analysis, a gradient of 4.46 Gy s^{-1} nA^{-1} is found. As anticipated, in the non-saturating regime, to ensure consistent dose delivery per MU, the nozzle current and delivery time are inversely proportional: doubling the nozzle current results in halving the spot dwell time. Consequently, this relationship leads to a doubling of the IDR since the total dose per MU remains constant. A similar pattern is observed in the saturated range of the NMC. As the spot dwell time remains constant, doubling the nozzle current doubles the delivered dose, thus doubling the IDR. The least-squares analysis reveals that the FLASH threshold for the instantaneous

dose rate occurs at a nominal nozzle current of 9.0 nA. After accounting for deviations between the nominal and detected nozzle currents, shown in Figure A.4a, the corrected threshold for the detected nozzle current is established at 7.0 nA. Note that the IDR is not uniform across the entire beam. For an individual UHDR proton beam, the highest dose rate occurs in the plateau region of the depth dose, not at the Bragg peak itself [104]. This variation is due to lateral divergence and scattering from the central beam axis, which causes the spot to broaden with increasing depth, consequently lowering the instantaneous dose rate.

Figure 3.18b shows the field-averaged dose rate as a function of the nominal nozzle current. Consistent with the IDR, the FADR exhibits a linear increase with the nominal nozzle current, demonstrating a gradient of 0.121 Gy s^{-1} nA^{-1}. This linear trend is anticipated since the field size and spot spacing remain constant across all irradiations, making the nominal nozzle current the sole variable of interest, thus mirroring the linear behaviour observed in the IDR.

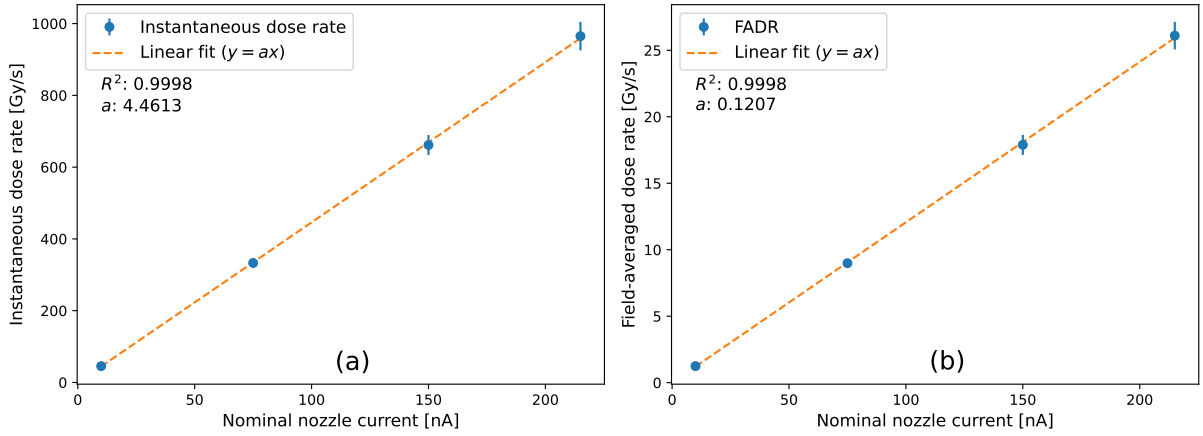

Figure 3.18: The (a) instantaneous dose rate and (b) field-averaged dose rate as a function of nominal nozzle current, with a linear fit included. The plotted data points represent the average dose rates calculated from four different dose levels for each specific nominal nozzle current, with error bars indicating the uncertainty in the mean.

3.4.4 Dose rate constancy

Figure 3.19a shows a box plot that illustrates the irradiation data plotted against the nominal nozzle current deviation, sorted by measurement session. Each black dot on the plot represents the nominal nozzle current deviation from a single irradiation, calculated using Equation 2.7. The data encompasses nozzle current values from 120 irradiations, collected over six different measurement sessions within a four-month period. Figure 3.19b shows the distributions formed by these individual irradiation points, each plotted per measurement session and visually distinguished using different colours.

First, the day-to-day variance is assessed by examining the data distributions per measurement session. It is observed that these distributions do not visually overlap in terms of both the standard deviation and the mean, suggesting the absence of a higher common distribution and confirming the presence of day-to-day variance. To further substantiate this observation, a statistical evaluation is conducted using ANOVA, Alexander-Govern, and Kruskal-Wallis tests. The results from all three tests yield p-values that are several orders of magnitude smaller than 0.05 ($\approx 10^{-8}$), which is the significance level set for the null hypothesis that all distributions originate from the same broader distribution. Therefore, the data are interpreted as distinct distributions, and the findings indicate a clear day-to-day variance. Among the six measurement sessions analysed, the nominal nozzle current deviations ranged from a minimum of -13.9% to a maximum of -23.2%. Additionally, no significant evidence was found to refute the normality of the individual histograms.

The second part of this analysis examines the beam-to-beam variance analysed through the nominal nozzle current deviations observed during the measurement sessions. This investigation reveals that the standard deviations vary between 2.2% and 6.0%, with an average of 3.9%, characterising the beam-to-beam variance. Additionally, no apparent correlation is found between the magnitude of the deviations and the nominal nozzle current of each individual irradiation.

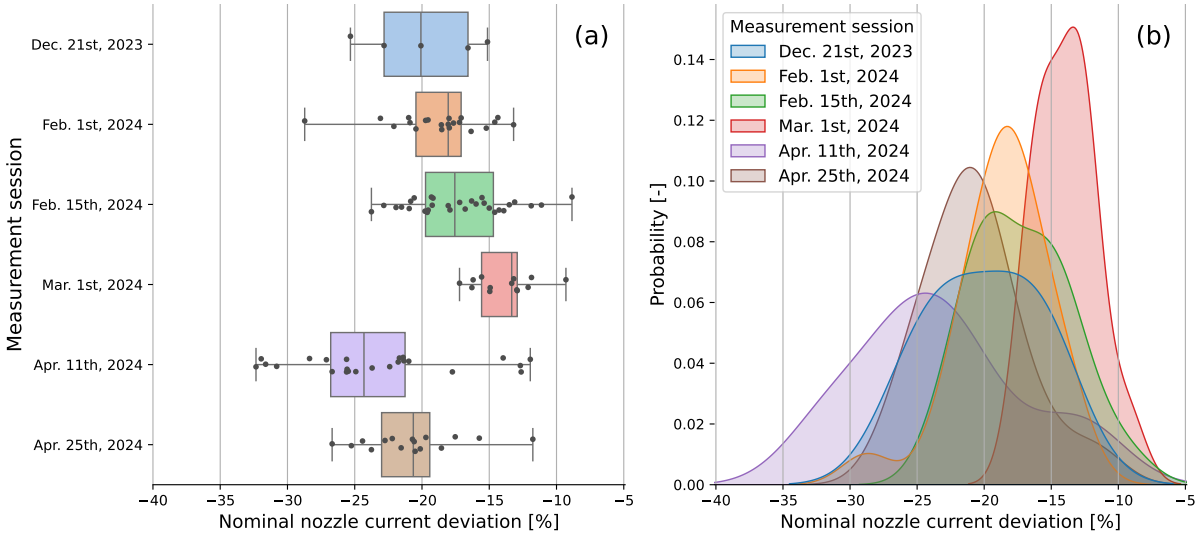

Figure 3.19: The nominal nozzle current deviation (Eq. 2.7) across sjix measurement sessions. (a) A box plot showing the distribution of nominal nozzle current deviation for each measurement session. The central line in each box indicates the median, while the dots represent individual irradiation deviations. (b) Probability density estimations showing the distribution of the nominal nozzle current deviations for each session, coloured by date, illustrating the variance in distribution shapes across the measurement period.

Finally, the variation within the beam is assessed by analysing the variance in the instantaneous dose rate as a function of time during each irradiation. The average relative variance observed across all included irradiations is 1.9% of the magnitude of the detected nozzle current, with the median variance found lower at 1.5%, attributed to three outliers with a relative variance exceeding 5%. Similarly, no immediate correlation is found between the relative variance and other irradiation parameters such as nozzle current, irradiation time, and field size.

3.4.5 Coupling FlashQ and Faraday cup

As explained in subsections 2.1.1 and 2.6.5, due to saturation effects in the NMC, the FlashQ is used as the reference monitor chamber. This approach enables the retrospective assessment of beam intensity, including the actual nozzle current, over time through calibration with a Faraday cup. Figure 3.20 displays the calibration curves for both FlashQ devices, where FlashQ counts per second are plotted against the FC current, which is found suitable for reliable current measurements at ultra-high dose rates. The FlashQ counts are determined by dividing the total detected counts by the irradiation time (also recorded by the FlashQ). With R^2-values exceeding 0.99, the linear least-squares fit confirms the strong linearity of the FlashQ counts per second with the nominal nozzle current. The established calibration factors are $(2.91 \pm 0.04) \cdot 10^4$ for the original FlashQ and $(2.22 \pm 0.03) \cdot 10^4$ for the loan Flash. As no saturation effects have been observed, the FlashQ is deemed a suitable detector to be used as a reference monitor chamber.

Although the calibration factors are precise, the inherent limitations of the least-squares fit mean that not all data points are perfectly aligned, leading to potential errors when using the FlashQ for calibration. Assuming the FC provides accurate benchmarks and considering that both the FlashQ and FC measured the same intensity, the FlashQ data derived from the calibration curve can be directly compared to the FC readings. This comparison shows a wider distribution for FlashQ data. When converting values between FlashQ and FC, the standard deviation as a percentage of the reading is 2.3%, with a 99% confidence interval of 6.0%. This variability is depicted in Figure A.5, which shows the difference in reading between both detectors. Lastly, as the accuracy of FlashQ counts per second hinges on both count and time readings, the precision of time measurement is also investigated. The loan FlashQ measurements are conducted on the experimental beamline at HollandPTC, where precise irradiation times can be specifically requested for measurements. The total irradiation time recorded by the FlashQ is compared against these requested beam line irradiation times, yielding highly accurate results. These findings are almost always found to match the beam line's timing perfectly with an uncertainty of 1 ms, corresponding to the time resolution of the FlashQ.

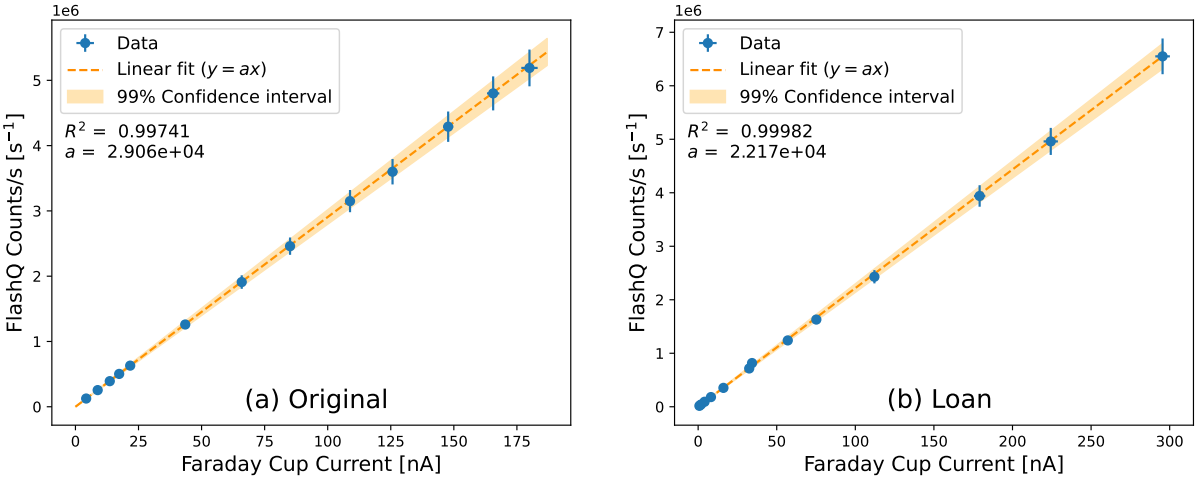

Figure 3.20: The (a) original and (b) loan FlashQ counts per second plotted against the nozzle current measured with the Faraday cup. A linear fit is overlaid to determine the calibration factor. The least-squares fit includes both the uncertainty in the FlashQ counts (u(counts) = 5% of reading) and time (u(T) = 1 ms).

3.4.6 Continuous scanning parameters ProBeam

The first parameter investigated is I_{mag}*-tolerance*. It is observed that the gantry halts the irradiation process if the current discrepancy exceeds the tolerance value of either 1200 or 1600 nA, as illustrated in Figure 3.21a, where the first spot is successfully irradiated but the gantry stops after a brief dose deposition resulting in a low-intensity spot. To address this, the tolerance limit needs to be increased to allow for spot spacings larger than 13 mm. In the conducted measurements, this limit was raised from 1200 to 12,000,000 mA (12 million) in the x-direction and from 1600 to 16,000,000 mA in the y-direction, enabling the beam to complete the full irradiation cycle regardless of spot distance, as shown in Figure 3.21b.

The second parameter is *ConstRaster*. For sufficiently large spot spacings and despite the default gantry setting, the gantry does not always manage to fully stop the beam throughout the entire transition, leading to some degree of beam smearing. This is illustrated in Figure 3.22a, particularly visible in the x-direction, where the beam stops temporarily but then continues. This phenomenon is not observed in the y-direction due to the faster scanning speed at similar distances. To address this issue, both parameters have been increased from 10 mm to 100 mm, allowing the gantry to maintain continuous spot transitions, as shown in Figure 3.22b.

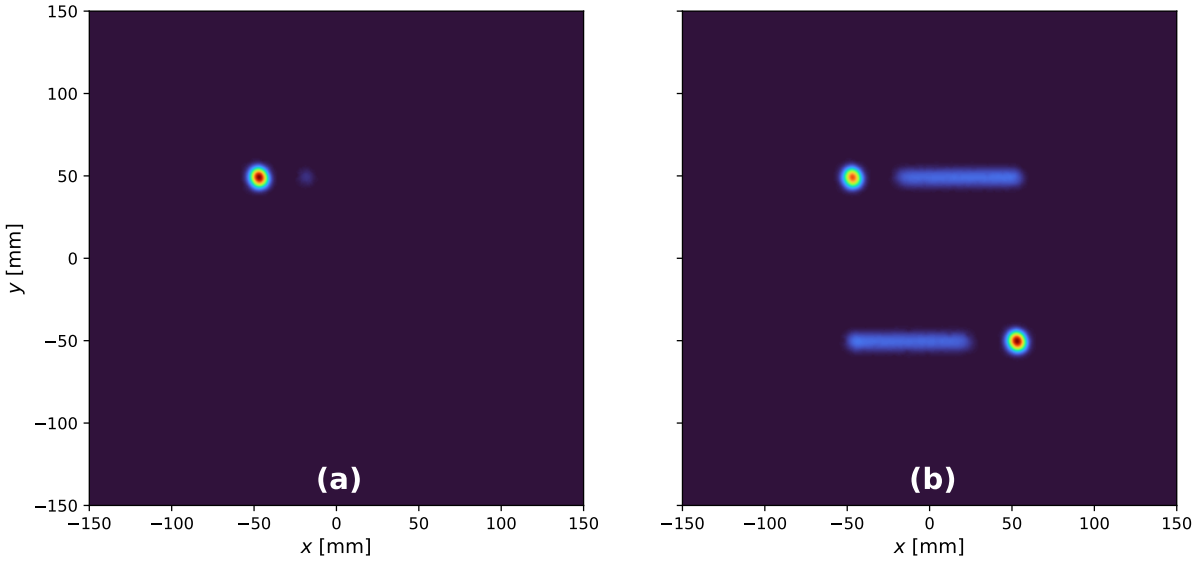

Figure 3.21: Irradiation of a 2 x 2 spot list with a spot spacing of 100 mm. (a) uses I_{mag}*-tolerance* settings of 1200 mA in the x-direction and 1600 mA in the y-direction. (b) employs much higher settings of 12,000,000 mA in the x-direction and 16,000,000 mA in the y-direction. Measurements were conducted with the Lynx at a nominal nozzle current of 215 nA.

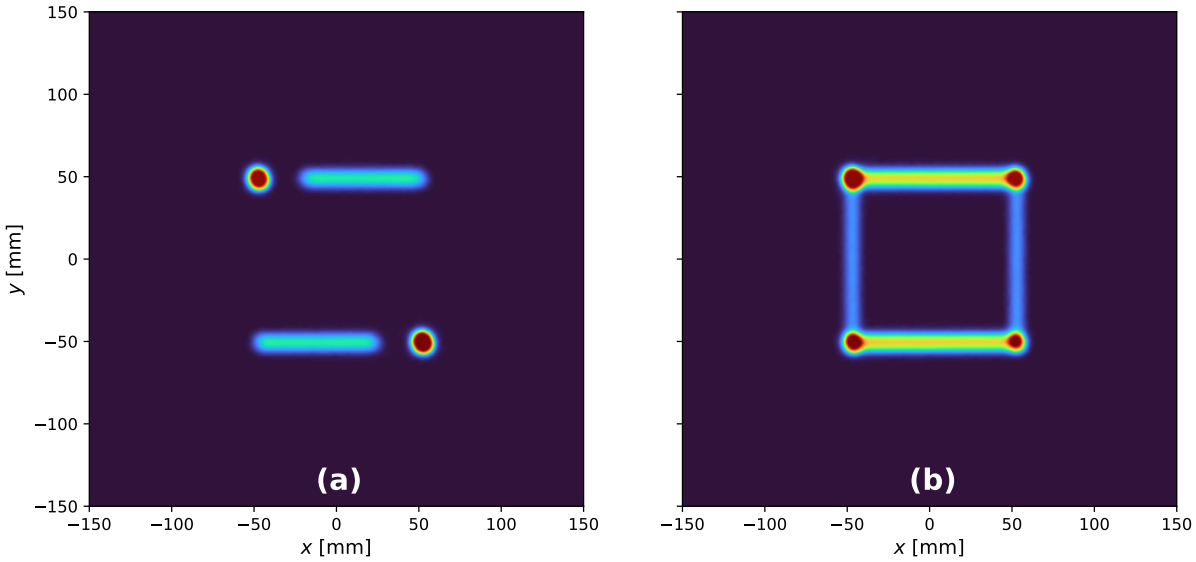

Figure 3.22: Irradiation of a 2 x 2 spot list with a spot spacing of 100 mm. (a) uses *ConstRaster* settings of 10 mm in both the x-direction and y-direction, where the beam is stopped temporarily for spacings exceeding this value, resulting in non-continuous scanning. Panel (b) employs increased settings of 100 mm in both directions, allowing for continuous scanning without temporary beam stops. Measurements were conducted with the Lynx at a nominal nozzle current of 215 nA.

4

Discussion

As part of the commissioning process of the proton FLASH beam at HollandPTC, this work describes the characterisation of the gantry-based 250 MeV UHDR continuous scanning proton beam. In this chapter, the findings from the four distinct dosimetric aspects that have been examined are discussed, followed by final remarks about the reproducibility and QA process in the fifth and final section.

4.1 Lateral relative dosimetry

4.1.1 Spot shape

First, the spot shape, as depicted in Figure 3.1, is modelled using a two-dimensional elliptical Gaussian. The parameters are observed to be of the same order of magnitude as those reported by other ProBeam institutions [97, 104, 106]. The 2D fit demonstrated an average discrepancy of 3.3% and a maximum of 3.7% between the fitted spot shape and the measured relative dose distribution of the spot. Furthermore, across different nozzle currents, the observed differences between repeated measurements of σ_x and σ_y are less than 2%. This variance is considered clinically insignificant by AAPM TG-224 standards, which allow for a delivery tolerance of ±10% for the spot shape [90]. This standard is supported by previous research which investigated the dosimetric consequences of pencil beam width variations, demonstrating that a 10% deviation in spot size has a minimal impact on target coverage [140–142]. Based on these findings, a fixed spot shape was maintained across all analyses in this report, irrespective of the nominal nozzle current for each irradiation. These are $\sigma_x = 3.39 \pm 0.06$ mm, $\sigma_y = 3.86 \pm 0.02$ mm and θ = -16.6 ± 4.5 degrees. This approach significantly simplifies modelling the UHDR proton beam both in current and future research.

Moreover, similar to this study, numerous articles have reported the measured spot profile solely in the form of a single Gaussian distribution [97, 104–106]. This is deemed accurate for in-air measurements as Li et al. found that single Gaussians provide a sufficiently accurate spot shape for these measurements [143]. To investigate the intrinsic spot shape of the gantry, air is chosen as the medium because water introduces additional scatter contributions to the dose profile. Nonetheless, both modelling with a single Gaussian and performing measurements in air do not fully capture long-range scatter effects due to nuclear interactions and large-angle Coulomb scattering. However, these factors were omitted to simplify numerical models. Ultimately, further modelling of these contributions is recommended, as they become more significant in measurements performed at greater depths in water, which are more clinically relevant too. To address this, some studies have included Cauchy-Lorentz distribution factors [105, 143]. Despite these individual factors having a minor impact on the overall dose — contributing 0.1-1% relative to the peak dose — their influence on the extended dose profile is clinically significant. Given that a proton field involves thousands of spots, these minor contributions cumulatively affect dose delivery accuracy, particularly since these tails can extend up to 10 cm from the centre of a spot [105]. As mentioned, this is specifically prevalent at medium depths where a scanning spot's peak dose may not dominate due to additional scatter contributions [143].

4.1.2 Spot position

Secondly, the accuracy of the spot position was evaluated to be 0.06 mm, meaning that the likelihood of a spatial difference between the detected spot position and the corresponding planned coordinate exceeding 0.15

mm (99% confidence interval) is approximately 1%. The detected spot positions were determined by least-squares fitting the spot centre coordinates (x_0, y_0) for each time step measured by the FlashQ, referred to as an event, and averaging the positions of the events that corresponded to a specific planned spot position. However, since the FlashQ reading consists only of integral readings of both directions, performing a 2D fit was found to be impossible without fixing either the spot shape or the spot angle. In this work, the spot angle was held constant as its clinical relevance was deemed less critical.

Sporadic jumps were observed in both the spatial and integral readings from the original FlashQ, significantly hindering the fitting algorithm, particularly at higher nozzle currents where the readings were on the same order of magnitude as the jumps. Initially, this led to less accurate retrieval of spot positions for each individual event. However, after manual data filtering performed by the vendor, the fitting algorithm functioned correctly. Ultimately, the jumps were determined not to be inherent to the proton beam but rather artefacts in both the spatial and integral strips of the FlashQ. This conclusion was supported by the observation of periodic negative counts with identical magnitudes. Conversely, measurements conducted with a loaned FlashQ did not exhibit any anomalies, as shown in Figure 3.2, leading to similar accuracy in retrieved data as the filtered results from the original FlashQ. Regardless, to ensure reliability, median values were chosen over means for calculating the detected spot positions. This approach helped mitigate biases that arose from consistent outlier positioning due to the aforementioned jumps. Choosing the median over the mean is deemed acceptable as a sufficient amount of data was available for each planned position.

Furthermore, it should be noted that scintillation screens are typically used for spot position measurements due to their high spatiotemporal resolution [144–146]. Although AAPM TG-224 does acknowledge the potential for using strip ionisation chambers for these measurements, Spruijt et al. specifically recommend the use of scintillation-based devices [90, 91]. However, in this study, differentiating between individual spots using the Lynx detector — a scintillation screen — proved challenging. Despite adjustments made to the gantry settings to prevent smearing between spots during the continuous scanning of the proton beam, smearing was still observed at spot spacings larger than 15 to 20 mm. To effectively distinguish between spots, it was assumed that the separation between the centres of the spots needed to be at least six times the spot width and height. With a minimum spot width of 3.4 mm, this did not allow for sufficient distance between individual spots. Hence, the FlashQ was used as its temporal resolution enabled the filtering of smeared data, thereby enhancing the precision of spot differentiation. Consequently, it is anticipated that the FlashQ can achieve results comparable to those of the Lynx. Still, it is important to note that the FlashQ has an effective resolution of 1 mm, whereas the Lynx offers a finer resolution of 0.5 mm. Hence, the spot position accuracy, with a 99% confidence interval of 0.15 mm, is significantly smaller than the resolution of the FlashQ. Therefore, this could simply be the intrinsic limit from the FlashQ's effective resolution. Nevertheless, this value is similar to another strip ionisation chamber with a position accuracy of 0.12 ± 0.02 mm and overall, well within the tolerance limit recommended by the AAPM TG-224 report, which specifies 1 mm for the absolute position accuracy [90, 105]. In line with these findings, it is concluded that a strip ionisation chamber is also deemed suitable for determining the spot position accuracy in FLASH measurements.

4.1.3 Beam envelope

Third, the beam envelope is shown in Figure 3.6, with linear fits detailed in Equation 3.1. The fits define the spot width σ_x and height σ_y as a function of the depth z in air and are based on current-averaged data points, aligning with the conclusion from subsection 4.1.1 that no significant nozzle current dependency is found. In the fit, the two fitted b-values represent the current-averaged spot width and height at the ISOC ($z = 0$). The gradient values a from these fits provide insight into changes in spot shape with depth in the air. The results show similar, yet distinct, gradients. For comparison, beam envelope data from a 250 MeV gantry at another ProBeam institute recorded gradient values of -0.006 and -0.012 for the x- and y-directions, respectively [106]. This variation underscores that beam envelope characteristics can differ significantly between institutions due to the intrinsic emittance of the beam, shaped by the beam-focusing elements unique to each facility's beamline. Accurately determining this attribute is crucial for correctly modelling dose delivery in patients. Typically, this is achieved by incorporating the beam line-specific equations, including the beam envelope, into the treatment planning system.

4.1.4 Comparison Lynx and EBT3 film

Fourth and last, the comparative analysis between film dosimetry and the Lynx system revealed similar, yet slightly varied, spot shape parameters. These differences are partly attributed to the intrinsic limitations associated with film development. The development and analysis process of the film involved several steps, each introducing small uncertainties. For instance, dust particles on the film were interpreted as significant saturated areas, potentially leading to minor errors. Additionally, there is an inherent uncertainty in determining the optical density and comparing it with the calibration curve. While each step contributed negligible uncertainty individually, collectively, they led to more significant errors. Another reason for this discrepancy could be due to an increased non-linearity in the Lynx's response for FLASH measurements, deviating from the ± 1.5% linearity specified in the manufacturer's specifications. Ultimately, as noted in subsection 4.1.1, the AAPM TG-224 guidelines permit a delivery tolerance of ± 10% for spot shape [90]. This tolerance supports the conclusion that the Lynx detector can be accurately used in UHDR measurements.

Moreover, the total MU per irradiation was adjusted to ensure each irradiation received an equal dose, as described in subsection 2.3.4. However, a retrospective comparison of the delivered dose, using the output measurements from subsection 3.3.1, revealed that the doses per spot varied across different nozzle currents, with the lowest being 4.9 Gy and the highest nearly doubling at 9.3 Gy. The shallow slopes of the EBT3 response curves at higher doses can lead to increased dose uncertainty [112], which might account for some observed measurement discrepancies under these conditions. Nonetheless, all doses remained below the 10 Gy threshold, thereby reducing concerns about potential inaccuracies due to overresponse behaviours [128, 129].

4.2 Longitudinal relative dosimetry

4.2.1 IDD

The in-depth beam range has been confirmed with an R_{80}-value of 37.9 ± 0.1 cm, aligning with theoretical expectations and demonstrating stability across multiple irradiations on the same day. This result is consistent with the findings from Charyyev et al., who reported a comparable R_{80}-value of 37.69 cm for their ProBeam system operating at 250 MeV [106]. The slight difference observed could be attributed to uncertainties, such as differences in experimental setup, as well as institutional beam line variations. In support of this, a study conducted by Langner et al. compared commissioning data of the ProBeam PBS proton beam across different energies up to 240 MeV at two different ProBeam facilities, finding that the consistency of IDD ranges in water was maintained within a precision of 0.5 mm [147]. The discrepancy between the results from Charyyev et al. and this study, coupled with the inherent uncertainties, is considered to be within an acceptable range. Furthermore, since the proton beam range is directly correlated with proton beam energy, beam energy was also investigated. Within HollandPTC, findings from the same cyclotron by Rovituso et al. highlighted a discrepancy between the nominal and detected beam energy of 1.0% [97]. It is important to note that these measurements were conducted on the research beamline, not the gantry beamline. Despite this, the detection of an energy of 248.5 MeV, representing a discrepancy of 0.6%, is not considered a significant outlier. Therefore, the R_{80}-value is deemed reasonable and typical for a 250 MeV gantry-based beam line.

In addition to the retrieval of the proton beam energy and range, the energy spread $\sigma_{E,0}$ was determined using the Bortfeld function. This determination involved a least-squares fit of Equation A.3.2, showing good agreement with the measured data but tending to overestimate both in the initial regime and at the Bragg peak. This discrepancy mainly arose because the Bortfeld fit only considers Coulomb interactions and omits the nuclear buildup effect in the entrance region, resulting in an elevated start and a slight overestimation at the peak. Importantly, the Bortfeld function is officially deemed valid only for proton energies ranging from 100 to 200 MeV, suggesting that the results may be skewed for energies outside this range. Furthermore, the energy purity, determined at 14.8 ± 0.8 MeV and corresponding to a relative purity of 5.9% compared to the initial energy, contrasts with the expectation set by Bortfeld, which suggests the width of the Gaussian energy spectrum should be around 1% of the initial proton beam energy, as shown in Table A.3. Therefore, alternative methods for defining the energy spectrum should be considered. For instance, multiple reports recommend using Monte Carlo simulation software, such as TOPAS and Geant4, to calculate the FWHM/E_0 ratio (where FWHM is the full width at half maximum and E_0 is the nominal proton energy) to define the energy spectrum [100, 148]. Considering that energy dispersion significantly influences the shape of pristine Bragg peaks, and given that similar in-house calculations have already been conducted at HollandPTC's eye beamline [98], follow-up research should extend these efforts to the gantry-based 250 MeV beamline to verify the energy spread.

Lastly, the IDD measurements were conducted at a nominal nozzle current of 2 nA, with the corresponding R_{80}-values considered accurate. This accuracy is maintained as saturation issues contribute only a negligible 0.025% discrepancy, attributed to the saturation of the monitor chamber positioned in between the gantry's nozzle and water phantom. Although the nominal nozzle current used is below the 9.0 nA FLASH threshold, increasing it is not recommended due to the introduction of additional unwanted saturation effects. Furthermore, studies like those by Darafsheh et al. on different systems and Langner et al. on a ProBeam system have demonstrated stability in the IDD across various dose rates [133, 147]. Langner et al., in particular, showed no dose rate dependence, even with a 50-fold increase in dose rate. These findings suggest that the underlying physics is unlikely to vary significantly in clinical settings as the nozzle current or dose rate increases.

4.2.2 Saturation effects BPC and MC

To assess the usability of both the Bragg peak and the Monitor chamber in FLASH measurements, the saturation effects of each chamber were investigated. It was determined that the BPC did not exhibit any significant changes in ion recombination as the nominal nozzle current increased. Conversely, the MC experienced ion recombination effects, with the discrepancy between the readings from the two chambers exceeding 0.5% at a nominal nozzle current of 23 nA. This current corresponds to an instantaneous dose rate of approximately 100 Gy/s. This performance is notably superior compared to the specifications provided by the vendor, which indicate a maximum dose rate of 10 Gy/s for achieving greater than 99.5% saturation at nominal voltage [117]. The specified dose rate corresponds to a nominal nozzle current of 2.24 nA, reinforcing the accuracy of the IDD measurements conducted at 2 nA. Additionally, the maximum dose rate for similar ion collection efficiency in the BPC is 21 Gy/s [116]. Remarkably, the BPC showed no signs of saturation for nominal nozzle currents up to 215 nA, which is equivalent to nearly 1000 Gy/s. Besides a possibly lower saturation value reported by the vendor, no clear reasons have been found for this dose rate discrepancy.

4.3 Absolute dosimetry

The absolute dosimetry measurements were conducted using the Advanced Markus chamber within a water phantom at a depth of 2 cm WET. In this study, the output of the gantry is quantified by the peak dose delivered per monitor unit for a single spot. This measure was selected because it is independent of the field size, can be directly correlated to the nominal nozzle current and allows for modelling of the expected dose distribution. Comparisons of the results with those from other ProBeam institutes that measure in Gy mm^2 MU^{-1} for a single field [106, 147] are not performed, which is a limitation of this work and should be considered for future research activities.

Quantifying the dose in Gy/MU necessitates a simulation, introducing extra uncertainties, two of which are particularly relevant to this research. Firstly, it is assumed that the Advanced Markus chamber is perfectly aligned with the central beam axis. However, significant effects from potential misalignment are not expected. This is because the small detector, when used within a relatively large field, is fully placed within the uniform field, effectively mitigating any partial volume effects. Secondly, the simulation incorporates the beam envelope relationships from Eq. 3.1 to model the spot shape, which influences the dose distribution. Notably, the output measurements are performed in liquid water, whereas the beam envelope data are obtained in air. As discussed in subsection 4.1.1, additional scattering in water impacts dose accuracy due to the more prominent influence of neighbouring spots. This effect results from alterations in spot shape, mostly due to Cauchy-Lorentz distribution factors and large-angle Coulomb scattering. These factors are not included in this research and thus are not considered in the simulation, leading to discrepancies in the peak dose reading D_{peak} and consequently, the field-to-peak ratio. Building on the conclusion from subsection 4.1.1, the spot shape in water should be investigated either through direct measurements or Monte Carlo simulations. The findings from these investigations can then be incorporated into the output simulations to enhance the accuracy of the field-to-peak ratio

4.4 Temporal dosimetry

4.4.1 Spot dwell time

As outlined in subsection 2.1.1, the dose delivery behaviour of the gantry exhibits distinct characteristics in non-saturated and saturated states of the nozzle monitor chamber, which are mathematically represented by Eq. 2.1 to 2.4. It has been observed that the spot dwell time converges to a constant value of 0.0483 ms per MU

once the nominal nozzle current surpasses the found threshold of 18.4 nA, indicating saturation of the NMC. This phenomenon is consistent with findings by Yang et al. from the commissioning of the 250 MeV research proton beamline at the New York Proton Center, another ProBeam facility involved in FLASH treatment [108]. Similarly, their research identified two distinct regimes — non-saturated and saturated NMC ranges — with comparable behaviours and characteristics. Yang et al. reported a convergence value for t_{dwell} at 0.0481 ms, which aligns within 0.5% of the value found in this work. However, despite providing a broad nominal nozzle current range from 10 to 30 nA, they did not specify an exact threshold value for the NMC to start saturating, although the value identified in this thesis does correspond with their reported range. Charyyev et al. do report that output was found to be stable up to a beam current of 15 nA, which aligns with the detected nominal nozzle current threshold of 15.7 nA identified in this study [106]. However, it is unclear whether Charyyev et al. refer to nominal or detected nozzle currents in their report.

Furthermore, the constant t_{dwell}-value found in this research corresponds to a delivery rate of 20,704 MU/s in the saturated state. These findings are consistent with previous measurements within HollandPTC, which recorded a rate of 20,380 MU/s, showing a close agreement within 2%. This discrepancy of 2% is deemed acceptable as it falls within the intrinsic measurement uncertainty. However, the amount of MU/s could deviate on a day-to-day basis due to manual settings by Varian. They require manual adjustment of voltage meters in the gantry nozzle, potentially resulting in variations between different measurement sessions. Ultimately, the definition of a fixed spot dwell time (and MU/s) results from the saturated NMC and should become obsolete as the spot dwell time becomes variable across the entire nozzle current range for a non-saturated NMC, a topic that will be further discussed in Section 4.5.

4.4.2 Scanning speed

The scanning speed of the ProBeam system has been quantified through two different methods. Initially, the ratio of the scanning speed was determined by comparing the smearing intensity between two spots in both the x- and y-directions, to establish the relative difference in scanning speeds between these two directions. An intensity ratio of 3.94 ± 0.05 was established, which is considered accurate when compared to the vendor-specified ratio of 4, with expected scanning speeds of 5 m/s in the x-direction and 20 m/s in the y-direction respectively. This value is calculated by averaging the intensity values within a manually defined range where the dose contributions from the planned spot are assumed to be zero, attributing any detected intensity to pure smearing. The method does not differentiate between directions within the same dimension, such as left to right versus right to left in the x-direction; however, no significant differences were observed in this aspect. Additionally, calculations showed that using the sum of intensities, instead of the average, did not yield any substantive differences in the outcomes.

Secondly, the magnitude of the scanning speed in both the x- and y-directions is quantified through the analysis of intermediate events, which are beam spots registered while the beam transitions from one spot to another. This approach is elaborated in subsection 2.6.2. Measurements are performed using the FlashQ detector, a strip ionisation chamber with a time resolution of 1 ms. For each time step, the central spot coordinate is determined through a Gaussian least-squares fit. However, accurately locating the position of intermediate spots presents challenges due to the movement of the beam during a single time step, causing the FlashQ reading to smear/flatten and deviate from Gaussian profiles like Figure 3.2. The least-squares fit minimisation process was observed to align the Gaussian profile, particularly the optimal central coordinates x_0 and y_0, with the centre of the smeared reading, even though the width of the Gaussian did not match the spread of the reading. While, in theory, this should not pose significant issues as long as the fitting algorithm applies it consistently, this method still introduces additional uncertainties. This is particularly true if the reading for a single time step is asymmetrical or involves small spot spacings. Also, the issue is especially pronounced in the y-direction, where the scanning speed is four times greater than in the x-direction, amplifying the likelihood and impact of flattened and/or asymmetrical readings. Alternative methods for determining scanning speed that account for the flattening could be of interest. For instance, since the width of the FlashQ reading per time step is dependent on the speed at which the beam scans across the detector surface, calculating the FWHM and correlating it to the scanning speed could provide a direct measure of beam movement. Another option could involve using the Lynx detector, which, unlike the FlashQ, does not have a time resolution because it measures the full signal while the detector is active. This approach would use the continuous data captured by the Lynx to estimate the speed from the spread and intensity of the detected signal. Assuming that the beam moves in a single, consistent direction (only forward, without retracing steps) and that the spot shape remains constant, it might be possible to determine the scanning speed from a non-time-resolved 2D scintillation detector image (e.g. Figure 3.15) through a deconvolution of the smeared path with the known spot shape.

In this study, the scanning speeds were found to be correlated with the spot spacing but ultimately converged to 7.8 ± 0.1 m/s in the x-direction and 29.4 ± 0.9 m/s in the y-direction, values that exceed the vendor's specifications of 5 and 20 m/s in the x- and y-direction respectively. These observations could be attributed to several factors. First, it is observed that for spot spacings less than 20 mm, which are considered clinically significant, the scanning speed in the x-direction indeed approximates the expected 5 m/s. Therefore, while higher scanning speeds could theoretically lead to reduced irradiation times and increased local dose rates, in practice, this effect may be less apparent in clinical settings. Furthermore, the impact of scanning speed variations on dose rate was also found to be relatively minimal by Huang et al., where a 10% discrepancy in scanning speed resulted in only a 1% effect on the resultant dose rate for typical clinical plans [71]. Second, the dependency of the scanning speed on the spot spacing is potentially due to a slow-down effect observed as the beam nears the next spot. This phenomenon has been visually documented in the spatiotemporal reconstruction of a single irradiation by Yang et al., which shows a noticeable deceleration upon arrival at another spot [105]. Assuming the time spent slowing down remains constant irrespective of spot spacing, smaller spot spacings would exhibit a higher ratio of events affected by this slowing effect compared to normal intermediate events where the beam scanning is not impeded. The convergence of values for larger spot spacings then logically follows from the fact that the time slowing down becomes negligible relative to the regular scanning time. A similar dependency on the spot spacing was identified by Tsai et al., who reported that an increase in spot spacing within the same scanning direction led to higher scanning speeds before reaching the maximum scanning speed [149]. Unfortunately, while similar spatiotemporal reconstructions have been performed in this work (as shown in Figure 3.3, 3.4, and 3.16), the replication of the slow-down effect with the FlashQ was not feasible. The detector used by Yang et al. boasts a 50 µs resolution, which is twenty times more precise than the 1 ms resolution of the FlashQ. Hence, to investigate this phenomenon more in-depth, it is recommended to use a detector with significantly better temporal resolution.

Moreover, variations or discrepancies in speed measurements may be considered normal across different ProBeam systems. For example, Kanouta et al. report scanning speeds at ISOC of 10 ± 0.8 m/s in the x-direction and 25.5 ± 5.1 m/s in the y-direction at their ProBeam gantry at the Danish Centre for Particle Therapy [150]. These findings align reasonably well with another Varian ProBeam facility, where logfile analysis yielded speeds of 7 m/s and 32 m/s in the x- and y-directions respectively [151]. This indicates that discrepancies are likely due to intrinsic variations in system performance and potentially conservative estimates from the vendor, which tend to predict longer beam delivery times than those achieved in practice [75, 152].

Lastly, the scanning speed data points with corresponding error bars from Figure 3.17 are calculated based on the average and standard deviation of individual averages from the irradiations. However, the error or deviation of the distances within a single irradiation itself is not included, thereby potentially underestimating the total error. This omission is particularly critical for low spot spacings, where the number of intermediate events is limited and the distances between two neighbouring events per irradiation can vary significantly. This variation could lead to a larger standard deviation, affecting the accuracy of the calculated values.

4.4.3 Dose rate

In this study, both the instantaneous and field-averaged dose rates are examined, primarily because these measures are straightforward to calculate and are commonly reported in related research. The IDR in this research was found to be linearly dependent on the nominal and detected nozzle current with 4.46 and 5.68 Gy s^{-1} nA^{-1} respectively. A comparison with commissioning data from the New York Proton Center, reported by Yang et al., reveals a gradient of 4.06 Gy s^{-1} nA^{-1}, which is 9.1% lower than the gradient derived from the analysis conducted in this thesis [108]. It is important to note that Yang et al.'s value is calculated based on only two data points, and thus it should be considered with a significant margin for error. FADRs are also reported by both Charyyev et al. and Yang et al., with the former observing a similar linear relationship in their FADR calculations [106]. In this thesis, a FADR gradient of 0.121 Gy s^{-1} nA^{-1} is determined. Yang et al. reported a higher gradient of 0.156 Gy s^{-1} nA^{-1} indicating a nearly 30% discrepancy [108]. However, when adjusted for nozzle current deviations during measurements for this thesis, a gradient of 0.154 Gy s^{-1} nA^{-1} is determined, aligning within 2%.

Discussing the realisation of the FLASH effect, a nominal nozzle current threshold for the IDR to exceed 40 Gy/s was determined at 9.0 nA. Consequently, all single spot irradiations, such as spot shape and beam envelope assessments, in principle adhered to the main FLASH criterion. In contrast, according to the FADR calculations for a 5 x 5 cm^2, with a 5 mm spot spacing spot list, no FLASH effect was achieved even at the highest nominal nozzle current. Extending the least-squares fit from Figure 3.18b, the nominal nozzle current threshold for a FADR exceeding 40 Gy/s is calculated at 331.4 nA.

It should be noted that these metrics are not realistically applicable in a clinical setting. Determining whether or not the FLASH effect is achieved through the IDR is not realistic as treatment fields consist of hundreds or thousands of planned spot positions. Furthermore, while the FADR does provide insight into dose rates, it usually underestimates the local dose rate as compared to more accurate dose rate definitions like the PBS-DR by Folkerts et al., which takes into account the unique spatiotemporal delivery patterns of PBS FLASH radiotherapy [88]. Although the relationship between nominal nozzle current and dose rates is linear, this is not the case for other parameters like field size. Even in scenarios where the field is uniform, the distribution of spots alters the PBS-DR. The FlashQ system does offer the capability for more complex dose rate calculations due to its temporal resolution and the ability to correlate counts with delivered doses. This potential was not explored in this thesis, representing a limitation of the current work. For future research, it is recommended to perform a calibration similar to that of the SICA, a 2D strip-segmented ionisation chamber array akin to the FlashQ [105]. Here, measurements were conducted to determine the dose calibration factor that converts the reading from the SICA into the received dose. While the FlashQ in this study was calibrated against the FC, the calibration factor relative to the Advanced Markus reading — and thus the dose — has not yet been implemented. Implementing this would enable both spatial and dose reconstruction over time.

4.4.4 Dose rate constancy

Data collected with the FlashQ over six different measurement sessions within a four-month period revealed significant dose rate deviations, both between different measurement sessions (day-to-day variation) and within the same day (beam-to-beam variation). These variations can significantly influence output values and dose rates because the MIC is unable to adjust the spot dwell time to compensate for these fluctuations due to saturation. Consequently, these variations are directly reflected in the output of the gantry and could potentially negatively impact the desired FLASH effect.

Day-to-day variations are evident from the discrepancies observed between the nominal/requested nozzle current and the nozzle current detected by the FlashQ, which directly leads to deviations in the instantaneous dose rate. The average discrepancy between the nominal and detected nozzle current ranged from a minimum of -13.9% to a maximum of -23.2%, as depicted in Figure 3.19. While the magnitude of these deviations aligns with previously reported variations for the ProBeam cyclotron system at HollandPTC, only negative discrepancies were observed, and no clear cause has been identified. It could be possible that this has to do with the fact that the maximum possible achieved nozzle current in the gantry is 215 nA due to cyclotron limitations under UHDR conditions. As the maximum requested nominal nozzle current also equals 215 nA, it would be impossible to measure more than 215 nA due to physical limitations. In addition to intrinsic gantry variations, discrepancies may also be attributed to the measurement device, the FlashQ, which was calibrated using a Faraday cup. The suitability of the FC for UHDR measurements is well-established in literature [64, 65, 105, 114]. However, consistent negative discrepancies could potentially be explained by a systematic error in the calibration of the FlashQ devices, either due to incorrect device settings or errors in the analysis. However, this is considered unlikely, as the calibrations were performed on separate days and have been thoroughly verified.

Similarly, the New York Proton Center, another ProBeam facility, reported significant discrepancies between different measurement days with an output variance of 9.69% around their baseline value [105, 149]. These measurements were obtained through repeated measurements of a 5 x 5 cm^2 field with 5 mm spot spacing. Although the output variance value represents variations in absolute dose output measurements, the same study highlighted a strong correlation, with a ratio close to 1, between dose rate variations and absolute dose output, thus also quantifying the variation in dose rate across various measurement sessions. Moreover, despite the irradiated output field being identical to the one in this study, a direct comparison with the values found in this thesis is not feasible due to differences in definition and because no standard field size was irradiated in this work. Instead, dose rate constancy was determined through irradiation over various field sizes and nozzle currents, focusing solely on variations in IDR. However, as part of the FLASH quality assurance process, output measurements using a similar 5 x 5 cm^2 field are already being conducted at HollandPTC, which enables a direct comparison with the New York Proton Center in the near future.

Next to day-to-day variations, beam-to-beam variations are also evident, with an average IDR variance of 3.9% between irradiations on the same day. This variation is smaller than the day-to-day variations, which aligns with findings by Tsai et al., who not only noted the presence of beam-to-beam variations but also mentioned that fluctuations within the same day or experimental session were generally smaller compared to day-to-day fluctuations [149]. Similarly, Charyyev observed through reproducibility measurements that the dose and dose rate could vary by 6.4% and 4.2%, respectively, for repeated irradiations [106]. Hence, the presence

of both day-to-day and beam-to-beam fluctuations at the HollandPTC gantry not only underscores the challenges faced at this institute but also highlights that this is a common issue across various ProBeam facilities engaged in the irradiation of FLASH proton beams.

Lastly, a median variance of 1.5% was observed in the instantaneous dose rate within single irradiations. However, three outliers exhibited a relative variance exceeding 5%. No definitive reason could be identified, as initial analyses did not reveal any clear correlation between the magnitude of these deviations and other beam or field parameters. Contrary, Tsai et al. reported day-to-day and beam-to-beam variations of 0.47% and 2.39% respectively for a 5 nA nozzle beam current, while for higher beam intensities, such as a 215 nA nozzle current, fluctuations were significantly larger with day-to-day and beam-to-beam variations of 2.14% and 9.69% respectively — more than four times as large [149]. It must be noted that while these findings do not directly quantify variation within the beam, they indicate that further investigation is warranted. Additional research into fluctuations within the beam is also recommended, as some longer irradiations have displayed greater deviation within the beam than the average irradiation standard deviation of 1.5%, occasionally exhibiting a sinusoidal pattern over time within the same irradiation. Depending on the spatiotemporal aspect of the treatment plan, this could lead to significant local deviations in both dose and dose rate, which may require additional corrections or margins when creating future clinical treatment plans, as discussed in section 4.5.

4.5 Reproducibility & QA

This thesis has characterised four dosimetric categories of the UHDR proton transmission beam at HollandPTC, with corresponding characteristics measured across various days over a four-month period. However, most measurements were conducted on a single day. This means that although quality assessment for the same day is complete and comparisons with other institutes are feasible, the majority of the characteristics and their corresponding values have not been verified over time. Consequently, this section focuses on the reproducibility of the results and explores and summarises the extent to which follow-up research and an extensive quality assurance programme are necessary for certain characteristics.

First, characteristics are identified that do not necessitate extensive follow-up research and can be integrated into regular machine QA guidelines as described by Spruijt et al. and in the AAPM TG-224 report [90, 91]. This category includes the spot shape, beam envelope, IDD and spot dwell time. As discussed in corresponding sections, these values have been reported as averages of repeated measurements on the same day. For instance, the deviations measured in the spot shape both on the same day and when compared with another measurement session were deemed clinically insignificant. Unless there are physical changes or adjustments made to the settings of the gantry, it is not expected that the spot shape will undergo clinically significant changes over time. Moreover, deviations found in the repeated measurements of the IDD were minimal, and it is possible that deviations between values measured on separate days fall within the guidelines of the AAPM or are attributed to experimental setup deviations, especially since a significant part of the uncertainty in the mean of the values found in this work consisted of experimental setup uncertainties. Therefore, it suffices to include them in a regular QA programme, where the frequency at which the values are validated — for example daily, monthly, or yearly — depends on the QA guidelines by Spruijt et al.. Note that a limitation of this work was the fixed gantry angle of 90 degrees. While no changes are expected, the impact of the gantry angle should ultimately be checked when working towards full clinical implementation [106]. Lastly, a separate but similar characterisation should be performed for the second 'Luit' gantry at HollandPTC when this gantry is commissioned for use in proton FLASH radiotherapy, after which the same QA program can be followed.

The second category encompasses characteristics that require more research, including a thorough investigation over time. This group includes the spot position, output, scanning speed and dose rate (constancy). In this work, spot position data were gathered from measurements conducted on a single day. Given that accurate dose delivery relies heavily on the lateral accuracy of the gantry, the spot position should also be thoroughly investigated over time. The focus should be on aligning the FlashQ with the isocentre. In the measurements performed, a manual correction was applied to account for what was deemed a misalignment with the isocentre. However, no cross-check was conducted if the magnitude of the misalignment corresponded to for instance the position of the individual strips in the FlashQ, as these may be positioned within the device and not directly at the surface of the device.

Regarding the scanning speed, it is important to verify its stability over time. This consideration may seem contrary to findings by Tsai et al., who reported minimal variance in scanning speed on their ProBeam system, noting that even a 10% discrepancy in scanning speed results in only a 1% effect on the resultant dose rate for typical clinical plans [71, 149]. However, further research is warranted, particularly for spot spacings within the clinical range (< 20 mm). In these scenarios, scanning speed can decrease by almost 50%, which is significantly lower than the convergence value. Such substantial reductions can lead to significant differences in dose rates. Combined with the observation that the standard deviation for these data points (see Figure 3.17) is significantly larger for smaller spot spacings, this underscores the need for studies in the clinically relevant domain.

Lastly, there is the issue of the constancy of the output, and consequently, the dose rate. Although this is already measured extensively in this work - both on the same day and across multiple measurement days - the potential consequences of dose rate fluctuations are significant enough that further research is warranted. The fluctuations are primarily caused by the inability of the NMC to regulate dose delivery due to saturation effects. Future research should focus on developing or acquiring an NMC that does not saturate under the nozzle currents and dose rates required for FLASH irradiations. This would enable direct verification of dose delivery during irradiation, allowing for adjustments to the spot dwell time, thereby significantly enhancing the accuracy of dose delivery. If upgrading or replacing the NMC is not feasible, a daily QA program should be established to determine the average variation on any given day, prior to patient irradiation. An example of a proton QA field that can be irradiated is provided by Tsai et al. [149]. This approach would enable proper scaling of the monitor units to ensure that the correct amount of dose, as originally planned, is delivered. Additionally, it is advisable to incorporate extra margins, such as planning for higher dose rates, to ensure that fluctuations in dose rates due to gantry variations do not result in clinically significant deviations. For instance, it is crucial to ensure that dose rates do not fall below 40 Gy/s, regardless of gantry fluctuations, to maintain the effectiveness and potential benefits of proton FLASH RT.

5

Conclusion

As part of the commissioning process of the gantry-based proton FLASH beam line at HollandPTC, the aim of this thesis was to characterise the 250 MeV ultra-high dose rate (UHDR) continuous scanning proton transmission beam. The characterisation was successfully achieved by exploring four key categories on the 'Citer' ProBeam gantry: lateral and longitudinal relative dosimetry, absolute dosimetry, and temporal dosimetry.

The investigation has confirmed that the spot shape remains clinically stable across the entire range of requestable nozzle currents. This enabled the full spatiotemporal reconstruction of individual irradiations, which were measured using the FlashQ strip ionisation chamber. The resulting data demonstrated robust lateral beam accuracy with a spot position accuracy within 0.15 mm, fully compliant with AAPM TG-224 standards. Additionally, with a discrepancy of 0.2 mm, the IDD measurements aligned well with those from another ProBeam facility, although the detected beam energy was slightly lower than nominal, at 248.5 MeV. The FlashQ's time resolution of 1 ms allowed for the quantification of both the spot dwell time and scanning speed. The scanning speed was found to correlate with spot spacing and converged to values of 7.8 ± 0.1 m/s in the horizontal direction and 29.4 ± 0.9 m/s in the vertical direction at the isocentre. These values, although higher than the vendor's specifications, did align with findings from another ProBeam institute. However, although higher scanning speeds could theoretically lead to shorter irradiation times and higher local dose rates, these effects may be deemed not clinically relevant. Ultimately, the characterisation parameters can serve as input parameters for a treatment planning system and also facilitate the calibration of readings from the FlashQ, enabling its use as a reference monitor chamber. This allows for the retrospective retrieval and simulation of the full spatiotemporal and delivered dose (rate) of individual FLASH irradiations.

Significant challenges were identified due to the saturation of the nozzle monitor chamber (NMC) at high nominal nozzle currents. This saturation introduced a current dependency on the dose delivery per monitor unit (MU), complicating the consistency of dose administration. This issue was further compounded by significant day-to-day variations in the nozzle current, ranging from -13.9% to -23.2%, and beam-to-beam variations with an average deviation of 3.9%, collected across six measurement sessions. This was mitigated by scaling the MU and using the FlashQ as a reference monitor chamber, thus allowing for further in-depth UHDR research.

To address the challenges highlighted in this study and enhance the reliability of the proton FLASH beam line at HollandPTC, several recommendations are proposed. First, a deeper insight into day-to-day variations is essential. Implementing daily quality assurance (QA) measurements to assess nozzle current - and thus dose rate - variations could help account for these variations, leading to more consistent and accurate dose delivery. Ultimately, a non-saturating NMC should be considered to resolve issues related to nozzle current variations effectively. Additionally, a robust QA program should be established to monitor parameters like scanning speed and spot position accuracy over time. This will ensure that any deviations from expected parameters are identified and corrected for when they exceed predefined tolerance limits, thereby maintaining the integrity of treatment delivery. Lastly, this research is limited to the use of UHDR transmission proton beams to achieve sufficiently high proton beam intensities. Further investigation into the implementation of pencil beam scanning FLASH beams is necessary to realise Bragg peak conforming proton FLASH radiotherapy, which fully utilises the intrinsic benefit of conventional proton therapy, specifically high dose conformity while sparing healthy tissue.

Bibliography

[1] Eurostat. *Causes of death statistics by age group*. 2023. Retrieved from https://ec.europa.eu/eurostat/statistics-explained/index.php?title=Causes_of_death_statistics_by_age_group.

[2] European Cancer Information System. *Long term estimates of cancer incidence and mortality, for all countries*. 2023. Retrieved from https://ecis.jrc.ec.europa.eu/explorer.php?$0-4$1-All$4-1,2$3-0$6-0,85$5-2022,2040$7-7$21-0$CLongtermChart1_1$X0_-1-AE27$CLongtermChart1_2$X1_-1-AE27$CLongtermChart1_3$X2_-1-AE27$CLongtermChart1_4$X3_14-$X3_-1-AE27$CLongtermTable1_6$X4_-1-AE27.

[3] European Commission. *A cancer plan for Europe*. 2022. Retrieved from https://commission.europa.eu/strategy-and-policy/priorities-2019-2024/promoting-our-european-way-life/european-health-union/cancer-plan-europe_en.

[4] National Cancer Institute. *Types of Cancer Treatment*. 2017. Retrieved from https://www.cancer.gov/about-cancer/treatment/types.

[5] May Abdel-Wahab et al. "Global Radiotherapy: Current Status and Future Directions—White Paper". In: *JCO Global Oncology* (2021). DOI: 10.1200/GO.21.00029.

[6] Josep M. Borras et al. "The optimal utilization proportion of external beam radiotherapy in European countries: An ESTRO-HERO analysis". In: *Radiotherapy and Oncology: Journal of the European Society for Therapeutic Radiology and Oncology* 116(1) (2015), pp. 38–44. DOI: 10.1016/j.radonc.2015.04.018.

[7] Geoff Delaney et al. "The role of radiotherapy in cancer treatment". In: *Cancer* 104(6) (2005), pp. 1129–1137. DOI: 10.1002/cncr.21324.

[8] Elham Hosseinzadeh, Nooshin Banaee, and Hassan Nedaie. "Cancer and Treatment Modalities". In: *Current Cancer Therapy Reviews* 13 (2017). DOI: 10.2174/1573394713666170531081818.

[9] Ruoxi Wang et al. "Targeting the DNA Damage Response for Cancer Therapy". In: *International Journal of Molecular Sciences* 24(21) (2023), p. 15907. DOI: 10.3390/ijms242115907.

[10] RaySearch Laboratories. *RayStation Brochure*. 2022. Retrieved from https://www.raysearchlabs.com/media/publications/raystation-brochure-pdf-read/.

[11] Indra J. Das and Kenneth R. Kase. "Higher energy: Is it necessary, is it worth the cost for radiation oncology?" In: *Medical Physics* 19(4) (1992), pp. 917–925. DOI: 10.1118/1.596779.

[12] Claus Grupen. "Tumour Therapy with Particle Beams". In: *AIP Conference Proceedings*. Vol. 538. Merida, Yucatan (Mexico): AIP Publishing, 2000. DOI: 10.1063/1.1328938.

[13] Timur Mitin and Anthony L. Zietman. "Promise and Pitfalls of Heavy-Particle Therapy". In: *Journal of Clinical Oncology* 32(26) (2014), pp. 2855–2863. DOI: 10.1200/JCO.2014.55.1945.

[14] Carl F. Von Essen. "Radiation Tolerance of the Skin". In: *Acta Radiologica: Therapy, Physics, Biology* 8(4) (1969), pp. 311–330. DOI: 10.3109/02841866909134462.

[15] Michael Goitein. *Radiation oncology: a physicist's-eye view*. 1st ed. Biological and Medical Physics, Biomedical Engineering. New York, NY: Springer New York, 2008. ISBN: 978-0-387-72644-1.

[16] Thomas Bortfeld. "An analytical approximation of the Bragg curve for therapeutic proton beams". In: *Medical Physics* 24(12) (1997), pp. 2024–2033. DOI: 10.1118/1.598116.

[17] Harald Paganetti. *Proton Therapy Physics*. 2nd ed. Boston. USA: CRC Press, 2012. ISBN: 978-1-4398-3645-3. Retrieved from https://www.amazon.nl/-/en/Harald-Paganetti-ebook/dp/B07KRMFP8K.

[18] Hwa Kyung Byun et al. "Physical and Biological Characteristics of Particle Therapy for Oncologists". In: *Cancer Research and Treatment* 53(3) (2021), pp. 611–620. DOI: 10.4143/crt.2021.066.

[19] Ulrike Mock et al. "Comparative treatment planning on localized prostate carcinoma conformal photon- versus proton-based radiotherapy". In: *Strahlentherapie Und Onkologie: Organ Der Deutschen Rontgengesellschaft ... [et Al]* 181(7) (2005), pp. 448–455. DOI: 10.1007/s00066-005-1317-7.

[20] Åsa Palm and Karl-Axel Johansson. “A review of the impact of photon and proton external beam radiotherapy treatment modalities on the dose distribution in field and out-of-field; implications for the long-term morbidity of cancer survivors”. In: *Acta Oncologica* 46(4) (2007), pp. 462–473. DOI: 10.1080/02841860701218626.

[21] Hui Liu and Joe Y. Chang. “Proton therapy in clinical practice”. In: *Chinese Journal of Cancer* 30(5) (2011), pp. 315–326. DOI: 10.5732/cjc.010.10529.

[22] Angélica Pérez-Andújar, Wayne D. Newhauser, and Paul M. Deluca. “Neutron production from beam-modifying devices in a modern double scattering proton therapy beam delivery system”. In: *Physics in Medicine and Biology* 54(4) (2009), pp. 993–1008. DOI: 10.1088/0031-9155/54/4/012.

[23] Christian Bäumer et al. “Clinical Implementation of Proton Therapy Using Pencil-Beam Scanning Delivery Combined With Static Apertures”. In: *Frontiers in Oncology* 11 (2021), p. 599018. DOI: 10.3389/fonc.2021.599018.

[24] Stefano Agosteo et al. “Secondary neutron and photon dose in proton therapy”. In: *Radiotherapy and Oncology* 48(3) (1998), pp. 293–305. DOI: 10.1016/S0167-8140(98)00049-8.

[25] Bernard Gottschalk. *Passive Beam Spreading in Proton Radiation Therapy (DRAFT)*. Oxford, 2004.

[26] Michael Baumann et al. “Radiation oncology in the era of precision medicine”. In: *Nature Reviews Cancer* 16(4) (2016), pp. 234–249. DOI: 10.1038/nrc.2016.18.

[27] Zhe Chen et al. “Proton versus photon radiation therapy: A clinical review”. In: *Frontiers in Oncology* 13 (2023), p. 1133909. DOI: 10.3389/fonc.2023.1133909.

[28] Michael Chuong et al. “Pencil beam scanning versus passively scattered proton therapy for unresectable pancreatic cancer”. In: *Journal of Gastrointestinal Oncology* 9(4) (2018), pp. 687–693. DOI: 10.21037/jgo.2018.03.14.

[29] Zhenwei Zou et al. “Scanning Beam Proton Therapy versus Photon IMRT for Stage III Lung Cancer: Comparison of Dosimetry, Toxicity, and Outcomes”. In: *Advances in Radiation Oncology* 5(3) (2020), pp. 434–443. DOI: 10.1016/j.adro.2020.03.001.

[30] Shravan Kandula et al. “Spot-scanning beam proton therapy *vs* intensity-modulated radiation therapy for ipsilateral head and neck malignancies: A treatment planning comparison”. In: *Medical Dosimetry* 38(4) (2013), pp. 390–394. DOI: 10.1016/j.meddos.2013.05.001.

[31] Yuki Tominaga et al. “Dose-volume comparisons of proton therapy for pencil beam scanning with and without multi-leaf collimator and passive scattering in patients with lung cancer”. In: *Medical Dosimetry* 49(1) (2024), pp. 13–18. DOI: 10.1016/j.meddos.2023.10.006.

[32] Masaru Takagi et al. “Dosimetric Comparison Study of Proton Therapy Using Line Scanning versus Passive Scattering and Volumetric Modulated Arc Therapy for Localized Prostate Cancer”. In: *Cancers* 16(2) (2024), p. 403. DOI: 10.3390/cancers16020403.

[33] Joe Y. Chang et al. “Consensus Guidelines for Implementing Pencil-Beam Scanning Proton Therapy for Thoracic Malignancies on Behalf of the PTCOG Thoracic and Lymphoma Subcommittee”. In: *International Journal of Radiation Oncology*Biology*Physics* 99(1) (2017), pp. 41–50. DOI: 10.1016/j.ijrobp.2017.05.014.

[34] Samuel Swisher-McClure et al. “Comparison of Pencil Beam Scanning Proton- and Photon-Based Techniques for Carcinoma of the Parotid”. In: *International Journal of Particle Therapy* 2(4) (2016), pp. 525–532. DOI: 10.14338/IJPT-15-00005.1.

[35] Mohamed El-Asery et al. “Evaluation of Secondary Neutron Produced in Proton Therapy Using Phits”. In: *Moscow University Physics Bulletin* 78(2) (2023), pp. 155–160. DOI: 10.3103/S0027134923020054.

[36] Uwe Schneider et al. “Secondary neutron dose during proton therapy using spot scanning”. In: *International Journal of Radiation Oncology, Biology, Physics* 53(1) (2002), pp. 244–251. DOI: 10.1016/s0360-3016(01)02826-7.

[37] Luis A. Soto et al. “FLASH Irradiation Results in Reduced Severe Skin Toxicity Compared to Conventional-Dose-Rate Irradiation”. In: *Radiation Research* 194(6) (2020), pp. 618–624. DOI: 10.1667/RADE-20-00090.

[38] Dirk De Ruysscher et al. “Radiotherapy toxicity”. In: *Nature Reviews Disease Primers* 5(1) (2019), pp. 1–20. DOI: 10.1038/s41572-019-0064-5.

[39] Jean Bourhis et al. “Clinical translation of FLASH radiotherapy: Why and how?” In: *Radiotherapy and Oncology*. FLASH radiotherapy International Workshop 139 (2019), pp. 11–17. DOI: 10.1016/j.radonc.2019.04.008.

[40] Vincent Favaudon et al. “Ultrahigh dose-rate FLASH irradiation increases the differential response between normal and tumor tissue in mice”. In: *Science Translational Medicine* 6(245) (2014), 245ra93. DOI: 10.1126/scitranslmed.3008973.

[41] Marie-Catherine Vozenin et al. “The Advantage of FLASH Radiotherapy Confirmed in Mini-pig and Cat-cancer Patients”. In: *Clinical Cancer Research: An Official Journal of the American Association for Cancer Research* 25(1) (2019), pp. 35–42. DOI: 10.1158/1078-0432.CCR-17-3375.

[42] Pierre Montay-Gruel et al. “Irradiation in a flash: Unique sparing of memory in mice after whole brain irradiation with dose rates above 100 Gy/s”. In: *Radiotherapy and Oncology*. 15th International Wolfsberg Meeting 2017 124(3) (2017), pp. 365–369. DOI: 10.1016/j.radonc.2017.05.003.

[43] Jean Bourhis et al. “Treatment of a first patient with FLASH-radiotherapy”. In: *Radiotherapy and Oncology*. FLASH radiotherapy International Workshop 139 (2019), pp. 18–22. DOI: 10.1016/j.radonc.2019.06.019.

[44] Jake Atkinson et al. “The current status of FLASH particle therapy: a systematic review”. In: *Physical and Engineering Sciences in Medicine* 46(2) (2023), pp. 529–560. DOI: 10.1007/s13246-023-01266-z.

[45] Andrea Borghini et al. “FLASH ultra-high dose rates in radiotherapy: preclinical and radiobiological evidence”. In: *International Journal of Radiation Biology* 98(2) (2022), pp. 127–135. DOI: 10.1080/09553002.2022.2009143.

[46] Ronald Chow et al. “FLASH Radiation Therapy: Review of the Literature and Considerations for Future Research and Proton Therapy FLASH Trials”. In: *Applied Radiation Oncology* (2021), pp. 16–21. DOI: 10.37549/ARO1274.

[47] Anna A. Friedl et al. “Radiobiology of the FLASH effect”. In: *Medical Physics* 49(3) (2022), pp. 1993–2013. DOI: 10.1002/mp.15184.

[48] J. S. Kirby-Smith and G. W. Dolphin. “Chromosome Breakage at High Radiation Dose-Rates”. In: *Nature* 182(4630) (1958), pp. 270–271. DOI: 10.1038/182270a0.

[49] D. L. Dewey and J. W. Boag. “Modification of the oxygen effect when bacteria are given large pulses of radiation”. In: *Nature* 183(4673) (1959), pp. 1450–1451. DOI: 10.1038/1831450a0.

[50] C. Tillman et al. “Survival of mammalian cells exposed to ultrahigh dose rates from a laser-produced plasma x-ray source”. In: *Radiology* 213(3) (1999), pp. 860–865. DOI: 10.1148/radiology.213.3.r99dc13860.

[51] P. Wilson et al. “Revisiting the ultra-high dose rate effect: implications for charged particle radiotherapy using protons and light ions”. In: *The British Journal of Radiology* 85(1018) (2012), e933–939. DOI: 10.1259/bjr/17827549.

[52] Joseph D. Wilson et al. “Ultra-High Dose Rate (FLASH) Radiotherapy: Silver Bullet or Fool’s Gold?” In: *Frontiers in Oncology* 9 (2019), p. 1563. DOI: 10.3389/fonc.2019.01563.

[53] Jonathan R. Hughes and Jason L. Parsons. “FLASH Radiotherapy: Current Knowledge and Future Insights Using Proton-Beam Therapy”. In: *International Journal of Molecular Sciences* 21(18) (2020), p. 6492. DOI: 10.3390/ijms21186492.

[54] Henry Rodriguez et al. “Mapping of Peroxyl Radical Induced Damage on Genomic DNA”. In: *Biochemistry* 38(50) (1999), pp. 16578–16588. DOI: 10.1021/bi9918994.

[55] T. Dunn. “Oxygen and cancer”. In: *North Carolina Medical Journal* 58(2) (1997), pp. 140–143.

[56] Ramin Abolfath, David Grosshans, and Radhe Mohan. “Oxygen depletion in FLASH ultra-high-dose-rate radiotherapy: A molecular dynamics simulation”. In: *Medical Physics* 47(12) (2020), pp. 6551–6561. DOI: 10.1002/mp.14548.

[57] Guillem Pratx and Daniel S. Kapp. “A computational model of radiolytic oxygen depletion during FLASH irradiation and its effect on the oxygen enhancement ratio”. In: *Physics in Medicine & Biology* 64(18) (2019), p. 185005. DOI: 10.1088/1361-6560/ab3769.

[58] Gabriel Adrian et al. “The FLASH effect depends on oxygen concentration”. In: *The British Journal of Radiology* 93(1106) (2020), p. 20190702. DOI: 10.1259/bjr.20190702.

[59] Yuta Shiraishi, Yusuke Matsuya, and Hisanori Fukunaga. “Possible mechanisms and simulation modeling of FLASH radiotherapy”. In: *Radiological Physics and Technology* 17(1) (2024), pp. 11–23. DOI: 10.1007/s12194-023-00770-x.

[60] Gabriel Adrian et al. “Cancer Cells Can Exhibit a Sparing FLASH Effect at Low Doses Under Normoxic In Vitro-Conditions”. In: *Frontiers in Oncology* 11 (2021), p. 686142. DOI: 10.3389/fonc.2021.686142.

[61] R. J. Berry and D Phil. “EFFECTS OF RADIATION DOSE-RATE: From Protracted, Continuous Irradiation to Ultra-High Dose-Rates from Pulsed Accelerators”. In: *British Medical Bulletin* 29(1) (1973), pp. 44–47. DOI: 10.1093/oxfordjournals.bmb.a070955.

[62] Shirley Hornsey and Tikvah Alper. “Unexpected Dose-rate Effect in the Killing of Mice by Radiation”. In: *Nature* 210(5032) (1966), pp. 212–213. DOI: 10.1038/210212a0.

[63] Jörg Pawelke et al. “Electron dose rate and oxygen depletion protect zebrafish embryos from radiation damage”. In: *Radiotherapy and Oncology* 158 (2021), pp. 7–12. DOI: 10.1016/j.radonc.2021.02.003.

[64] Eric S. Diffenderfer et al. “Design, Implementation, and in Vivo Validation of a Novel Proton FLASH Radiation Therapy System”. In: *International Journal of Radiation Oncology, Biology, Physics* 106(2) (2020), pp. 440–448. DOI: 10.1016/j.ijrobp.2019.10.049.

[65] Qixian Zhang et al. “FLASH Investigations Using Protons: Design of Delivery System, Preclinical Setup and Confirmation of FLASH Effect with Protons in Animal Systems”. In: *Radiation Research* 194(6) (2020), pp. 656–664. DOI: 10.1667/RADE-20-00068.1.

[66] N. Rama et al. “Improved Tumor Control Through T-cell Infiltration Modulated by Ultra-High Dose Rate Proton FLASH Using a Clinical Pencil Beam Scanning Proton System”. In: *International Journal of Radiation Oncology, Biology, Physics* 105(1) (2019), S164–S165. DOI: 10.1016/j.ijrobp.2019.06.187.

[67] Elke Beyreuther et al. “Feasibility of proton FLASH effect tested by zebrafish embryo irradiation”. In: *Radiotherapy and Oncology*. FLASH radiotherapy International Workshop 139 (2019), pp. 46–50. DOI: 10.1016/j.radonc.2019.06.024.

[68] Anthony E. Mascia et al. “Proton FLASH Radiotherapy for the Treatment of Symptomatic Bone Metastases: The FAST-01 Nonrandomized Trial”. In: *JAMA oncology* 9(1) (2023), pp. 62–69. DOI: 10.1001/jamaoncol.2022.5843.

[69] Varian, a Siemens Healthineers Company. *Feasibility Study of FLASH Radiotherapy for the Treatment of Symptomatic Bone Metastases*. Clinical trial registration NCT04592887. clinicaltrials.gov, 2023. Retrieved from https://clinicaltrials.gov/study/NCT04592887.

[70] Varian, a Siemens Healthineers Company. *FLASH Radiotherapy for the Treatment of Symptomatic Bone Metastases in the Thorax*. Clinical trial registration NCT05524064. clinicaltrials.gov, 2024. Retrieved from https://clinicaltrials.gov/study/NCT05524064.

[71] Sheng Huang et al. “Implementation of novel measurement-based patient-specific QA for pencil beam scanning proton FLASH radiotherapy”. In: *Medical Physics* 50(7) (2023), pp. 4533–4545. DOI: 10.1002/mp.16458.

[72] Wei Zou et al. “Current delivery limitations of proton PBS for FLASH”. In: *Radiotherapy and Oncology* 155 (2021), pp. 212–218. DOI: 10.1016/j.radonc.2020.11.002.

[73] Nolan Esplen, Marc S. Mendonca, and Magdalena Bazalova-Carter. “Physics and biology of ultrahigh dose-rate (FLASH) radiotherapy: a topical review”. In: *Physics in Medicine & Biology* 65(23) (2020), 23TR03. DOI: 10.1088/1361-6560/abaa28.

[74] Alexander Koschik et al. “Gantry 3: Further Development of the PSI PROSCAN Proton Therapy Facility”. In: JACOW, Geneva, Switzerland, 2015, pp. 2275–2277. ISBN: 978-3-95450-168-7. DOI: 10.18429/JACoW-IPAC2015-TUPWI016. Retrieved from https://accelconf.web.cern.ch/IPAC2015/doi/JACoW-IPAC2015-TUPWI016.html.

[75] Jiajian Shen et al. “Technical Note: Using experimentally determined proton spot scanning timing parameters to accurately model beam delivery time”. In: *Medical Physics* 44(10) (2017), pp. 5081–5088. DOI: 10.1002/mp.12504.

[76] Frank Verhaegen et al. “Considerations for shoot-through FLASH proton therapy”. In: *Physics in Medicine & Biology* 66(6) (2021), 06NT01. DOI: 10.1088/1361-6560/abe55a.

[77] Lorraine Courneyea et al. “Optimizing mini-ridge filter thickness to reduce proton treatment times in a spot-scanning synchrotron system”. In: *Medical Physics* 41(6Part1) (2014), p. 061713. DOI: 10.1118/1.4876276.

[78] T. Furukawa et al. “Development of NIRS pencil beam scanning system for carbon ion radiotherapy”. In: *Nuclear Instruments and Methods in Physics Research Section B: Beam Interactions with Materials and Atoms*. Proceedings of the 12th European Conference on Accelerators in Applied Research and Technology (ECAART12) 406 (2017), pp. 361–367. DOI: 10.1016/j.nimb.2016.10.029.

[79] Tami Freeman. *Patient-specific ridge filters enable conformal FLASH proton therapy*. 2023. Retrieved from https://physicsworld.com/a/patient-specific-ridge-filters-enable-conformal-flash-proton-therapy/.

[80] Guoliang Zhang, Wenchao Gao, and Hao Peng. “Design of static and dynamic ridge filters for FLASH–IMPT: A simulation study”. In: *Medical Physics* 49(8) (2022), pp. 5387–5399. DOI: 10.1002/mp.15717.

[81] Yuri Simeonov et al. “3D range-modulator for scanned particle therapy: development, Monte Carlo simulations and experimental evaluation”. In: *Physics in Medicine & Biology* 62(17) (2017), p. 7075. DOI: 10.1088/1361-6560/aa81f4.

[82] Bethany Rothwell et al. “Treatment planning considerations for the development of FLASH proton therapy”. In: *Radiotherapy and Oncology* 175 (2022), pp. 222–230. DOI: 10.1016/j.radonc.2022.08.003.

[83] Steven van de Water et al. “Towards FLASH proton therapy: the impact of treatment planning and machine characteristics on achievable dose rates”. In: *Acta Oncologica (Stockholm, Sweden)* 58(10) (2019), pp. 1463–1469. DOI: 10.1080/0284186X.2019.1627416.

[84] Patricia van Marlen et al. “Ultra-High Dose Rate Transmission Beam Proton Therapy for Conventionally Fractionated Head and Neck Cancer: Treatment Planning and Dose Rate Distributions”. In: *Cancers* 13(8) (2021), p. 1859. DOI: 10.3390/cancers13081859.

[85] Hao Gao et al. “Simultaneous dose and dose rate optimization (SDDRO) for FLASH proton therapy”. In: *Medical Physics* 47(12) (2020), pp. 6388–6395. DOI: 10.1002/mp.14531.

[86] Minglei Kang et al. “Quantitative Assessment of 3D Dose Rate for Proton Pencil Beam Scanning FLASH Radiotherapy and Its Application for Lung Hypofractionation Treatment Planning”. In: *Cancers* 13(14) (2021), p. 3549. DOI: 10.3390/cancers13143549.

[87] Shouyi Wei et al. “Use of single-energy proton pencil beam scanning Bragg peak for intensity-modulated proton therapy FLASH treatment planning in liver-hypofractionated radiation therapy”. In: *Medical Physics* 49(10) (2022), pp. 6560–6574. DOI: 10.1002/mp.15894.

[88] Michael M. Folkerts et al. “A framework for defining FLASH dose rate for pencil beam scanning”. In: *Medical Physics* 47(12) (2020), pp. 6396–6404. DOI: 10.1002/mp.14456.

[89] Rodrigo José Santo et al. “Pencil-beam Delivery Pattern Optimization Increases Dose Rate for Stereotactic FLASH Proton Therapy”. In: *International Journal of Radiation Oncology*Biology*Physics* 115(3) (2023), pp. 759–767. DOI: 10.1016/j.ijrobp.2022.08.053.

[90] Bijan Arjomandy et al. “AAPM task group 224: Comprehensive proton therapy machine quality assurance”. In: *Medical Physics* 46(8) (2019). DOI: 10.1002/mp.13622.

[91] Kees Spruijt et al. “Multi-institutional consensus on machine QA for isochronous cyclotron-based systems delivering ultra-high dose rate (FLASH) pencil beam scanning proton therapy in transmission mode”. In: *Medical Physics* 51(2) (2024), pp. 786–798. DOI: 10.1002/mp.16854.

[92] Gabriele Kragl et al. “Dosimetric characteristics of 6 and 10MV unflattened photon beams”. In: *Radiotherapy and Oncology* 93(1) (2009), pp. 141–146. DOI: 10.1016/j.radonc.2009.06.008.

[93] Md. Motiur Rahman et al. “Dosimetric characterization of medical linear accelerator Photon and Electron beams for the treatment accuracy of cancer patients”. In: *Tsinghua Science & Technology* 3 (2021), pp. 41–059.

[94] Serenella Russo et al. “Dosimetric Characterization of Small Radiotherapy Electron Beams Collimated by Circular Applicators with the New Microsilicon Detector”. In: *Applied Sciences* 12(2) (2022), p. 600. DOI: 10.3390/app12020600.

[95] J. D. Steben, K. Ayyangar, and N. Suntharalingam. “Betatron electron beam characterisation for dosimetry calculations”. In: *Physics in Medicine & Biology* 24(2) (1979), p. 299. DOI: 10.1088/0031-9155/24/2/006.

[96] T. Arunkumar et al. “Electron beam characteristics at extended source-to-surface distances for irregular cut-outs”. In: *Journal of Medical Physics / Association of Medical Physicists of India* 35(4) (2010), pp. 207–214. DOI: 10.4103/0971-6203.71763.

[97] M. Rovituso et al. *Characterisation of the HollandPTC R&D proton beamline for physics and radiobiology studies*. 2023. DOI: 10.48550/arXiv.2302.09943. Retrieved from http://arxiv.org/abs/2302.09943.

[98] Emmanuelle Fleury et al. "Characterization of the HollandPTC proton therapy beamline dedicated to uveal melanoma treatment and an interinstitutional comparison". In: *Medical Physics* 48(8) (2021), pp. 4506–4522. DOI: 10.1002/mp.15024.

[99] Linh T. Tran et al. "Characterization of proton pencil beam scanning and passive beam using a high spatial resolution solid-state microdosimeter". In: *Medical Physics* 44(11) (2017), pp. 6085–6095. DOI: 10.1002/mp.12563.

[100] M. Kang and D. Pang. "Commissioning and beam characterization of the first gantry-mounted accelerator pencil beam scanning proton system". In: *Medical Physics* 47(8) (2020), pp. 3496–3510. DOI: 10.1002/mp.13972.

[101] Alexandra Bourgouin et al. "Characterization of the PTB ultra-high pulse dose rate reference electron beam". In: *Physics in Medicine & Biology* 67(8) (2022), p. 085013. DOI: 10.1088/1361-6560/ac5de8.

[102] Lucia Giuliano et al. "Characterization of Ultra-High-Dose Rate Electron Beams with ElectronFlash Linac". In: *Applied Sciences* 13(1) (2023), p. 631. DOI: 10.3390/app13010631.

[103] Riccardo Dal Bello et al. "Enabling ultra-high dose rate electron beams at a clinical linear accelerator for isocentric treatments". In: *Radiotherapy and Oncology* 187 (2023), p. 109822. DOI: 10.1016/j.radonc.2023.109822.

[104] J. D. Aylward et al. "Characterisation of the UK high energy proton research beamline for high and ultra-high dose rate (FLASH) irradiation". In: *Biomedical Physics & Engineering Express* 9(5) (2023), p. 055032. DOI: 10.1088/2057-1976/acef25.

[105] Yunjie Yang et al. "A 2D strip ionization chamber array with high spatiotemporal resolution for proton pencil beam scanning FLASH radiotherapy". In: *Medical Physics* 49(8) (2022), pp. 5464–5475. DOI: 10.1002/mp.15706.

[106] Serdar Charyyev et al. "Characterization of 250 MeV Protons from the Varian ProBeam PBS System for FLASH Radiation Therapy". In: *International Journal of Particle Therapy* 9(4) (2023), pp. 279–289. DOI: 10.14338/IJPT-22-00027.1.

[107] HollandPTC. *Research: benefit and efficacy of proton therapy*. 2024. Retrieved from https://www.hollandptc.nl/research/.

[108] Yunjie Yang et al. "Commissioning a 250 MeV research beamline for proton FLASH radiotherapy preclinical experiments". In: *Medical Physics* 50(7) (2023), pp. 4623–4636. DOI: 10.1002/mp.16364.

[109] Brita Singers Sørensen et al. "In vivo validation and tissue sparing factor for acute damage of pencil beam scanning proton FLASH". In: *Radiotherapy and Oncology* 167 (2022), pp. 109–115. DOI: 10.1016/j.radonc.2021.12.022.

[110] DE.TEC.TOR. *FlashQ: Technical Specifications*. Retrieved from https://detector-group.com/flashq/.

[111] IBA. *Lynx PT: High accuracy and speed for daily machine parameter verification*. Retrieved from https://www.iba-dosimetry.com/product/lynx-pt.

[112] Ashland. *GAFchromic™ EBT3 film specifications*. Retrieved from http://www.gafchromic.com/gafchromic-film/radiotherapy-films/EBT/index.asp.

[113] Pyramid. *BC-75: Faraday Cup Beam Collector for Particle Therapy QA and Diagnostics*. Retrieved from https://ptcusa.com/products/bc-75.

[114] Ethan W. Cascio and Bernard Gottschalk. "A Simplified Vacuumless Faraday Cup for the Experimental Beamline at the Francis H. Burr Proton Therapy Center". In: *2009 IEEE Radiation Effects Data Workshop*. 2009, pp. 161–165. DOI: 10.1109/REDW.2009.5336294. Retrieved from https://ieeexplore.ieee.org/document/5336294?denied=.

[115] PTW. *Advanced Markus®Chamber Type 34045*. Retrieved from https://www.ptwdosimetry.com/fileadmin/user_upload/Online_Catalog/DETECTORS_Cat_en_16522900-14/blaetterkatalog/blaetterkatalog/pdf/save/bk_35.pdf.

[116] PTW. *Bragg Peak® Chamber Type 34070*. Retrieved from https://www.ptwdosimetry.com/en/products/bragg-peak-ionization-chambers.

[117] PTW. *X-Ray Therapy Monitor Chamber 7862*. Retrieved from https://www.ptwdosimetry.com/en/products/x-ray-therapy-monitor-chamber-7862.

[118] R. J. Barlow. *Statistics: A Guide and Reference to the Use of Statistical Methods in the Physical Sciences*. Manchester Physics Series. Wiley, 1993. ISBN: 0-471-92295-1.

[119] Michael P. Fay and Michael A. Proschan. "Wilcoxon-Mann-Whitney or t-test? On assumptions for hypothesis tests and multiple interpretations of decision rules". In: *Statistics surveys* 4 (2010), pp. 1–39. DOI: 10.1214/09-SS051.

[120] Stanislaw Szpala et al. "Dosimetry with a clinical linac adapted to FLASH electron beams". In: *Journal of Applied Clinical Medical Physics* 22(6) (2021), pp. 50–59. DOI: 10.1002/acm2.13270.

[121] Elise Konradsson et al. "Correction for Ion Recombination in a Built-in Monitor Chamber of a Clinical Linear Accelerator at Ultra-High Dose Rates". In: *Radiation Research* 194(6) (2020), pp. 580–586. DOI: 10.1667/RADE-19-00012.

[122] Michael Lempart et al. "Modifying a clinical linear accelerator for delivery of ultra-high dose rate irradiation". In: *Radiotherapy and Oncology*. FLASH radiotherapy International Workshop 139 (2019), pp. 40–45. DOI: 10.1016/j.radonc.2019.01.031.

[123] Emil Schüler et al. "Experimental Platform for Ultra-high Dose Rate FLASH Irradiation of Small Animals Using a Clinical Linear Accelerator". In: *International Journal of Radiation Oncology*Biology*Physics* 97(1) (2017), pp. 195–203. DOI: 10.1016/j.ijrobp.2016.09.018.

[124] Maud Jaccard et al. "High dose-per-pulse electron beam dosimetry: Usability and dose-rate independence of EBT3 Gafchromic films". In: *Medical Physics* 44(2) (2017), pp. 725–735. DOI: 10.1002/mp.12066.

[125] Kristoffer Petersson et al. "High dose-per-pulse electron beam dosimetry — A model to correct for the ion recombination in the Advanced Markus ionization chamber". In: *Medical Physics* 44(3) (2017), pp. 1157–1167. DOI: 10.1002/mp.12111.

[126] Elke Beyreuther et al. "Research Facility for Radiobiological Studies at the University Proton Therapy Dresden". In: *International Journal of Particle Therapy* 5(1) (2018), pp. 172–182. DOI: 10.14338/IJPT-18-00008.1.

[127] Annalisa Patriarca et al. "Experimental Set-up for FLASH Proton Irradiation of Small Animals Using a Clinical System". In: *International Journal of Radiation Oncology, Biology, Physics* 102(3) (2018), pp. 619–626. DOI: 10.1016/j.ijrobp.2018.06.403.

[128] L. Karsch et al. "Dose rate dependence for different dosimeters and detectors: TLD, OSL, EBT films, and diamond detectors". In: *Medical Physics* 39(5) (2012), pp. 2447–2455. DOI: 10.1118/1.3700400.

[129] Daphnée Villoing et al. "Technical note: Proton beam dosimetry at ultra-high dose rates (FLASH): Evaluation of GAFchromic™ (EBT3, EBT-XD) and OrthoChromic (OC-1) film performances". In: *Medical Physics* 49(4) (2022), pp. 2732–2745. DOI: 10.1002/mp.15526.

[130] International Atomic Energy Agency. *Absorbed Dose Determination in External Beam Radiotherapy*. Rev. 1. Technical Reports Series. International Atomic Energy Agency, 2024. ISBN: 978-92-0-146022-6. DOI: 10.61092/iaea.ve7q-y94k. Retrieved from https://www.iaea.org/publications/15048.

[131] IBA. *IBA Dosimetry: Blue Phantom 2*. Retrieved from https://www.iba-dosimetry.com/product/blue-phantom-2.

[132] PTW. *RW3 Slab Phantom*. Retrieved from https://www.ptwdosimetry.com/en/products/rw3-slab-phantom/.

[133] Arash Darafsheh et al. "Spread-out Bragg peak proton FLASH irradiation using a clinical synchrocyclotron: Proof of concept and ion chamber characterization". In: *Medical Physics* 48(8) (2021), pp. 4472–4484. DOI: 10.1002/mp.15021.

[134] Eunsin Lee et al. "Ultrahigh dose rate pencil beam scanning proton dosimetry using ion chambers and a calorimeter in support of first in-human FLASH clinical trial". In: *Medical Physics* 49(9) (2022), pp. 6171–6182. DOI: 10.1002/mp.15844.

[135] Brita Singers Sørensen et al. "Pencil beam scanning proton FLASH maintains tumor control while normal tissue damage is reduced in a mouse model". In: *Radiotherapy and Oncology* 175 (2022), pp. 178–184. DOI: 10.1016/j.radonc.2022.05.014.

[136] A. Mirandola et al. “Determination of ion recombination and polarity effects for the PTW Advanced Markus ionization chamber in synchrotron based scanned proton and carbon ion beams”. In: *Physica Medica* 96 (2022), pp. 149–156. DOI: 10.1016/j.ejmp.2022.03.007.

[137] PTW. *UNIDOS E Universal Dosemeter*. Retrieved from https://www.google.com/search?client=firefox-b-d&q=unidos+e+specs#ip=1.

[138] Ana Lourenço et al. “Absolute dosimetry for FLASH proton pencil beam scanning radiotherapy”. In: *Scientific Reports* 13(1) (2023), p. 2054. DOI: 10.1038/s41598-023-28192-0.

[139] Wei Zou et al. “Characterization of a high-resolution 2D transmission ion chamber for independent validation of proton pencil beam scanning of conventional and FLASH dose delivery”. In: *Medical Physics* 48(7) (2021), pp. 3948–3957. DOI: 10.1002/mp.14882.

[140] M. A. Chanrion et al. “Dosimetric consequences of pencil beam width variations in scanned beam particle therapy”. In: *Physics in Medicine & Biology* 58(12) (2013), p. 3979. DOI: 10.1088/0031-9155/58/12/3979.

[141] Yuting Lin et al. “Impacts of gantry angle dependent scanning beam properties on proton PBS treatment”. In: *Physics in Medicine & Biology* 62(2) (2016), p. 344. DOI: 10.1088/1361-6560/aa5084.

[142] L. De Marzi et al. “Experimental characterisation of a proton kernel model for pencil beam scanning techniques”. In: *Physica Medica* 64 (2019), pp. 195–203. DOI: 10.1016/j.ejmp.2019.07.013.

[143] Yupeng Li et al. “Beyond Gaussians: a study of single-spot modeling for scanning proton dose calculation”. In: *Physics in Medicine & Biology* 57(4) (2012), p. 983. DOI: 10.1088/0031-9155/57/4/983.

[144] E. Seravalli et al. “2D dosimetry in a proton beam with a scintillating GEM detector”. In: *Physics in Medicine & Biology* 54(12) (2009), p. 3755. DOI: 10.1088/0031-9155/54/12/010.

[145] Mahbubur Rahman et al. “Characterization of a new scintillation imaging system for proton pencil beam dose rate measurements”. In: *Physics in Medicine & Biology* 65(16) (2020), p. 165014. DOI: 10.1088/1361-6560/ab9452.

[146] S. Russo et al. “Characterization of a commercial scintillation detector for 2-D dosimetry in scanned proton and carbon ion beams”. In: *Physica Medica* 34 (2017), pp. 48–54. DOI: 10.1016/j.ejmp.2017.01.011.

[147] Ulrich W. Langner et al. “Comparison of multi-institutional Varian ProBeam pencil beam scanning proton beam commissioning data”. In: *Journal of Applied Clinical Medical Physics* 18(3) (2017), pp. 96–107. DOI: 10.1002/acm2.12078.

[148] Danny Giancarlo Apaza Veliz et al. “Monte Carlo Calculation of the Energy Spectrum of a 6 MeV Electron Beam using PENetration and Energy Loss of Positrons and Electrons Code”. In: *Journal of Medical Physics* 45(2) (2020), p. 116. DOI: 10.4103/jmp.JMP_104_19.

[149] Pingfang Tsai et al. “A comprehensive pre-clinical treatment quality assurance program using unique spot patterns for proton pencil beam scanning FLASH radiotherapy”. In: *Journal of Applied Clinical Medical Physics* (2024). DOI: 10.1002/acm2.14400.

[150] Eleni Kanouta et al. “Time structure of pencil beam scanning proton FLASH beams measured with scintillator detectors and compared with log files”. In: *Medical Physics* 49(3) (2022), pp. 1932–1943. DOI: 10.1002/mp.15486.

[151] Per Rugaard Poulsen et al. “Efficient Interplay Effect Mitigation for Proton Pencil Beam Scanning by Spot-Adapted Layered Repainting Evenly Spread out Over the Full Breathing Cycle”. In: *International Journal of Radiation Oncology, Biology, Physics* 100(1) (2018), pp. 226–234. DOI: 10.1016/j.ijrobp.2017.09.043.

[152] Alfred Smith et al. “The M. D. Anderson proton therapy system”. In: *Medical Physics* 36(9Part1) (2009), pp. 4068–4083. DOI: 10.1118/1.3187229.

[153] Milton Abramowitz and Irene A. Stegun. *Handbook of Mathematical Functions: With Formulas, Graphs, and Mathematical Tables*. Courier Corporation, 1965. ISBN: 978-0-486-61272-0.

A

Appendix

A.1 Spot shape

Table A.1: Overview of the test statistics for the unpaired t-test and Mann-Whitney U test. For each spot shape parameter σ_x, σ_y and θ, both tests are used to compare the corresponding parameter distributions for the 10 and 215 nA nozzle currents. The statistic value can only be used to verify the performed analysis, the p-value is used to either accept or reject the null hypothesis.

	σ_x		σ_y		θ	
Test type	Statistic	p-value	Statistic	p-value	Statistic	p-value
Unpaired t-test	3.29	0.00	-2.70	0.02	0.70	0.49
Mann-Whitney U	21	0.03	17	0.01	65	0.28

A.2 Beam envelope

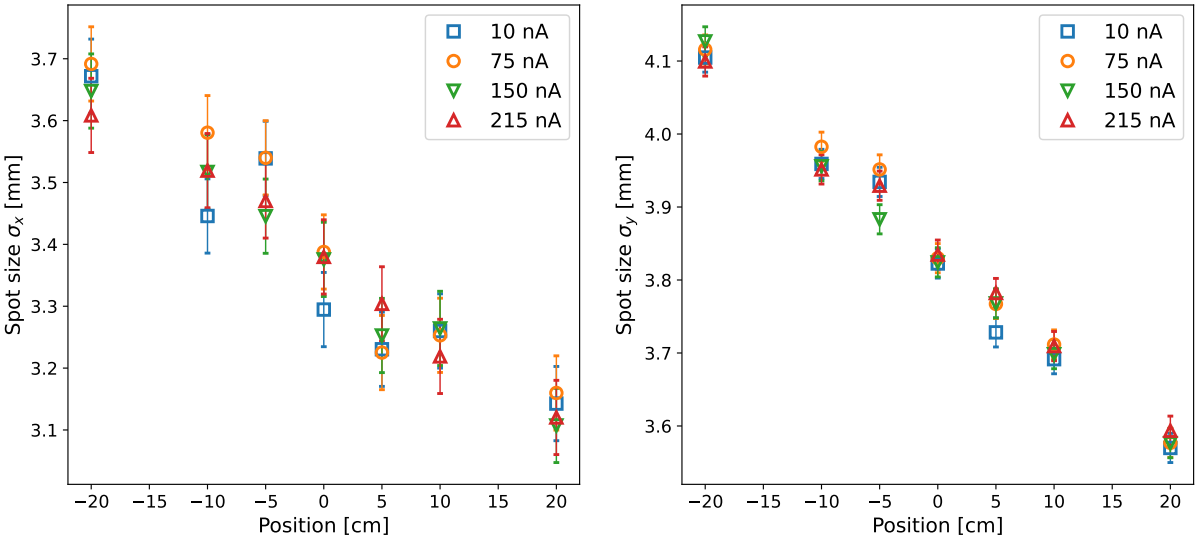

Figure A.1: Beam envelope of the 250 MeV proton beam. The spot sizes σ_x and σ_y for each nozzle current are plotted against the relative position with respect to the gantry's isocentre (ISOC = 0 cm). Positions towards the gantry are represented by positive x-axis values, while positions away from it are indicated by negative values. The error bars represent the maximum standard deviation for σ_x and σ_y from Table 3.1. The current-averaged data points can be found in Figure 3.6.

A.3 IDD

Table A.2: Overview of all contributions to the total water equivalent thickness (WET) for the R_{80} calculation. The Bragg peak chamber is abbreviated as BPC.

Contribution	WET [mm]
Bragg peak chamber	4
Monitor chamber	0.36
Blue Phantom 2 entrance window	6.35
Water between BPC and entrance window	1
Total	11.71

A.3.1 Bortfeld function

The Bortfeld function is an analytical approximation for therapeutic Bragg curves, published in 1997 by Thomas Bortfeld [16]. The theoretical model is based on the parameters presented in Table A.3.

Table A.3: Overview of the used constants and parameters for the Bortfeld function. The given values are solely valid for protons in water. E_0 is the initial energy of the proton. The last two parameters ($\sigma_{E,0}$ and ϵ), are machine specific values. Table is adapted from [16].

Symbol	Description	Value	Unit
p	Exponent of range-energy relation (see R_0)	1.77	-
α	Proportionality factor (see R_0)	0.0022	cm MeV^{-p}
R_0	Proton range	αE_0^p	cm
β	Slope parameter of fluence reduction	0.012	cm^{-1}
γ	Fraction of locally absorbed energy released in nonelastic nuclear interactions	0.6	-
σ_{mono}	Width of Gaussian range straggling	$0.012R_0^{0.935}$	cm
$\sigma_{E,0}$	Width of Gaussian energy spectrum	$\approx 0.01E_0$	MeV
ϵ	Fraction of primary fluence contributing to the "tail" of the energy spectrum	$\approx$ 0.0-0.2	-

These parameters are used in the theoretical expression for the depth-dose distribution $D(z)$, given by:

$$D(z) = \Phi_0 \frac{e^{-\zeta^2/4}\sigma^{1/p}\Gamma(1/p)}{\sqrt{2\pi\rho p}\alpha^{1/p}(1+\beta R_0)}\left[\frac{1}{\sigma}\mathscr{D}^{-1/p}(-\zeta) + \left(\frac{\beta}{p}+\gamma\beta+\frac{\epsilon}{R_0}\right)\mathscr{D}^{-1/p-1}(-\zeta)\right] \tag{A.3.1}$$

with $\mathscr{D}$ the parabolic cylinder function [153], Γ the gamma function, ρ the mass density of the medium, z the depth in the medium and ζ defined as $(R_0 - z)/\sigma$. However, due to the formula's length and divergence for $\zeta > 20$, Eq. A.3.1 is numerically impractical to fit. Therefore, various assumptions and simplifications are made to rewrite the Bortfeld function to a computationally simpler form. As a result, the dose-depth distribution in water $D_{H_2O}(z)$ is given by:

$$D_{H_2O}(z) = \Phi_0 \frac{e^{-(R_0-z)^2/4\sigma^2}\sigma^{0.565}}{1+0.012R_0} \times \left[11.26\sigma^{-1}\mathscr{D}^{-0.565}\left(\frac{R_0-z}{\sigma}\right) + (0.157+11.26\epsilon/R_0)\mathscr{D}^{-1.565}\left(\frac{R_0-z}{\sigma}\right)\right] \tag{A.3.2}$$

This equation can be computationally fitted as it only depends on four parameters: R_0, σ, ϵ and p. For the determination of the energy spectrum, the Gaussian energy spectrum parameter σ is of interest. From theory, this parameter is proportional to both σ_{mono} and $\sigma_{E,0}$ through:

$$\sigma^2 = \sigma_{\text{mono}}^2 + \sigma_{E,0}^2\left(\frac{dR_0}{dE_0}\right)^2 = (0.012R_0^{0.935})^2 + \sigma_{E,0}^2\alpha^2p^2E_0^{2p-2} \tag{A.3.3}$$

The only unknown in this equation is $\sigma_{E,0}$ as all other parameters (including σ) are either given or fitted. Hence, the value of the width of the Gaussian energy spectrum (in MeV) can be determined. The accuracy of the fit can be verified by comparing the fitted values of R_0 and p to known values as R_0 is a function of the proton beam energy and $p \approx 1.77$.

A.4 Saturation effects BPC and MC

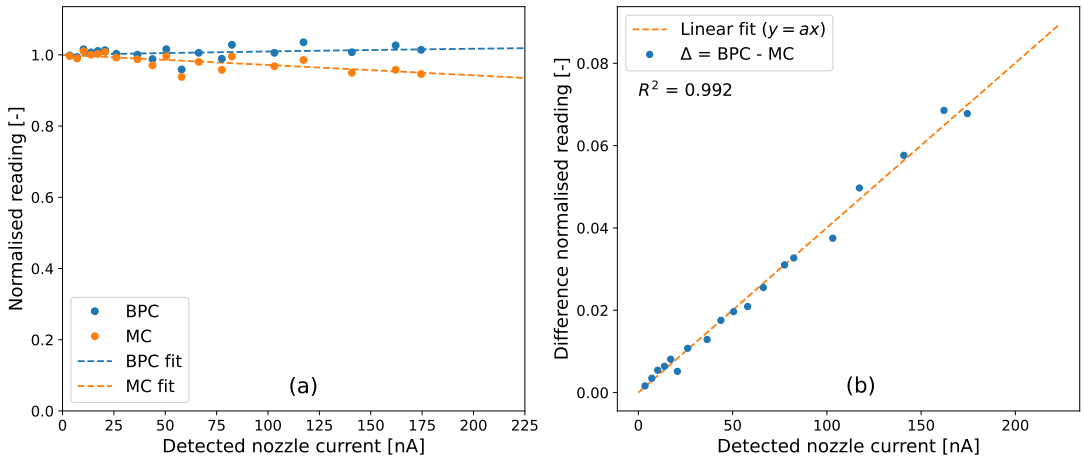

Figure A.2: (a) Saturation curve for the Bragg peak chamber (BPC) and the 7862 monitor chamber (MC) against the detected nozzle current. A separate second-degree polynomial fit is performed for both detectors. (b) The difference Δ between the normalised reading from the BPC and MC overlaid with a linear fit.

A.5 Output

Table A.4: Overview of all contributions to the total water equivalent thickness (WET) for the output measurements. The Advanced Markus is abbreviated as AM.

Contribution	WET [mm]
FlashQ	0.76
Water phantom entrance window	3.36
Distance between AM-holder and AM window	1.1
AM window	1.04
Total	6.26

A.6 Spot dwell time

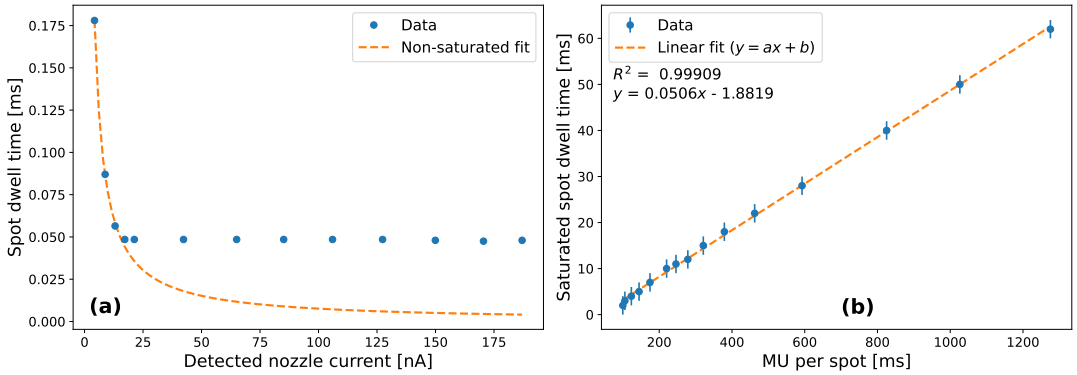

Figure A.3: (a) The spot dwell time per MU as a function of the detected nozzle current, measured by the FlashQ detector. The dashed curve represents the inverse-proportional relationship between spot dwell time and nozzle beam current in the absence of saturation. (b) The saturated spot dwell times plotted as a function of the the MU per spot. A linear fit is performed to investigate the linearity.

A.7 Dose rate

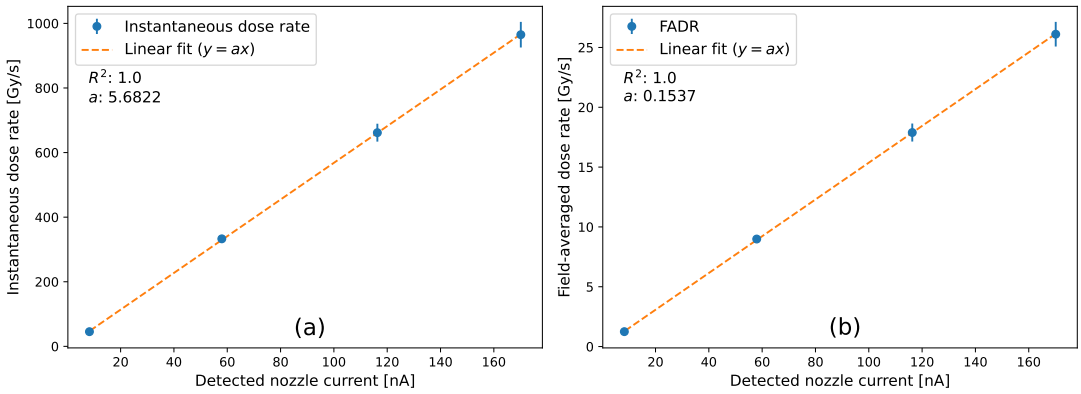

Figure A.4: The (a) instantaneous dose rate and (b) field-averaged dose rate as a function of the detected current, with a linear fit included. The plotted data points represent the average dose rates calculated from four different dose levels for each specific nominal nozzle current, with error bars indicating the uncertainty in the mean.

A.8 Coupling FlashQ and Faraday cup

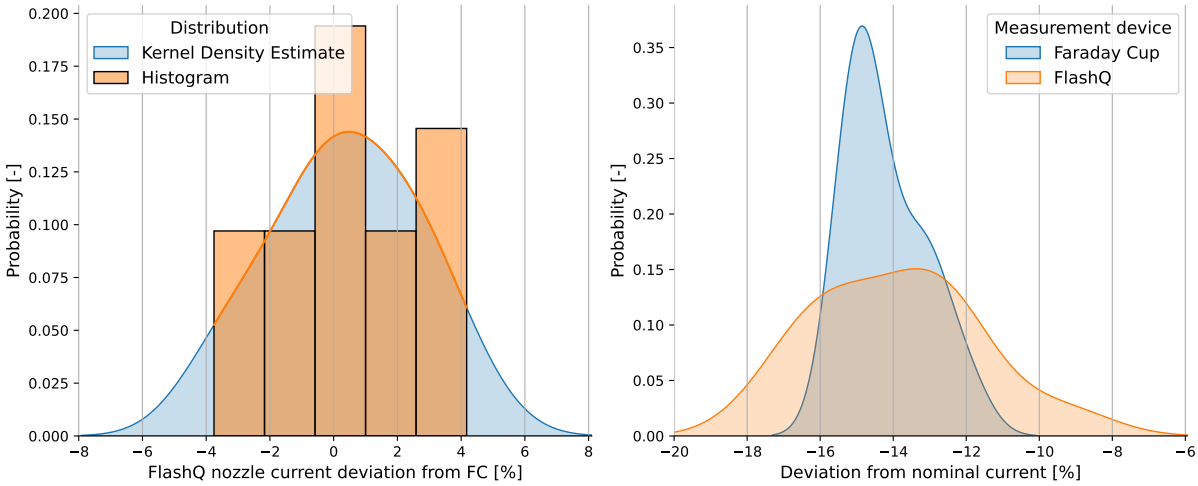

Figure A.5: (a) Histogram of the relative difference in detected nozzle current between the FlashQ and Faraday cup. (b) Probability density estimations of the detected nominal nozzle current deviation detected by the FlashQ and Faraday cup. The deviation is calculated through Eq. 2.7.

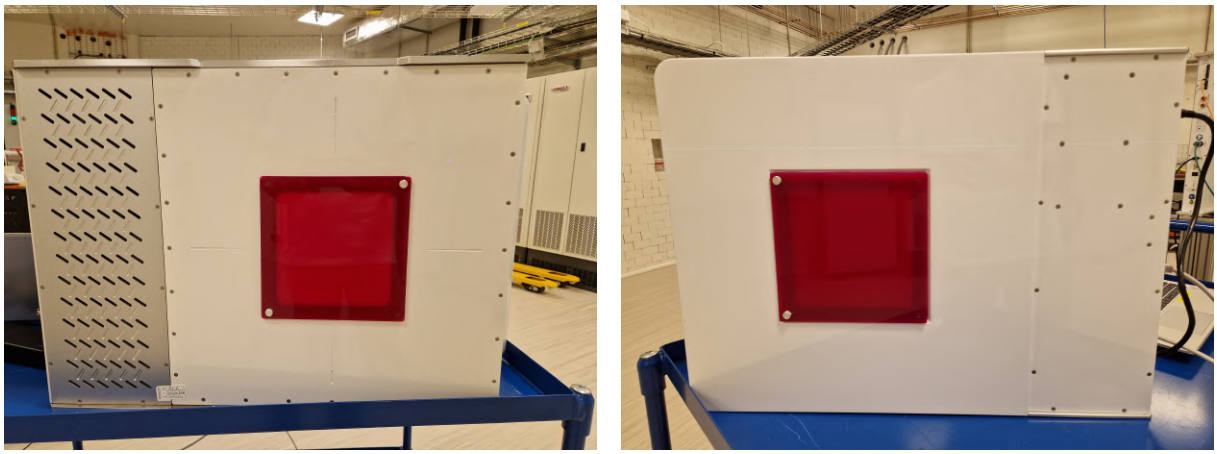

Figure A.6: Photos of the original FlashQ (left) and the loan FlashQ (right) for comparison. The original FlashQ is characterised by its sharp edges and includes two metal side panels, with a metal grating at the front. In contrast, the loan FlashQ features a fully white casing with more rounded edges.